ΕΛΛΗΝΙΚΗ ΔΗΜΟΚΡΑΤΙΑ
ΠΑΝΕΠΙΣΤΗΜΙΟ ΙΩΑΝΝΙΝΩΝ
ΠΟΛΥΤΕΧΝΙΚΗ ΣΧΟΛΗ
ΤΜΗΜΑ ΜΗΧΑΝΙΚΩΝ ΕΠΙΣΤΗΜΗΣ ΥΛΙΚΩΝ
ΠΡΟΓΡΑΜΜΑ ΜΕΤΑΠΤΥΧΙΑΚΩΝ ΣΠΟΥΔΩΝ
«ΤΕΧΝΟΛΟΓΙΕΣ ΠΡΟΗΓΜΕΝΩΝ ΥΛΙΚΩΝ»

ΜΕΤΑΠΤΥΧΙΑΚΗ ΔΙΠΛΩΜΑΤΙΚΗ ΕΡΓΑΣΙΑ

Αγνή Πυθαρά

STUDY OF GRAPHENE SATURABLE ABSORPTION FOR NEAR-INFRARED OPTICAL PULSE RESHAPING

ΙΩΑΝΝΙΝΑ, 2026

Η παρούσα Μεταπτυχιακή Διπλωματική Εργασία εκπονήθηκε στο πλαίσιο των σπουδών για την απόκτηση του Διπλώματος Μεταπτυχιακών Σπουδών που απονέμει το Τμήμα Μηχανικών Επιστήμης Υλικών του Πανεπιστημίου Ιωαννίνων.

Εγκρίθηκε την ……28/07/2026……..από την εξεταστική επιτροπή:

1. Ελευθέριος Λοιδωρίκης, Καθηγητής του Τμήματος Μηχανικών Επιστήμης Υλικών της Πολυτεχνικής Σχολής του Πανεπιστημίου Ιωαννίνων, **Επιβλέπων**

2. **Δημήτριος Παπαγεωργίου**, Καθηγητής του Τμήματος Μηχανικών Επιστήμης Υλικών της Πολυτεχνικής Σχολής του Πανεπιστημίου Ιωαννίνων

3. **Νικόλαος Καλφαγιάννης**, Επίκουρος Καθηγητής του Τμήματος Μηχανικών Επιστήμης Υλικών της Πολυτεχνικής Σχολής του Πανεπιστημίου Ιωαννίνων

ΥΠΕΥΘΥΝΗ ΔΗΛΩΣΗ

"Δηλώνω υπεύθυνα ότι η παρούσα διατριβή εκπονήθηκε κάτω από τους διεθνείς ηθικούς και ακαδημαϊκούς κανόνες δεοντολογίας και προστασίας της πνευματικής ιδιοκτησίας. Σύμφωνα με τους κανόνες αυτούς, δεν έχω προβεί σε ιδιοποίηση ξένου επιστημονικού έργου και έχω πλήρως αναφέρει τις πηγές που χρησιμοποίησα στην εργασία αυτή."

(Υπογραφή υποψηφίου)

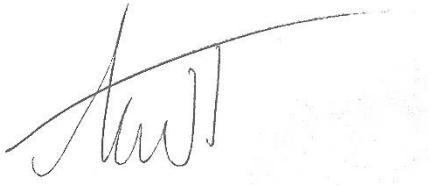

Contents

Acknowledgments

I would like to express my sincere gratitude to my supervisor, Professor Elefterios Lidorikis, for his guidance, scientific insight, and continuous support throughout the development of this thesis. He was consistently supportive, patient, and available whenever difficulties arose. His attention to detail and insistence on physical consistency and rigorous analysis were essential to the completion of this work and contributed significantly to my personal and academic development.

I am particularly grateful to Dr. Spyridon-Chrysovalantis Doukas for his valuable scientific guidance, technical support, and the numerous discussions concerning the physics of graphene. His knowledge, experience, and support in the physical interpretation of the results were invaluable throughout this work.

Special acknowledgment is due to Professor Andrea C. Ferrari and the Cambridge Graphene Centre, University of Cambridge, for providing the experimental measurements used in this work. Access to these data made it possible to compare the developed numerical model with experimentally measured graphene transmission and to investigate the physical parameters governing its nonlinear response.

I would also like to thank Associate Professor Konstantinos S. Daskalakis and his research group at the University of Turku, Finland, for the fabrication and provision of the six-period dielectric Bragg reflector employed in the experimental structure and considered in the cavity-design part of this thesis. Their contribution provided the experimental basis for the realistic modeling and optimization of the graphene-loaded photonic cavity.

I am grateful to all members of the research group at the Department of Materials Science and Engineering of the University of Ioannina for the constructive scientific environment, and the discussions that contributed directly or indirectly to this work.

Finally, I would like to thank my family and the people close to me for their patience, encouragement, and unwavering support throughout my studies. Their presence was especially important during the most demanding stages of this effort.

Abstract

Graphene saturable absorption is of particular interest for nonlinear photonic applications because of graphene's broadband optical response and ultrafast photoexcited-carrier dynamics. However, saturation intensities reported in the literature differ by several orders of magnitude, while the weak absorption of an isolated graphene sheet limits the modulation achievable in a single optical pass. In this context, the purpose of this thesis is to investigate graphene saturable absorption and apply it to the design of a reflective near-infrared pulse-shaping device.

To this end, a time-dependent model is employed to describe the evolution of the non-equilibrium carrier population and the electronic and lattice temperatures during pulsed excitation. Subsequently, the resulting time-dependent optical response of graphene is coupled to the transfer matrix method, thereby relating the transient carrier dynamics to the reflection, transmission, and absorption of complete multilayer photonic structures.

As a first step in evaluating the model, published saturation intensities are compared. The analysis showed that the large spread among reported values persists even after normalization using analytical relations derived from the model. Moreover, no clear dependence was identified on the measurement method, substrate or host material, fabrication route, or Raman ratio I_D/I_G. In addition, comparison with measurements from an electrostatically gated single-layer graphene (SLG) device showed that a common set of model parameters provides a reasonable approximation of the main Fermi-level-dependent trends in the nonlinear transmission.

Building on this evaluation, the model was then applied to the design of an asymmetric Fabry–Pérot cavity consisting of a Bragg reflector, a dielectric spacer, graphene, and a metallic mirror. The strongest pulse-shaping response was obtained for a cavity with a PMMA spacer, illumination from the Bragg-reflector side, and three graphene layers. Under these conditions, at a wavelength of 1579.13 nm, an initially single-peaked Gaussian pulse was transformed into reflected profiles containing two or three distinct peaks, depending on the incident peak intensity. This response results from the dynamic variation of the cavity losses near the critical-coupling condition. Overall, the results demonstrate that, under resonant conditions, the device can convert the relatively weak absorption of graphene into strong temporal modulation of the reflected field. Finally, the proposed devices are currently being fabricated with the aim of experimentally validating their predicted operation as passive, all-optical pulse shapers.

Περίληψη

Η κορέσιμη απορρόφηση του γραφενίου παρουσιάζει ιδιαίτερο ενδιαφέρον για εφαρμογές μη γραμμικής φωτονικής, χάρη στην ευρυζωνική οπτική του απόκριση και στην υπερταχεία δυναμική των φωτοδιεγερμένων φορέων. Ωστόσο, οι εντάσεις κορεσμού που αναφέρονται στη βιβλιογραφία διαφέρουν κατά πολλές τάξεις μεγέθους, ενώ η περιορισμένη απορρόφηση ενός απομονωμένου φύλλου γραφενίου περιορίζει τη διαμόρφωση που μπορεί να επιτευχθεί σε μία μόνο διέλευση του φωτός. Σκοπός της παρούσας διπλωματικής εργασίας είναι η μελέτη της κορέσιμης απορρόφησης του γραφενίου, καθώς και η αξιοποίησή της για τον σχεδιασμό μιας διάταξης διαμόρφωσης παλμών στο εγγύς υπέρυθρο.

Για τον σκοπό αυτό χρησιμοποιείται ένα χρονικά εξαρτώμενο μοντέλο, το οποίο περιγράφει την εξέλιξη του πληθυσμού των φορέων εκτός ισορροπίας, καθώς και των θερμοκρασιών του ηλεκτρονικού συστήματος και του πλέγματος κατά την παλμική διέγερση. Παράλληλα, η προκύπτουσα οπτική απόκριση του γραφενίου υπολογίζεται με τη μέθοδο πινάκων μεταφοράς, επιτρέποντας τη σύνδεση της παροδικής κατάστασης των φορέων με την ανάκλαση, τη διέλευση και την απορρόφηση πολυστρωματικών φωτονικών διατάξεων.

Στη συνέχεια, το μοντέλο αξιοποιείται για τη σύγκριση τιμών έντασης κορεσμού, δημοσιευμένων στη βιβλιογραφία. Η ανάλυση έδειξε ότι η μεγάλη διασπορά των τιμών παραμένει ακόμη και μετά την κανονικοποίησή τους με τη χρήση αναλυτικών σχέσεων που προκύπτουν από το μοντέλο. Επιπλέον, δεν διαπιστώθηκε σαφής εξάρτηση από τη μέθοδο μέτρησης, το υπόστρωμα ή το υλικό υποδοχής, τη μέθοδο παρασκευής ή τον λόγο Raman I_D/I_G. Έπειτα, η σύγκριση με μετρήσεις από ηλεκτροστατικά ρυθμιζόμενη διάταξη μονοστρωματικού γραφενίου έδειξε ότι ένα κοινό σύνολο παραμέτρων του μοντέλου μπορεί να προσεγγίσει τις εξαρτώμενες από το επίπεδο Fermi καμπύλες της μη γραμμικής διέλευσης.

Τέλος, το μοντέλο εφαρμόστηκε στον σχεδιασμό μιας ασύμμετρης κοιλότητας Fabry–Pérot, η οποία αποτελείται από ανακλαστήρα Bragg, διηλεκτρικό διαχωριστικό στρώμα, γραφένιο και μεταλλικό κάτοπτρο. Η ισχυρότερη διαμόρφωση παλμών επιτεύχθηκε για κοιλότητα με διαχωριστικό στρώμα PMMA, πρόσπτωση από την πλευρά του ανακλαστήρα Bragg και τρεις στρώσεις γραφενίου. Σε μήκος κύματος 1579.13 nm, ένας αρχικά μονοκορυφικός Γκαουσιανός παλμός μετασχηματίστηκε σε ανακλώμενα προφίλ με δύο ή τρεις διακριτές κορυφές, ανάλογα με τη μέγιστη προσπίπτουσα ένταση. Η απόκριση αυτή οφείλεται στη δυναμική μεταβολή των απωλειών της κοιλότητας κοντά στη συνθήκη κρίσιμης σύζευξης. Τα αποτελέσματα καταδεικνύουν ότι, υπό συνθήκες συντονισμού, η διάταξη μπορεί να μετατρέψει τη σχετικά ασθενή απορρόφηση του γραφενίου σε ισχυρή χρονική διαμόρφωση του ανακλώμενου πεδίου. Οι προτεινόμενες διατάξεις βρίσκονται ήδη σε διαδικασία κατασκευής, με στόχο την πειραματική επιβεβαίωση της προβλεπόμενης λειτουργίας τους ως παθητικών, εξ ολοκλήρου οπτικών διαμορφωτών παλμών.

Chapter 1

Introduction

1.1 Motivation

The temporal control of optical pulses is important in applications including optical communications, ultrafast spectroscopy, optical metrology, and laser material processing [1–3]. In particular, these applications require optical signals whose amplitude, duration, and temporal profile can be controlled over increasingly short time scales [1, 2]. Consequently, the development of methods capable of performing this control directly in the optical domain constitutes an important objective in nonlinear photonics [2, 4].

The suitability of a pulse-shaping method depends strongly on the duration and bandwidth of the incident pulse [1, 2]. Spectral Fourier techniques provide extensive control over broadband femtosecond pulses, but become increasingly demanding for picosecond pulses, whose narrower bandwidth contains fewer spectral components that can be controlled independently [1, 2]. Alternatively, electro-optic modulation enables pulse shaping directly in the time domain, although its temporal resolution is limited by the bandwidth of both the modulator and the associated electronic driving system [4]. In this context, the direct use of an ultrafast optical nonlinearity offers a complementary route for reshaping picosecond pulses without requiring an electrical waveform with the same temporal structure [5].

Saturable absorption (SA) is particularly well suited to this purpose because it converts the instantaneous intensity of an incident pulse into a time-dependent optical loss [6, 7]. Accordingly, saturable absorbers are widely used for passive mode locking and ultrashort-pulse generation, while they have also been investigated for optical modulation and temporal pulse reshaping [6–9]. Among the most established implementations, conventional semiconductor saturable-absorber mirrors provide reliable operation. However, their spectral range and tunability are constrained by the semiconductor band structure and the design of the multilayer structure [6, 7]. These limitations have therefore motivated the investigation of carbon nanomaterials and two-dimensional materials as alternative saturable absorbers [7, 10, 11].

Graphene is particularly attractive for this role because it combines broadband optical absorption, electrical tunability, and ultrafast carrier dynamics [8, 12, 13]. Owing to this combination of properties, graphene saturable absorbers have been demonstrated in free-space, fibre, and integrated configurations, enabling mode locking over a broad spectral range [8, 9, 14, 15]. Moreover, their nonlinear optical response can be modified through con-

trol of the Fermi level, providing an additional degree of freedom for tuning the operation of graphene-based photonic devices [4, 16].

Despite these advantages, the quantitative description of graphene SA remains challenging. In particular, reported saturation intensities span several orders of magnitude, even among measurements performed in similar spectral regions [8, 9, 16, 17]. This large variation creates a practical difficulty for device design, since an empirical saturation curve fitted to a specific experiment cannot generally be expected to remain valid when the pulse duration, excitation wavelength, or carrier-dynamics conditions are changed [16, 18, 19]. Consequently, a physics-based model is required to relate the intensity-dependent optical response to the relevant optical and carrier-dynamics parameters, while remaining computationally efficient enough to be incorporated into repeated simulations of a complete multilayer device.

Existing theoretical studies have established the non-perturbative character of graphene saturable absorption and examined its dependence on excitation conditions, carrier relaxation, and doping [16, 18–20]. Nevertheless, incorporating the transient graphene response accurately into device-scale simulations requires the optical response and carrier dynamics to be treated within a common numerical framework. This requirement becomes particularly important under pulsed excitation, since the electronic state of graphene, and therefore its optical response, evolves continuously throughout the pulse [13, 19, 21].

Beyond this modelling challenge, a further limitation arises from the small absolute optical absorption of a single graphene layer. Suspended, undoped single-layer graphene absorbs approximately 2.3% of normally incident light in the visible and near-infrared interband regime [12]. Although this absorption is exceptionally large relative to the atomic thickness of graphene, it limits the modulation depth achievable in a single optical pass. Consequently, resonant structures, optical waveguides, and photonic cavities have been employed to enhance the interaction between light and graphene [22, 23].

Among these approaches, Fabry–Pérot and Bragg cavities are especially attractive because their optical response can be engineered through the cavity geometry and the position of the active layer within the resonant field [22, 23]. Moreover, operation close to critical coupling can substantially increase the fraction of the incident power absorbed by an atomically thin active layer [23–26]. Under these conditions, even a relatively small change in graphene absorption can produce a much larger variation in the reflected power [23].

Taken together, these considerations identify two interconnected requirements. The first is a transient model capable of relating graphene SA to the excitation conditions and the relevant carrier-dynamics parameters. The second is the enhancement of the weak single-pass light–graphene interaction, so that the intensity-dependent absorption can produce a substantial device-level optical response. Accordingly, this thesis addresses both requirements by coupling a time-dependent graphene carrier-dynamics model, based on the framework developed in Refs. [22, 27], to a resonant multilayer structure designed for reflective near-infrared pulse shaping.

1.2 Scope

This thesis investigates graphene saturable absorption and its application to a reflective near-infrared pulse-shaping device. More specifically, its central objective is to determine how the transient carrier dynamics of graphene produce intensity-dependent changes in the reflection and absorption of a resonant photonic structure. To address this objective, the work combines time-dependent carrier-dynamics calculations, multilayer optical simulations, comparison with published and experimental measurements, and device optimization.

The first objective is to assess the physical consistency of the graphene saturable-absorption model through comparison with available measurements. To this end, reported saturation intensities obtained using different experimental techniques are collected and normalized with respect to excitation wavelength, saturable absorbance, and the effective number of graphene layers. The remaining dispersion is examined in relation to the measurement method, fabrication route, substrate or host material, pulse conditions, and Raman-derived structural characteristics [28–30]. Furthermore, the calculated linear and nonlinear transmission responses are compared with measurements from an electrostatically gated single-layer graphene device.

Building on this evaluation, the second objective is to apply the model to the design and optimization of a reflective pulse-shaping device. For this purpose, the proposed structure incorporates graphene into an asymmetric Fabry–Pérot cavity consisting of a dielectric Bragg reflector, a dielectric spacer, and a metallic reflector. Such resonant graphene-loaded cavities have previously been shown to enhance the interaction between graphene and the incident optical field [23]. Accordingly, the analysis examines the reflected temporal profiles and identifies the operating conditions under which a single incident pulse is transformed into two or three distinct output peaks. Finally, the optimized configurations are evaluated in terms of their wavelength and incident-intensity tolerances, allowing maximum pulse-shaping performance to be distinguished from operation that is less sensitive to experimental deviations.

1.3 Layout

This thesis is organized as follows:

- **Chapter 2** presents the theoretical background on graphene optical properties, photoexcited-carrier dynamics, optical cavities, and critical coupling.
- **Chapter 3** describes the computational methods used for the optical and time-dependent simulations.
- **Chapter 4** presents the graphene SA model, compares reported saturation intensities, and evaluates the model against experimental transmission measurements.
- **Chapter 5** applies the model to the design and optimization of a graphene-loaded reflective pulse-shaping device.
- **Chapter 6** summarizes the main conclusions.

- **Appendix A** estimates third-harmonic generation and assesses its influence on the optical response of the devices studied.

Chapter 2

Theoretical Background

This chapter establishes the theoretical framework required to describe graphene saturable absorption and its integration into resonant photonic structures. The electronic band structure and carrier statistics of graphene are first introduced, as they determine its linear and nonlinear optical response. The discussion then turns to the generation, thermalization, and cooling of photoexcited carriers, which govern the transient variation of graphene absorption under pulsed excitation. Finally, the operating principles of Bragg mirrors, Fabry–Pérot cavities, and critical coupling are presented, providing the basis for the graphene-loaded reflective pulse-shaping structures investigated in the following chapters.

2.1 Electronic properties of graphene

2.1.1 Lattice and band structure

The carbon atoms in single-layer graphene are arranged in a two-dimensional honeycomb network. Despite its hexagonal symmetry, this honeycomb structure is not a Bravais lattice. It is therefore described as a triangular Bravais lattice with a two-atom basis [31, 32], corresponding to the two sublattices A and B, as shown in figure 2.1.

The real-space primitive lattice vectors can be expressed as

$$\mathbf{a}_1 = \frac{a}{2}(3, \sqrt{3}), \qquad \mathbf{a}_2 = \frac{a}{2}(3, -\sqrt{3}), \tag{2.1}$$

where $a \approx 1.42$ Å is the carbon–carbon bond length [32]. The three nearest-neighbour vectors connecting an atom on one sublattice to the adjacent atoms on the opposite sublattice are

$$\boldsymbol{\delta}_1 = \frac{a}{2}(1, \sqrt{3}), \qquad \boldsymbol{\delta}_2 = \frac{a}{2}(1, -\sqrt{3}), \qquad \boldsymbol{\delta}_3 = -a(1, 0). \tag{2.2}$$

The reciprocal lattice is generated by the primitive vectors

$$\mathbf{b}_1 = \frac{2\pi}{3a}(1, \sqrt{3}), \qquad \mathbf{b}_2 = \frac{2\pi}{3a}(1, -\sqrt{3}). \tag{2.3}$$

These reciprocal lattice vectors define the periodicity of the electronic structure in momentum space and determine the first Brillouin zone [33]. Its corners contain two inequivalent high-symmetry points, denoted by K and K'.

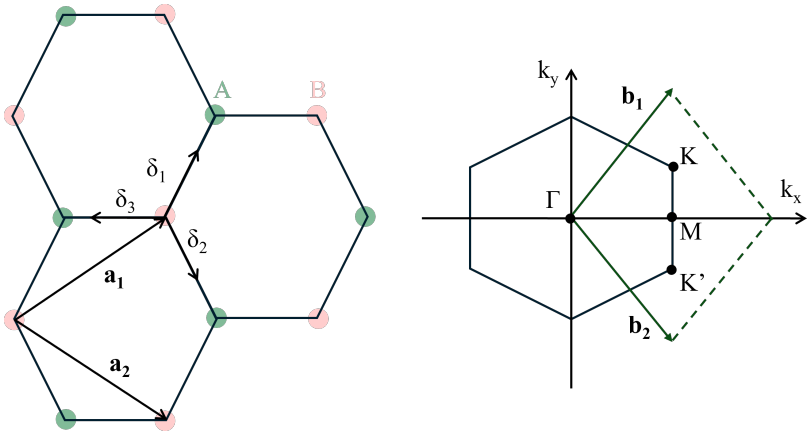

Figure 2.1: Left: real-space lattice of graphene and A and B, the two sublattices. The vectors $\mathbf{a}_1$ and $\mathbf{a}_2$ denote the primitive lattice vectors, while $\boldsymbol{\delta}_i$, $i = 1, 2, 3$, represent the nearest-neighbour vectors. Right: first Brillouin zone of graphene, showing the corners K and K', together with the reciprocal-lattice primitive vectors $\mathbf{b}_1$ and $\mathbf{b}_2$.

The electronic properties of graphene are dominated by the π and π^* bands, which originate from the out-of-plane p_z orbitals of the carbon atoms [32]. The tight-binding approximation can be used to describe these bands by assuming that electrons hop between nearest-neighbour carbon atoms [31,32]. Within this approximation, the energy dispersion is written as [32]

$$E_{\pm}(\mathbf{k}) = \pm t\sqrt{3 + f(\mathbf{k})}, \tag{2.4}$$

where

$$f(\mathbf{k}) = 2\cos\left(\sqrt{3}k_y a\right) + 4\cos\left(\frac{\sqrt{3}}{2}k_y a\right)\cos\left(\frac{3}{2}k_x a\right). \tag{2.5}$$

Here, $t \approx 2.8$ eV is the nearest-neighbour hopping energy, and a is the carbon–carbon bond length [32]. The plus and minus signs in eq. (2.4) correspond to the upper π^* band and the lower π band, respectively.

Figure 2.2 shows the full band structure of graphene calculated from Eq. (2.4). This expression is obtained within the nearest-neighbour tight-binding approximation and therefore neglects further-neighbour hopping terms. When such terms are included, electron–hole symmetry is broken and the band structure is modified away from the K and K' points [32,34].

Expanding eq. (2.4) around the K or K' point by writing the wave vector as $\mathbf{q} = \mathbf{K} + \mathbf{k}$, with $|\mathbf{k}| \ll |\mathbf{K}|$, yields [31]

$$\epsilon(\mathbf{k}) = \pm\frac{3ta}{2}|\mathbf{k}| = \pm\hbar v_{F,\mathrm{SLG}}|\mathbf{k}|, \tag{2.6}$$

where $v_{F,\mathrm{SLG}} = 3ta/(2\hbar) \approx 10^6$ m/s is the Fermi velocity [32]. The K and K' points are commonly referred to as the Dirac points. In their vicinity, the valence and conduction bands display a linear conical dispersion, forming the characteristic Dirac cones [35], as indicated by the circled region in Fig. 2.2. Within this low-energy approximation, the magnitude of the carrier group velocity is approximately constant and independent of the carrier energy, reflecting the massless Dirac-fermion character of charge carriers in graphene [34,35].

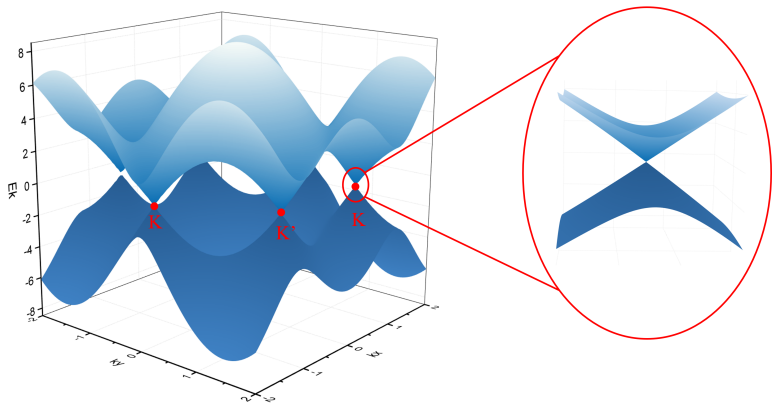

Figure 2.2: Three-dimensional representation of the π and π^* bands of single-layer graphene. Red markers denote representative K and K' points, and the inset magnifies the band structure around one selected K point.

The density of states varies linearly with energy and includes the fourfold spin and valley degeneracy [32]

$$\nu(\epsilon) = \frac{2}{\pi \left(\hbar v_{F,\mathrm{SLG}}\right)^2} |\epsilon|. \tag{2.7}$$

Integrating Eq. (2.7) gives the charge carrier density at zero temperature

$$n(\epsilon) = \int_0^{\epsilon} \nu(\epsilon')\, d\epsilon' = \frac{\epsilon^2}{\pi \left(\hbar v_{F,\mathrm{SLG}}\right)^2}. \tag{2.8}$$

Therefore, the carrier density can be related to the Fermi level through [32]

$$E_{F,\mathrm{SLG}} = \pm \hbar v_{F,\mathrm{SLG}} \sqrt{\pi |n|}. \tag{2.9}$$

The positive sign corresponds to electrons with $n > 0$, while the negative sign corresponds to holes with $n < 0$.

2.1.2 Electrostatic Control of the Fermi Level

Controlling the carrier density in graphene is essential for tuning the position of the Fermi level relative to the Dirac point. In ideal undoped graphene, the Fermi level coincides with the Dirac point, where the net carrier density vanishes and electron and hole populations are balanced. As follows from Eq. (2.9), varying the carrier density shifts the Fermi level above or below the Dirac point, corresponding to electron or hole doping, respectively [35].

The carrier density can be modified through substitutional incorporation of heteroatoms during synthesis or by post-synthesis chemical functionalization. These approaches, however, may introduce disorder, lattice defects, chemical residues, or irreversible structural modifications [36–38]. By contrast, electrostatic gating varies the carrier density by applying an external gate voltage across a dielectric layer [39]. Because it does not require chemical

modification of the graphene lattice, electrostatic gating provides a reversible and comparatively non-destructive means of tuning the Fermi level.

In a typical gated graphene structure, the graphene sheet and a metal or doped-semiconductor gate electrode are separated by a dielectric layer of thickness d and relative permittivity ϵ_r. Within a simple parallel-plate capacitor model, the induced change in carrier density is given by [39]

$$\Delta n = \frac{C_g V_g}{e} = \frac{\epsilon_0 \epsilon_r V_g}{ed}, \tag{2.10}$$

where C_g is the gate capacitance per unit area, V_g is the applied gate voltage, ϵ_0 is the vacuum permittivity, and e is the elementary charge.

Combining Eqs. (2.9), (2.10), the magnitude of the Fermi level can be related to the applied gate voltage as

$$|E_{F,\mathrm{SLG}}(V_g)| = \hbar v_{F,\mathrm{SLG}} \sqrt{\frac{\pi \epsilon_0 \epsilon_r |V_g|}{ed}}. \tag{2.11}$$

This expression assumes the ideal case in which the charge neutrality point occurs at $V_g = 0$. In real devices, unintentional charge transfer from the substrate, residues, trapped charges, or fabrication-induced impurities can lead to a finite carrier density at zero gate voltage. As a result, the charge neutrality point is reached at a non-zero gate voltage, denoted by V_{CNP}. In that case, the gate voltage must be measured relative to the charge neutrality voltage V_{CNP}, and V_g in eq. (2.11) is replaced by $V_g - V_{\mathrm{CNP}}$.

2.1.3 Equilibrium chemical potential

At thermodynamic equilibrium, the occupation probability of electronic states in graphene is described by the Fermi–Dirac distribution

$$f_{\mathrm{FD}}(\varepsilon; \mu, T_e) = \left[\exp\left(\frac{\varepsilon - \mu}{k_B T_e} \right) + 1 \right]^{-1}, \tag{2.12}$$

where T_e is the carrier temperature and μ is the chemical potential [31, 40]. The chemical potential controls the occupation of the electronic bands and therefore determines the electron and hole densities. At $T_e = 0$, the distribution reduces to a step function: states with $\varepsilon < \mu$ are fully occupied, whereas states with $\varepsilon > \mu$ are empty. For $T_e > 0$, Fermi–Dirac broadening occurs around μ, as shown in Fig. 2.3 (a).

The doping level is conveniently specified through the zero-temperature Fermi energy E_F. For electron-doped graphene, $E_F > 0$, the electron and hole densities at $T_e = 0$ are

$$n_e(E_F, 0) = \int_0^{E_F} \nu(\varepsilon)\, d\varepsilon = \frac{E_F^2}{\pi(\hbar v_F)^2}, \qquad n_h(E_F, 0) = 0. \tag{2.13}$$

At finite temperature, both conduction-band electrons and valence-band holes are thermally populated. Their densities are calculated from the graphene density of states, Eq. (2.7),

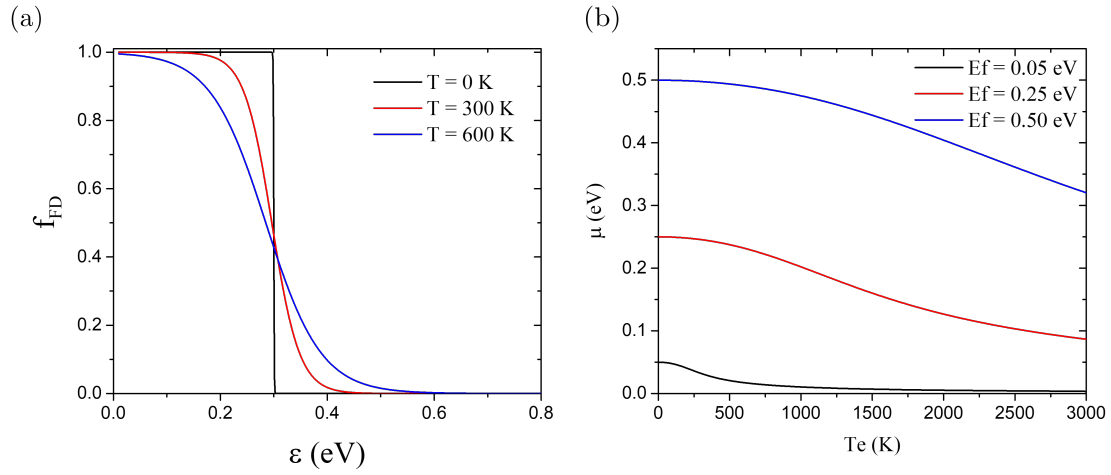

Figure 2.3: (a) Fermi–Dirac distribution as a function of carrier energy for different temperatures and $E_F = 0.3$ eV. At $T = 0$ K, the distribution has a step-like form, while at finite temperatures the occupation around the chemical potential is broadened. (b) Equilibrium chemical potential μ of electron-doped graphene as a function of carrier temperature T_e, calculated from the charge-conservation condition in Eq. (2.16). The curves correspond to different zero-temperature Fermi energies E_F. As T_e increases, μ shifts towards the Dirac point.

weighted by the Fermi–Dirac distribution

$$n_e(\mu, T_e) = \int_0^\infty \nu(\varepsilon) f_{\text{FD}}(\varepsilon; \mu, T_e)\, d\varepsilon, \tag{2.14}$$

$$n_h(\mu, T_e) = \int_0^\infty \nu(\varepsilon) f_{\text{FD}}(\varepsilon; -\mu, T_e)\, d\varepsilon. \tag{2.15}$$

The equilibrium chemical potential at each temperature is obtained by requiring that the net carrier density remains fixed by the doping level. For electron-doped graphene,

$$n_e(\mu, T_e) - n_h(\mu, T_e) = \frac{E_F^2}{\pi(\hbar v_F)^2}. \tag{2.16}$$

Eq. (2.16) is solved numerically for μ at each value of T_e.

The behavior shown in Fig. 2.3 (b) follows directly from charge conservation. As the temperature increases, additional electron and hole states become thermally populated. Since the difference $n_e - n_h$ must remain fixed by the doping level, the chemical potential moves towards the Dirac point. Therefore,

$$\mu(T_e) \to E_F \quad \text{for} \quad T_e \to 0, \qquad |\mu(T_e)| < |E_F| \quad \text{for} \quad T_e > 0. \tag{2.17}$$

2.1.4 Electronic heat capacity

The electronic heat capacity c_e quantifies how much energy is required to increase the temperature of the carrier system [40]. Graphene exhibits an exceptionally low electronic heat

capacity, which leads to large temperature rises even for small absorbed excitation energies [13, 37]. It is defined as the temperature derivative of the carriers' total internal energy, $U(\mu, T_e)$, as [40, 41]

$$\begin{aligned} c_e(\mu, T_e) &= \frac{\partial U(\mu, T_{e,})}{\partial T_e} \\ &= \frac{\partial}{\partial T_e} \int_0^\infty \nu(\epsilon)\, \epsilon \left[f_{\text{FD}}(\epsilon; \mu, T_e) + f_{\text{FD}}(\epsilon; -\mu, T_e) \right] d\epsilon. \end{aligned} \tag{2.18}$$

The electronic heat capacity depends strongly on the position of the Fermi level relative to the thermal energy scale $k_B T_e$. There are two limiting regimes usually distinguished. The first corresponds to a finite-density, or degenerate, carrier system, where the Fermi energy is much larger than the thermal energy. While, the second one corresponds to the charge-neutrality regime, where the Fermi energy is small compared with $k_B T_e$. These two regimes lead to different temperature dependencies of the electronic heat capacity [41].

In the degenerate finite-density regime, $k_B T_e \ll E_F$, the electronic heat capacity is given by [42]

$$c_e^{\text{deg}} = \frac{2\pi E_F}{3(\hbar v_F)^2} k_B^2 T_e, \qquad k_B T_e \ll E_F. \tag{2.19}$$

In this regime, the heat capacity is proportional to both the Fermi energy and the carrier temperature. This occurs because only carriers within an energy window of order $k_B T_e$ around the Fermi level can be thermally excited. Therefore, a larger E_F corresponds to a larger density of available electronic states and, consequently, to a larger electronic heat capacity. In

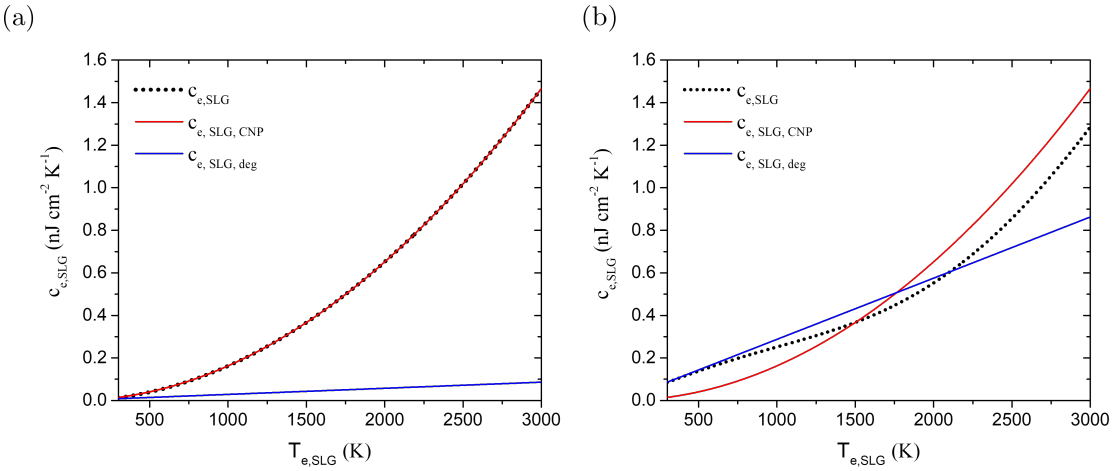

Figure 2.4: Electronic heat capacity of single-layer graphene as a function of carrier temperature for (a) $E_F = 0.05\ eV$ and (b)$E_F = 0.5\ eV$. The numerical result is compared with the analytical limiting expressions for the charge-neutral regime, $c_e \propto T_e^2$, and the degenerate finite-density regime, $c_e \propto E_F T_e$.

the opposite limit, close to the CNP, where $k_B T_e \gg E_F$, the heat capacity becomes [43]

$$c_e^{\text{CNP}} = \frac{18\zeta(3)}{\pi(\hbar v_F)^2} k_B^3 T_e^2, \qquad k_B T_e \gg E_F \tag{2.20}$$

here, $\zeta(3) \simeq 1.202$ is Apéry's constant. In this regime, the electronic heat capacity is independent of E_F, because thermal excitation dominates over the equilibrium carrier density. Electron-hole pairs are thermally populated around the Dirac point, leading to the quadratic temperature dependence $c_e \propto T_e^2$.

Figure 2.4 illustrates these two limiting behaviours by comparing the numerically calculated electronic heat capacity, Eq. (2.18), with the analytical expressions given in Eqs. (2.19) and (2.20).

2.2 Optical Properties of Graphene

The optical response of a material originates from the motion of its charged particles under the action of an external electromagnetic field. In conventional bulk media, this response is commonly described through the induced polarization density **P**, which represents the electric dipole moment per unit volume. In the linear regime, the polarization is proportional to the applied electric field [44],

$$\mathbf{P}^{(1)}(\omega) = \varepsilon_0 \chi^{(1)}(\omega)\mathbf{E}(\omega), \tag{2.21}$$

where $\chi^{(1)}$ is the linear electric susceptibility.

The role of the induced polarization becomes evident from the electromagnetic wave equation. In a non-magnetic medium without free-current sources, Maxwell's equations give [44, 45]

$$\nabla \times \nabla \times \mathbf{E} + \frac{1}{c^2}\frac{\partial^2 \mathbf{E}}{\partial t^2} = -\mu_0 \frac{\partial^2 \mathbf{P}}{\partial t^2}. \tag{2.22}$$

Equation (2.22) shows that each temporal-frequency component of the induced polarization acts as a source for an electromagnetic field at the same frequency. In the linear regime, the polarization contains only the frequencies already present in the applied field. Higher-order polarization terms can additionally generate new frequency components or modify the response at the original frequency. For atomically thin graphene, the corresponding electromagnetic source is more naturally expressed as a surface current density, as introduced below.

For a harmonic time dependence $e^{-i\omega t}$, the time derivative of the polarization gives rise to a polarization current density [46, 47],

$$\mathbf{J}^{(1)}(\omega) = \frac{\partial \mathbf{P}^{(1)}}{\partial t} = \sigma^{(1)}(\omega)\mathbf{E}(\omega). \tag{2.23}$$

The quantity $\sigma^{(1)}_{\mathrm{SLG}}$ is therefore a sheet optical conductivity, with units of Siemens. If graphene is treated as an effective thin film of thickness d_{SLG}, its sheet conductivity can be written as [48]

$$\sigma^{(1)}(\omega) = -i\omega\varepsilon_0 d_{\mathrm{SLG}} \chi^{(1)}(\omega). \tag{2.24}$$

2.2.1 Linear Optical Conductivity

As mentioned before, due to its atomically thin nature, the optical response of single-layer graphene is described through its complex sheet optical conductivity [46]. This quantity is

obtained from the Kubo formalism and depends on the angular frequency of the incident field ω, the chemical potential μ, and the electronic temperature T [46,47]. The total linear optical conductivity can be separated into an intraband and an interband contribution,

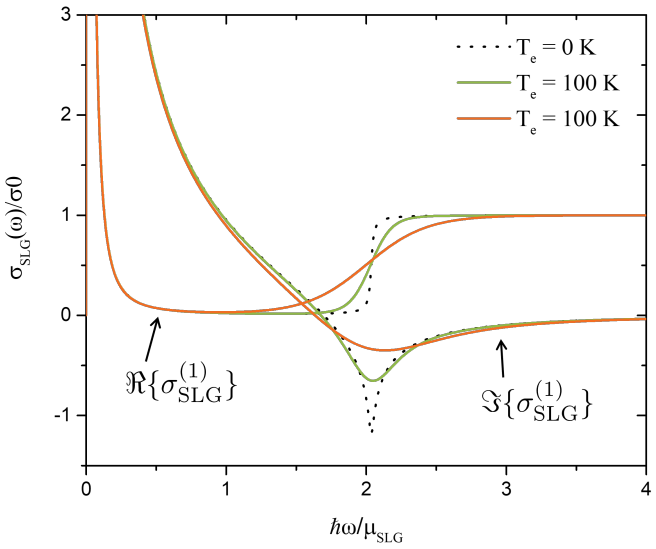

Figure 2.5: The real and imaginary parts of the optical conductivity of doped SLG as a function of photon energy, normalized to the universal value $\sigma_0 = e^2/4\hbar$, for $T_{e,\mathrm{SLG}} = 0\ \mathrm{K}, 100\ \mathrm{K}, 300\ \mathrm{K}$, $\tau_{\mathrm{opt}} = 200$ fs and $E_{F,\mathrm{SLG}} = 0.25$ eV.

$$\sigma^{(1)}(\omega;\mu,T_e) = \sigma^{(1)}_{\mathrm{intra}}(\omega;\mu,T_e) + \sigma^{(1)}_{\mathrm{inter}}(\omega;\mu,T_e). \tag{2.25}$$

The intraband term describes the response of carriers driven within the same band. In the Kubo formalism it is written as [46,47]

$$\sigma^{(1)}_{\mathrm{intra}} = \frac{ie^2}{\pi\hbar^2\Omega}\int_0^\infty \varepsilon\left[\frac{\partial f_{\mathrm{FD}}(-\varepsilon;\mu,T_e)}{\partial\varepsilon} - \frac{\partial f_{\mathrm{FD}}(\varepsilon;\mu,T_e)}{\partial\varepsilon}\right]d\varepsilon. \tag{2.26}$$

The interband term, on the other hand, accounts for optical transitions between the valence and conduction bands and is given by [46,47]

$$\sigma^{(1)}_{\mathrm{inter}} = \frac{ie^2\Omega}{\pi\hbar^2}\int_0^\infty \frac{f_{\mathrm{FD}}(-\varepsilon;\mu,T_e) - f_{\mathrm{FD}}(\varepsilon;\mu,T_e)}{\Omega^2 - 4(\varepsilon/\hbar)^2}d\varepsilon. \tag{2.27}$$

Here, $\Omega = \omega + i\tau_{\mathrm{opt}}^{-1}$, where τ_{opt} is an effective optical relaxation time that introduces a finite broadening of the optical transitions and is commonly related to carrier scattering processes [46].

The distinction between the two contributions is illustrated in Fig. 2.6. Interband optical transitions are vertical in k-space due to energy and momentum conservation [49]. In doped graphene, however, interband transitions are suppressed for photon energies $\hbar\omega < 2|\mu|$, because the required initial and final electronic states are not simultaneously available. This

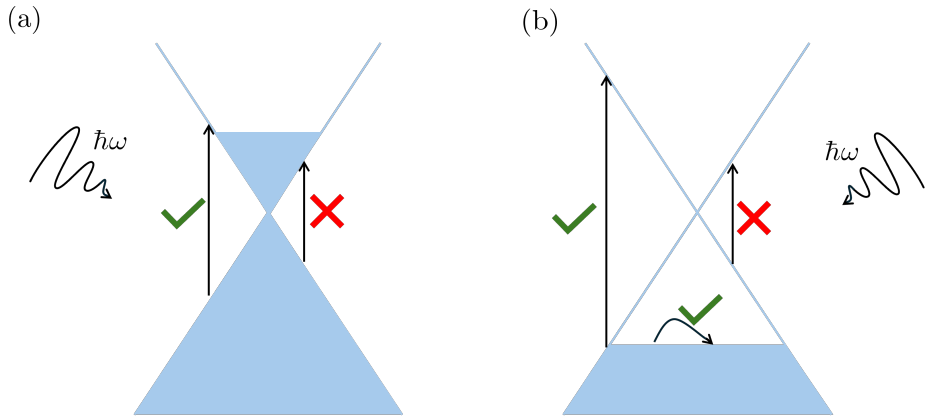

Figure 2.6: Schematic illustration of optical transitions in doped graphene for photon energies below the interband threshold. (a) n-doped graphene, where states in the conduction band are partially occupied. (b) p-doped graphene, where states near the top of the valence band are partially empty. In both cases, interband absorption can be suppressed by Pauli blocking, because the required initial or final electronic states are not available. The green marks indicate allowed intraband and interband carrier excitation, while the red crosses indicate forbidden interband transitions.

suppression is known as Pauli blocking [46]. The onset of interband absorption therefore occurs at $\hbar\omega = 2|\mu|$ for $T_e = 0K$. Above this threshold, interband transitions become allowed and dominate the absorptive part of the optical conductivity.

This behavior is reflected in the frequency dependence of the complex optical conductivity shown in Fig. 2.5. The plotted quantity is normalized to the universal value $\sigma_0 = e^2/4\hbar$. For $\hbar\omega \geq 2|\mu|$, the real part of the conductivity approaches σ_0, indicating the onset of the universal interband optical response of Dirac fermions in SLG [12, 47, 50]. Just below this threshold, $\mathrm{Re}\{\sigma^{(1)}\}$ becomes minimal, corresponding to suppressed absorption and increased optical transparency.

For photon energies well below the interband threshold, $\hbar\omega \ll 2|\mu_{\mathrm{SLG}}|$, graphene's optical response is mainly governed by free-carrier absorption, described by the intraband contribution to the conductivity. In the degenerate regime, where $k_B T_e \ll |\mu| \approx E_F$, Eq. (2.26) reduces to a Drude-like form [46, 51]

$$\sigma^{(1)}_{\mathrm{intra}} \approx \frac{ie^2}{\pi\hbar^2} \frac{\mu}{\omega + i\tau^{-1}_{\mathrm{opt}}}. \tag{2.28}$$

This low-energy, intraband-dominated regime extends from the mid-infrared down to the THz spectral range, where the optical conductivity depends strongly on the effective relaxation time τ_{opt}. The latter is influenced by carrier scattering mechanisms associated with impurities, defects, wrinkles, substrate interactions and other non-uniformities [52].

At $T_e = 0$ K, the transition at $\hbar\omega = 2|\mu|$ appears as a sharp step in $\mathrm{Re}\{\sigma^{(1)}_{\mathrm{SLG}}\}$. At finite electronic temperature, this edge is broadened because the Fermi–Dirac distribution is thermally smeared. Increasing T_e therefore widens the transition region around the threshold, as shown in Fig. 2.5. The imaginary part exhibits a corresponding dispersive feature near the interband threshold [47].

By applying Maxwell's boundary conditions at the graphene interface, the absorbance of suspended SLG is directly related to the real part of its optical sheet conductivity [53]

$$a \simeq \frac{\mathrm{Re}\{\sigma^{(1)}\}}{\epsilon_0 c}, \tag{2.29}$$

where ϵ_0 is the vacuum permittivity and c is the speed of light in vacuum. When the interband response reaches the universal conductivity $\sigma_0 = e^2/4\hbar$, Eq. (2.29) gives $a \simeq \frac{e^2}{4\hbar\epsilon_0 c} = \pi\alpha \simeq 2.3\%$, with $\alpha = e^2/(4\pi\hbar\epsilon_0 c)$ being the fine-structure constant [12].

2.2.2 Nonlinear Optical Conductivity

The linear optical response discussed in the previous section assumes that the induced polarization is proportional to the applied electric field. This approximation is valid when nonlinear corrections are negligible. When these corrections remain within the perturbative regime, the induced polarization can be expanded in powers of the applied electric field [45]

$$\mathbf{P} = \mathbf{P}^{(1)} + \mathbf{P}^{(2)} + \mathbf{P}^{(3)} + \cdots . \tag{2.30}$$

In component form, the first three polarization contributions are [45]

$$P_i^{(1)} = \varepsilon_0 \sum_j \chi_{ij}^{(1)} E_j, \tag{2.31}$$

$$P_i^{(2)} = \varepsilon_0 \sum_{jk} \chi_{ijk}^{(2)} E_j E_k, \tag{2.32}$$

$$P_i^{(3)} = \varepsilon_0 \sum_{jkl} \chi_{ijkl}^{(3)} E_j E_k E_l. \tag{2.33}$$

Here, i, j, k, l denote Cartesian components, and $\chi^{(n)}$ is the n-th-order optical susceptibility tensor. The second-order susceptibility describes processes such as second-harmonic, sum-frequency and difference-frequency generation. The third-order susceptibility describes processes including third-harmonic generation, Kerr-type self-action, two-photon absorption and four-wave mixing [45].

In centrosymmetric media, the local electric-dipole second-order response vanishes [45]. Consequently, for ideal centrosymmetric single-layer graphene, the lowest-order intrinsic local electric-dipole nonlinearity is the third-order response. Effective second-order contributions may nevertheless arise when inversion symmetry is broken, for example by a substrate, an external dc field or another asymmetric perturbation [54, 55].

In the frequency domain, the third-order polarization generated at the output frequency

$$\omega_\Sigma = \omega_1 + \omega_2 + \omega_3 \tag{2.34}$$

is written as

$$P_i^{(3)}(\omega_\Sigma) = \varepsilon_0 \sum_{jkl} \chi_{ijkl}^{(3)}(\omega_\Sigma; \omega_1, \omega_2, \omega_3) E_j(\omega_1) E_k(\omega_2) E_l(\omega_3). \tag{2.35}$$

The frequency arguments ω_1, ω_2 and ω_3 may be positive or negative. Because the physical electric field is real, its frequency components satisfy $E_j(-\omega) = E_j^*(\omega)$.

The frequency combinations produced by a third-order response can be seen directly by considering a monochromatic field linearly polarized along the x-direction,

$$\widetilde{E}_x(t) = E_x(\omega)e^{-i\omega t} + E_x^*(\omega)e^{i\omega t}. \tag{2.36}$$

Its cubic power is

$$\left[\widetilde{E}_x(t)\right]^3 = E_x^3(\omega)e^{-3i\omega t} + 3|E_x(\omega)|^2 E_x(\omega)e^{-i\omega t} + \text{c.c.} \tag{2.37}$$

The first positive-frequency term results from the combination $\omega + \omega + \omega = 3\omega$ and drives a nonlinear response at the third-harmonic frequency. The second positive-frequency term results from $\omega + \omega - \omega = \omega$ and therefore remains at the fundamental frequency.

The third-order sheet-current contribution generated by the frequency triplet $(\omega_1, \omega_2, \omega_3)$ is written as [54–56]

$$J_i^{(3)}(\omega_\Sigma) = \sum_{jkl} \sigma_{ijkl}^{(3)}(\omega_\Sigma; \omega_1, \omega_2, \omega_3) E_j(\omega_1) E_k(\omega_2) E_l(\omega_3), \tag{2.38}$$

where $\sigma_{ijkl}^{(3)}$ is the third-order nonlinear surface-conductivity tensor of graphene. For the monochromatic field of Eq. (2.36), the third-harmonic surface current is

$$J_x^{(3)}(3\omega) = \sigma_{xxxx}^{(3)}(3\omega; \omega, \omega, \omega) E_x^3(\omega), \tag{2.39}$$

whereas the nonlinear current at the fundamental frequency is

$$J_x^{(3)}(\omega) = 3\sigma_{xxxx}^{(3)}(\omega; \omega, \omega, -\omega)|E_x(\omega)|^2 E_x(\omega). \tag{2.40}$$

The current $J_x^{(3)}(3\omega)$ acts as a source of radiation at the third-harmonic frequency, whereas $J_x^{(3)}(\omega)$ modifies the optical response at the incident frequency. In the latter case, the real part of $\sigma_{xxxx}^{(3)}(\omega; \omega, \omega, -\omega)$ modifies the absorptive response, while its imaginary part modifies the phase of the fundamental field [55, 56].

Panels (a) and (b) of Fig. 2.7 show representative time orderings of the interactions $(\omega, \omega, -\omega)$ that contribute to the nonlinear current at the fundamental frequency. The final downward transition represents emission of the nonlinear response, both pathways therefore contribute to $J_x^{(3)}(\omega)$ [45]. The nonlinear correction at the fundamental frequency is shown in Fig. 2.8. The spectra were calculated using the perturbative expressions for the third-order conductivity of graphene reported in Refs. [55, 56].

In the low-energy limit $\hbar\omega \ll |\mu_{\text{SLG}}|$, interband transitions are strongly Pauli blocked, and the response is dominated by intraband carrier dynamics [56, 57]. As shown in Fig. 2.8, at zero electronic temperature, three spectral regimes can be distinguished. For $\hbar\omega < |\mu_{\text{SLG}}|$, both one-photon and two-photon interband absorption are Pauli blocked. In the ideal lossless limit, the real part of the perturbative nonlinear conductivity vanishes, while its imaginary part describes a dispersive nonlinear response. At $\hbar\omega = |\mu_{\text{SLG}}|$, the two-photon absorption threshold is reached. For $|\mu_{\text{SLG}}| < \hbar\omega < 2|\mu_{\text{SLG}}|$, two-photon absorption is allowed, while

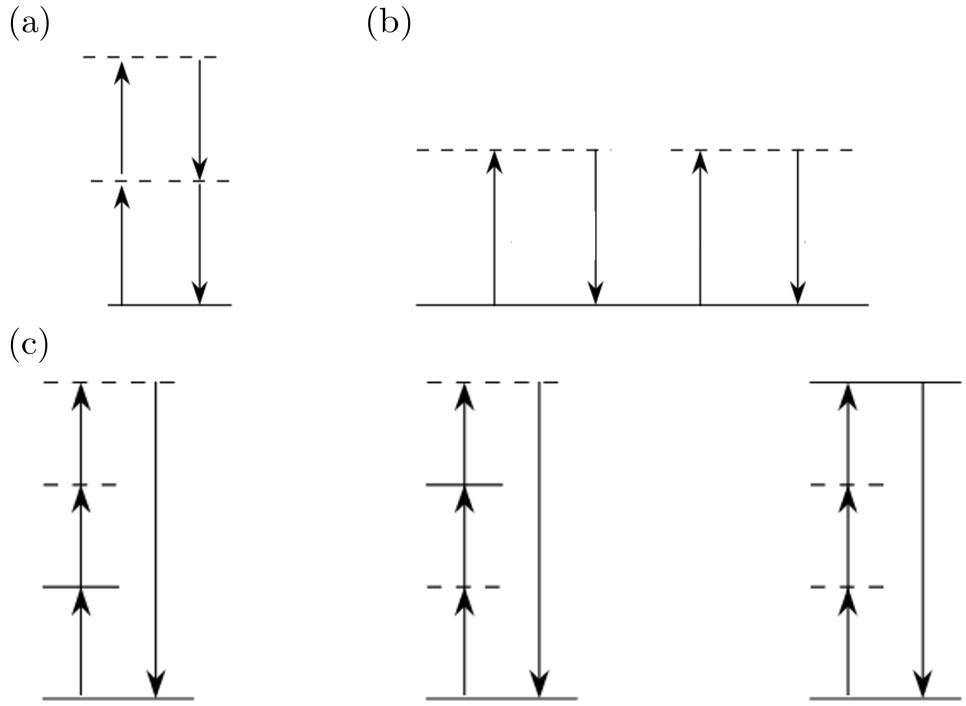

Figure 2.7: Representative quantum-mechanical pathways contributing to the third-order optical response. (a) Two successive absorptive interactions are followed by an interaction with the complex-conjugate field component and emission of the nonlinear response at ω. (b) An alternating absorption–emission–absorption sequence, followed by emission at ω. (c) Third-harmonic-generation pathways under one-, two-, and three-photon resonance conditions, shown from left to right. In panel (c), the solid intermediate level identifies the stage at which the accumulated photon energy becomes resonant with an electronic transition, whereas the dashed levels represent off-resonant intermediate states.

one-photon interband absorption remains Pauli blocked. Finally, for $\hbar\omega > 2|\mu_{\mathrm{SLG}}|$, one-photon interband absorption also becomes allowed, and $\sigma^{(3)}_{xxxx}(\omega;\omega,\omega,-\omega)$ acts as a perturbative correction to an already active linear absorption channel [55]. Increasing the electronic temperature smooths these thresholds through the thermal broadening of the Fermi–Dirac distribution [55].

The three pathways in Fig. 2.7(c) represent resonant structures that arise when one, two, or three incident photons bridge the Pauli-blocking edge $2|\mu_{\mathrm{SLG}}|$ [45]:

$$\hbar\omega = 2|\mu_{\mathrm{SLG}}|, \qquad 2\hbar\omega = 2|\mu_{\mathrm{SLG}}|, \qquad 3\hbar\omega = 2|\mu_{\mathrm{SLG}}|. \tag{2.41}$$

The resonant features of $\sigma^{(3)}_{xxxx}(3\omega;\omega,\omega,\omega)$ are shown in Fig. 2.9. The conductivity was calculated using the perturbative third-order formalism of Refs. [54,58]. Because the resonance conditions depend on μ_{SLG}, electrostatic control of the carrier density shifts the corresponding resonant photon energies and provides a means of tuning the nonlinear optical response of graphene [41].

The perturbative third-order conductivity is useful for identifying nonlinear optical channels, resonant spectral features, and the leading weak-field correction associated with the onset of absorption bleaching. It does not, however, provide a complete description of graphene

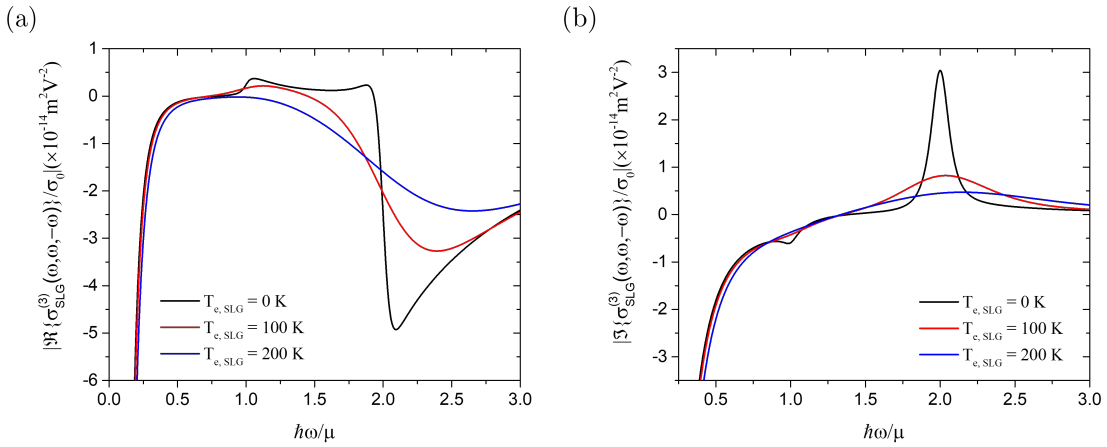

Figure 2.8: (a) Real and (b) imaginary parts of the third-order nonlinear conductivity at the fundamental frequency, $\sigma^{(3)}_{xxxx}(\omega;\omega,\omega,-\omega)$, as a function of photon energy for $E_F = 0.1$ eV. The spectra compare the zero-temperature and finite-temperature responses.

saturable absorption over the full saturation regime. In perturbative density-matrix treatments, the electronic response is expanded about the equilibrium density matrix $\hat{\rho}^{(0)}$, whose diagonal elements are determined by the equilibrium Fermi–Dirac occupations, and the expansion is retained only up to third-order in the electric field [54–56]. Consequently, field-induced changes in the band populations enter only as finite-order corrections, rather than through a non-perturbative evolution of the carrier populations without truncation in the field amplitude. This distinction becomes essential in the saturation regime. Interband photoexcitation progressively depletes occupied valence-band states and populates the corresponding conduction-band states, thereby reducing the occupation difference that drives interband absorption. The resulting Pauli blocking suppresses further optical transitions and drives the absorption toward an intensity-dependent saturated value. As emphasized by Marini et al., graphene saturable absorption is inherently non-perturbative and cannot be accurately described over the full saturation range by a standard finite-order expansion of the nonlinear conductivity [16]. For completeness, third-harmonic generation was also evaluated to determine whether energy transfer to the third-harmonic field could influence the calculated optical response. Under the conditions considered here, the generated third-harmonic intensity was found to be negligible and therefore does not affect the results or conclusions for the devices studied, as demonstrated in Appendix **??**.

Accordingly, the intensity-dependent absorption considered in the following sections is calculated from the evolving nonequilibrium carrier distributions and their relaxation toward thermalized hot-carrier distribution. Carrier redistribution, Pauli blocking, electronic heating, and relaxation are therefore included explicitly, rather than represented through a fixed equilibrium third-order conductivity.

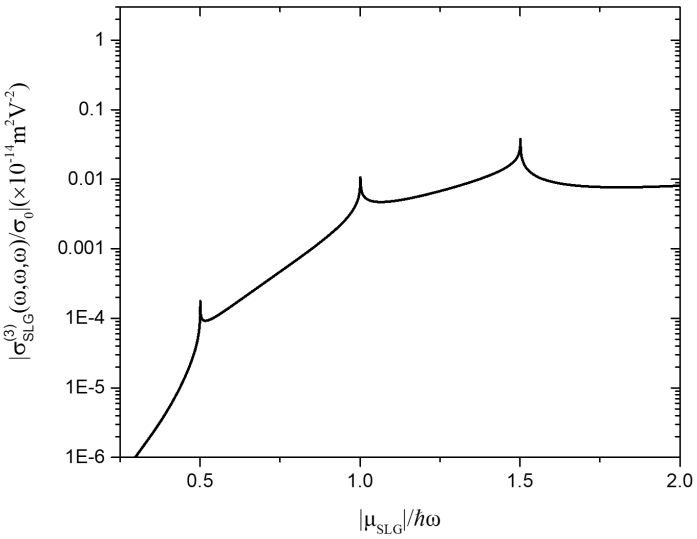

Figure 2.9: Magnitude of the third-order nonlinear conductivity of graphene for third-harmonic generation, $\sigma^{(3)}_{xxxx}(3\omega;\omega,\omega,\omega)$, normalized to $\sigma_0 = e^2/(4\hbar)$, as a function of $|\mu_{\mathrm{SLG}}|/(\hbar\omega)$, calculated for $\mu_{\mathrm{SLG}} = E_F = 0.25$ eV and $T_{e,\mathrm{SLG}} = 0$ K.

2.2.3 Dielectric Function and Refractive Index

Using the effective film thickness d_{SLG}, for graphene, introduced previously, the sheet optical conductivity of single-layer graphene can be related to an effective dielectric function as [46],

$$\varepsilon\left(\omega,\mu,T_e\right) = \varepsilon_\infty + \frac{i\sigma^{(1)}\left(\omega,\mu,T_e\right)}{\varepsilon_0\omega d_{\mathrm{SLG}}}. \tag{2.42}$$

Here $\sigma^{(1)}$ is the complex linear optical conductivity of graphene, ε_0 is the vacuum permittivity, and $d_{\mathrm{SLG}} = 0.335$ nm is the thickness of one graphene layer. The parameter $\varepsilon_\infty = 5.7$ accounts for the high-frequency background contribution used in this effective-film description. In this section, only the linear optical response is considered.

The complex refractive index is defined as [44]

$$\tilde{n} = n + i\kappa, \tag{2.43}$$

where n is the real refractive index and κ is the extinction coefficient. For non-magnetic media, the dielectric function and the complex refractive index are related through [44]

$$\tilde{n}^2 = \varepsilon. \tag{2.44}$$

By substituting Eq. (2.43) into Eq. (2.44), one obtains

$$\mathrm{Re}\left(\varepsilon\right) = n^2 - \kappa^2, \tag{2.45}$$

and

$$\mathrm{Im}\,(\varepsilon) = 2n\kappa. \tag{2.46}$$

These relations allow the refractive index of graphene to be calculated directly from its optical conductivity.

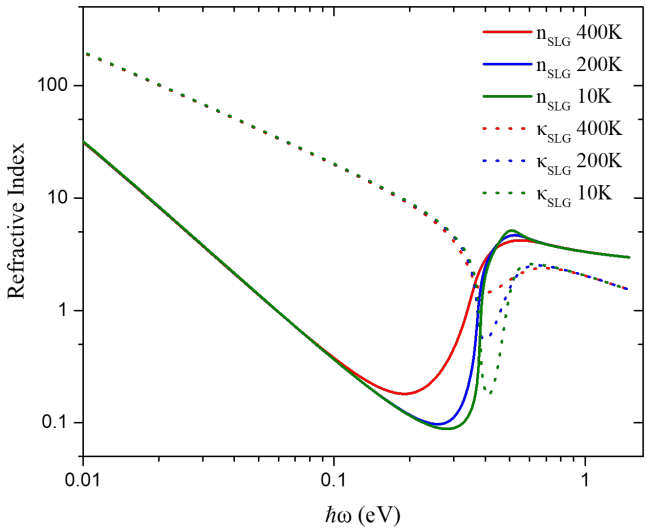

Figure 2.10: Real n and imaginary κ parts of the effective refractive index of single-layer graphene as a function of photon energy $\hbar\omega$. The green, blue and red curves correspond to electronic temperatures $T_e = 10$ K, $T_e = 200$ K and $T_e = 400$ K, respectively. The calculation was performed for $\tau_{\text{opt}} = 100$ fs and $E_F = 0.25$ eV.

Figure 2.10 shows the refractive index of single-layer graphene for three electronic temperatures. Both n and κ vary with photon energy, reflecting the frequency dependence of the graphene optical conductivity. The temperature dependence is more pronounced near the interband absorption threshold, $\hbar\omega \simeq 2|\mu|$, where the optical response changes from an intraband-dominated regime to interband absorption.

2.3 Photoexcited Carriers in Graphene

2.3.1 Carrier Heating

Optical absorption in graphene initially drives the electronic system out of equilibrium by generating high-energy carriers. Depending on the photon energy relative to the Fermi level, this excitation can occur through interband transitions, for $\hbar\omega > 2|E_F|$, where electron–hole pairs are created across the Dirac point, or through intraband absorption, for $\hbar\omega < 2|E_F|$, where the optical field mainly accelerates already existing free carriers within the partially filled band [13, 20]. These initially non-equilibrium carriers subsequently redistribute their

excess energy and momentum mainly through Coulomb-mediated carrier–carrier scattering. This internal thermalization occurs on time scales of tens of femtoseconds, with ultrafast pump–probe measurements and microscopic calculations giving a typical electron–electron relaxation time of $\tau_{e-e} \sim 20$ fs [19, 21]. After this redistribution, the electronic population can be described by a hot Fermi–Dirac distribution characterized by an elevated electronic temperature T_e, which exceeds the lattice temperature T_l [13, 59]. The microscopic carrier–carrier scattering processes responsible for carrier heating can be classified into intraband and interband channels [13, 59]. In doped graphene, where $|E_F| \gg k_B T_e$, thermalization occurs predominantly within a single band and is governed mainly by intraband carrier–carrier scattering. In contrast, close to the Dirac point, where $|E_F| \ll k_B T_e$, interband thermalization becomes important, and the electronic redistribution can involve both the valence and conduction bands [13]. The two main interband Auger-type processes are impact ionization and Auger recombination [13, 60]. In impact ionization, a high-energy carrier loses part of its excess energy, while another carrier is promoted from the valence band to the conduction band, increasing the number of electron–hole pairs. Auger recombination is the reverse process, in which an electron recombines from the conduction band to the valence band and transfers its energy to another carrier [60]. These interband processes can contribute to carrier multiplication, particularly near the charge-neutrality point [13, 19, 60].

Although interband photoexcitation occurs when $\hbar\omega > 2|E_F|$, the subsequent relaxation of the generated high-energy carriers does not necessarily proceed through interband thermalization. In this regime, a primary high-energy carrier can relax through intraband inelastic scattering by transferring part of its excess energy to carriers in the Fermi sea [13, 61]. In this cascade, the total carrier density within the band remains approximately conserved, whereas the density of hot carriers increases [13, 62]. Since the average energy exchanged in each scattering event, $\Delta\varepsilon$, follows a distribution that peaks around the Fermi energy, a single primary carrier can generate several secondary hot carriers before relaxing toward the Fermi level [13, 61]. This process is referred to as hot-carrier multiplication [61, 62].

For intraband optical excitation, where $\hbar\omega < 2|E_F|$, the initial excitation step is different because no direct interband electron–hole pair generation occurs. Instead, the optical field accelerates free carriers within the partially filled band. These energized carriers subsequently redistribute their excess energy through carrier–carrier scattering with the surrounding carriers in the Fermi sea, leading again to internal thermalization and to the formation of a hot-carrier distribution [13, 20, 63].

The elevated electronic temperature directly affects graphene's optical response. Since graphene's optical conductivity depends on the carrier distribution, carrier heating modifies the occupation probabilities of the electronic states involved in optical transitions and can therefore change both intraband and interband absorption.

2.3.2 Carrier cooling

After the rapid carrier–carrier thermalization discussed above, the electronic system of graphene can be described by a hot Fermi–Dirac distribution with an electronic temperature T_e higher than the lattice temperature T_l and chemical potential $\mu(T_e)$ [63–65]. Carrier cooling refers to the subsequent relaxation of the electronic energy stored in the hot-carrier distribution. In

contrast to carrier–carrier scattering, which redistributes energy within the electronic subsystem and establishes internal thermal equilibrium, electron–phonon scattering transfers energy from the carrier bath to phonons and drives T_e towards T_l [13, 65–67]. This separation between ultrafast electronic thermalization and slower energy relaxation has been observed experimentally in pump–probe spectroscopy and time-resolved THz measurements [63–65, 68].

In graphene devices, the hot-carrier energy can relax through different pathways. In device geometries with non-uniform excitation, the electronic temperature can decrease through in-plane heat diffusion away from the initially heated region [13]. In supported graphene, an additional out-of-plane cooling pathway may arise from coupling to substrate phonons, especially for polar substrates [13, 69]. In this context, however, carrier cooling is described only through electron–phonon energy transfer, namely optical-phonon scattering and disorder-assisted acoustic-phonon supercollision cooling. The total electron–phonon thermal current density is therefore written as

$$J_{e-\mathrm{ph}} = J_{\mathrm{OP}} + J_{\mathrm{SC}}, \tag{2.47}$$

where J_{OP} is the thermal current density associated with optical-phonon scattering and J_{SC} is the thermal current density associated with disorder-assisted acoustic-phonon supercollisions [66, 70].

The relative importance of J_{OP} and J_{SC} is not universal, and remains dependent on graphene quality, carrier mobility, disorder, carrier density, Fermi energy, and electronic temperature [13, 65]. The relative importance of optical-phonon and supercollision cooling depends on both the electronic temperature and the degree of disorder [13, 65]. In high-quality graphene, disorder-assisted processes are weaker and optical-phonon cooling is often expected to provide a dominant electron–phonon cooling pathway [65]. In contrast, in graphene with higher impurity concentration, in graphene supported by conventional dielectric substrates, or in nanostructured graphene where the effective mean free path is reduced, disorder-assisted supercollision cooling can become comparable to or even dominate the electron–phonon cooling pathway [70–72].

Graphene possesses strongly coupled optical phonon modes near the Γ and K points of the Brillouin zone [28, 73, 74]. The corresponding phonon energies are approximately $\hbar\Omega_\Gamma \simeq 196$ meV and $\hbar\Omega_K \simeq 161$ meV [64, 67]. The Γ-point optical phonons mainly induce intravalley scattering, whereas the K-point optical phonons are associated with intervalley carrier scattering [67]. When the hot-carrier distribution contains carriers with sufficient energy, optical-phonon emission can efficiently transfer energy from the electronic system to the optical-phonon bath [65, 66]. This cooling mechanism has been observed in ultrafast pump–probe experiments and supported by microscopic theoretical studies [63–65]. The optical-phonon cooling thermal current density can be written as [69, 75]

$$\begin{aligned} J_{\mathrm{OP}}(\mu, T_e, T_l) = \sum_i \frac{9\hbar\Omega_i^3 \left(\gamma_0'\right)^2}{\pi \left(\hbar v_F\right)^4 \rho} \times \left[N\left(\frac{\hbar\Omega_i}{k_B T_e}\right) - N\left(\frac{\hbar\Omega_i}{k_B T_l}\right) \right] \\ \times \mathcal{F}_i(\mu, T_e), \end{aligned} \tag{2.48}$$

where the summation is performed over the optical phonon branches at the Γ and K points [67]. Here, $N(x) = (e^x - 1)^{-1}$ is the Bose distribution, ρ is the mass density of graphene, v_F is the Fermi velocity, and γ_0' is the derivative of the nearest-neighbor hopping energy with

respect to the carbon–carbon bond length [66,67]. The function $\mathcal{F}_i$ accounts for the available electronic phase space for phonon emission and absorption and is given by [75]

$$\mathcal{F}_i\left(\mu, T_e\right) = \int_{-\infty}^{\infty} |x(1-x)| \left\{ f_{\mathrm{FD}}\left[\hbar\Omega_i(x-1); \mu, T_e\right] - f_{\mathrm{FD}}\left[\hbar\Omega_i x; \mu, T_e\right] \right\} dx. \tag{2.49}$$

For $T_e > T_l$, the difference between the Bose occupation factors in Eq. (2.48) gives a net energy flow from the electronic system to the optical phonon bath.

In addition to optical-phonon emission, hot carriers can lose energy through acoustic phonons [66,75]. In disorder-free graphene, however, momentum-conserving acoustic-phonon cooling is strongly constrained [75]. Because the Fermi velocity of graphene carriers is much larger than the sound velocity, $v_F \gg v_s$, only a small amount of energy can be transferred in a single acoustic-phonon scattering event while simultaneously satisfying energy and momentum conservation [66, 70]. As a result, ordinary acoustic-phonon cooling can be inefficient and may fail to explain experimentally observed picosecond cooling rates in graphene devices [70, 71].

This acoustic-phonon cooling bottleneck can be bypassed by disorder-assisted electron–phonon scattering, known as supercollision cooling [70]. In a supercollision process, disorder provides the additional momentum required for the emission of acoustic phonons with larger momenta and therefore larger energies than those allowed in ordinary momentum-conserving acoustic-phonon scattering [70, 72]. Consequently, supercollisions can provide an efficient pathway for transferring electronic heat to the lattice [71, 72]. In the degenerate regime, the corresponding cooling power density is written as [70–72]

$$J_{\mathrm{SC}}\left(\mu, T_e, T_l\right) = \gamma_{\mathrm{SC}}\left(T_e^3 - T_l^3\right), \tag{2.50}$$

where γ_{SC} is the supercollision cooling coefficient. For short-range disorder-assisted scattering, it can be expressed as [27]

$$\gamma_{\mathrm{SC}} = \frac{9.62 D^2 k_B^3}{2\rho s^2 \hbar k_F l} \frac{4\left(n_e + n_h + 2n_{ne}\right)}{\pi\left(\hbar v_F\right)^4}, \tag{2.51}$$

where D is the deformation potential for supercollision scattering, estimated between 10 and 30 eV [59, 70], s is the sound velocity, k_F is the Fermi wavevector, and l is the mean free path associated with short-range disorder [70]. The product $k_F l$ acts as a disorder parameter: smaller values correspond to stronger disorder and therefore stronger supercollision cooling [70–72]. The quantities n_e and n_h are the electron and hole densities, while n_{ne} denotes the nonequilibrium photoexcited carrier density. Although the cubic supercollision law is originally derived in the degenerate limit [70], its use can be extended phenomenologically to higher carrier temperatures by including the total available carrier density through n_e, n_h, and n_{ne} [27]. Time-resolved photocurrent and noise-thermometry measurements have shown cooling dynamics consistent with this cubic temperature dependence, supporting the role of disorder-assisted supercollisions as an efficient picosecond-scale cooling mechanism in graphene [71, 72].

2.4 Bragg Mirrors and Fabry–Pérot Cavities

A dielectric Bragg mirror, also known as a distributed Bragg reflector (DBR), is a one-dimensional photonic crystal formed by a periodic sequence of dielectric layers with different refractive indices [76, 77]. Its operation originates from the periodic modulation of the dielectric function, which couples forward- and backward-propagating waves through Bragg scattering and opens frequency intervals where propagating Bloch modes are not allowed in the corresponding infinite periodic structure [76, 77]. In the one-dimensional case, these forbidden frequency intervals are commonly referred to as stop bands, or photonic band gaps [76, 77].

The physical origin of the stop band can be understood by first considering a homogeneous medium. In that case, the electromagnetic modes are plane waves with dispersion [77]

$$\omega(k) = \frac{c}{n}|k|, \tag{2.52}$$

where n is the refractive index of the medium. If an artificial period a is assigned to this otherwise homogeneous system, the same dispersion can be folded into the first Brillouin zone [77],

$$-\frac{\pi}{a} \leq k \leq \frac{\pi}{a}. \tag{2.53}$$

This folding alone does not change the physical modes; it only relabels equivalent wavevectors that differ by integer multiples of $2\pi/a$. At the Brillouin-zone boundary, $k = \pm\pi/a$, the forward- and backward-propagating waves become degenerate and can equivalently be written as standing waves with even and odd spatial profiles, such as $\cos(\pi z/a)$ and $\sin(\pi z/a)$ [77]. This band-folding picture, together with the corresponding gap opening produced by a real periodic dielectric modulation, is summarized schematically in Fig. 2.11.

In a real DBR, the periodicity is not artificial but arises from the alternating dielectric layers, as shown in Fig. 2.11(a). The periodic refractive-index modulation lifts the degeneracy between the two counter-propagating waves at the Brillouin-zone edge, as illustrated in Fig. 2.11(c) [76, 77]. The resulting standing-wave modes have different spatial overlap with the high- and low-index regions: the mode whose electric-field energy is concentrated more strongly in the high-index regions lies at lower frequency, whereas the mode with larger weight in the low-index regions lies at higher frequency [77]. The frequency separation between these two modes forms the stop band of the one-dimensional periodic structure [76, 77].

For a finite multilayer stack, frequencies inside the stop band do not propagate efficiently through the structure. Instead, the optical field decays inside the periodic medium, and incident light in this spectral range is strongly reflected [77]. Therefore, a DBR can behave as a high-reflectivity mirror even when all individual layers are transparent dielectrics [76, 77]. Increasing the number of layer pairs increases the reflectivity because the partial reflections from successive interfaces add coherently, while the residual field inside the mirror decays evanescently with depth [77]. The stop-band width is mainly controlled by the refractive-index contrast: a larger contrast produces stronger Bragg scattering and therefore a broader high-reflectivity region [76–78].

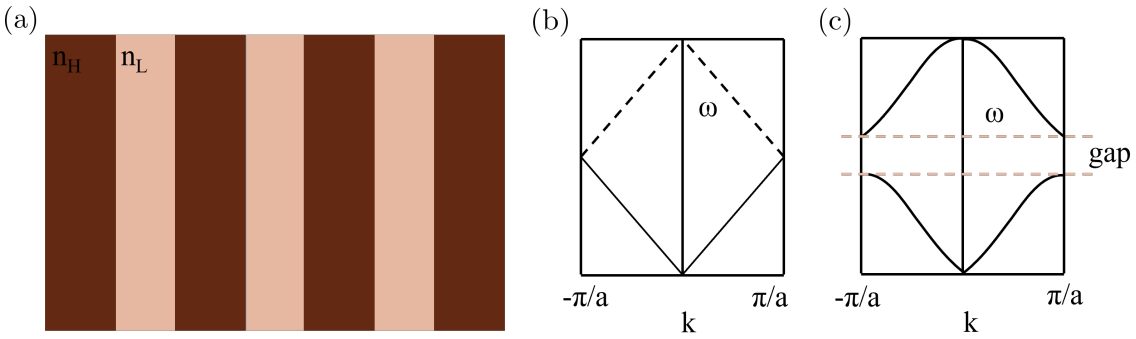

Figure 2.11: Schematic illustration of the formation of a Bragg stop band in a one-dimensional periodic dielectric structure. (a) A distributed Bragg reflector (DBR) consists of alternating high- and low-index dielectric layers, with refractive indices n_H and n_L, respectively. (b) In a homogeneous medium with an assigned period a, the dispersion relation can be folded into the first Brillouin zone without changing the physical modes. (c) When a real periodic dielectric modulation is introduced, the degeneracy of the counter-propagating waves at the Brillouin-zone boundary is lifted, opening a frequency interval in which propagating Bloch modes are not allowed. This interval corresponds to the photonic band gap, or stop band, of the Bragg mirror [76, 77].

A particularly useful DBR design is the quarter-wave stack. In this case, alternating high- and low-index layers, denoted by H and L, are chosen so that

$$n_H d_H = n_L d_L = \frac{\lambda_0}{4}, \tag{2.54}$$

where n_H and n_L are the refractive indices, d_H and d_L are the corresponding physical thicknesses, and λ_0 is the design wavelength [77, 78]. Under this condition, the optical thickness of one bilayer is $\lambda_0/2$, placing λ_0 near the centre of the first stop band, where the reflected waves from successive interfaces interfere constructively in reflection [77, 78].

A Fabry–Pérot cavity is obtained when a spacer layer is placed between two reflecting elements, allowing the optical field to perform multiple round trips inside the spacer region [79]. When the reflecting elements are DBRs, the same structure can also be interpreted as a one-dimensional photonic crystal with a deliberately introduced defect [76, 77]. The spacer interrupts the periodic sequence of the multilayer and can support a localized optical mode whose frequency lies inside the DBR stop band [76, 77]. Since propagation through the surrounding DBRs is forbidden at this frequency, the defect mode remains confined near the spacer and decays evanescently into the Bragg mirrors [76, 77].

The resonance condition is determined by the total phase accumulated during one round trip inside the cavity [78, 79],

$$2k_c d_c + \phi_{r,1} + \phi_{r,2} = 2\pi m, \tag{2.55}$$

where $k_c = 2\pi n_c/\lambda$ is the wavevector in the spacer, d_c is the spacer thickness, $\phi_{r,1}$ and $\phi_{r,2}$ are the reflection phases of the two mirrors, and m is an integer. For DBR mirrors, the reflection phases cannot generally be neglected, because the field penetrates a finite distance into the multilayer before being reflected [77, 78]. When Eq. (2.55) is satisfied, the fields

generated after successive round trips interfere constructively and the intracavity intensity is enhanced, while for wavelengths away from resonance, the round-trip phase is mismatched and the constructive build-up is suppressed [79].

The spectral selectivity of a cavity resonance is quantified by the quality factor [79]

$$Q = \frac{\omega_0}{\Delta\omega}, \tag{2.56}$$

where ω_0 is the resonance angular frequency and $\Delta\omega$ is the full width at half maximum of the resonance. The same quantity can also be interpreted as

$$Q = 2\pi \frac{\text{energy stored in the cavity}}{\text{energy lost per optical cycle}}, \tag{2.57}$$

showing that high-Q resonances correspond to long photon storage times and narrow spectral linewidths [79]. In a DBR cavity, increasing the reflectivity of the Bragg mirrors reduces radiative leakage and therefore increases Q, whereas absorption and scattering introduce additional loss channels that reduce Q [77, 79].

2.5 Critical Coupling

Critical coupling is a resonant absorption condition in which the rate at which energy leaks out of a cavity is matched to the rate at which energy is dissipated inside it [23,24,26]. Under this condition, destructive interference can suppress the outgoing wave from the structure and strongly enhance the absorbed fraction of the incident power [23,25].

Temporal coupled-mode theory (CMT) provides a reduced description of this process by replacing the full resonant structure with a single resonant mode coupled to external radiation channels [25, 26, 80]. In this context, a port denotes an independent input-output channel through which optical power can enter or leave the resonator [25,26]. A structure illuminated from one side is a two-port system if the incident power can leave through both reflection and transmission channels. If a back reflector suppresses transmission, the system becomes effectively one-port, because reflection is the only remaining radiative output channel [23, 26].

The complex amplitude of the resonant mode is denoted by $\alpha(t)$ and is normalized so that $|\alpha|^2$ is the energy stored in the cavity. The incoming, reflected, and transmitted wave amplitudes are denoted by u, y_R, and y_T, respectively, and are normalized so that their squared magnitudes correspond to optical powers [25, 26, 80]. The two basic configurations considered here are shown in Fig. 2.12: a one-port resonator, where a back mirror suppresses transmission, and a two-port resonator, where energy can leave through both reflection and transmission channels [23,26].

2.5.1 One-port resonant absorber

We first consider the one-port geometry of Fig. 2.12(a). The cavity has a resonance frequency ω_0, a radiative decay rate γ_d, and an absorption rate γ_a. The rate γ_d describes leakage of

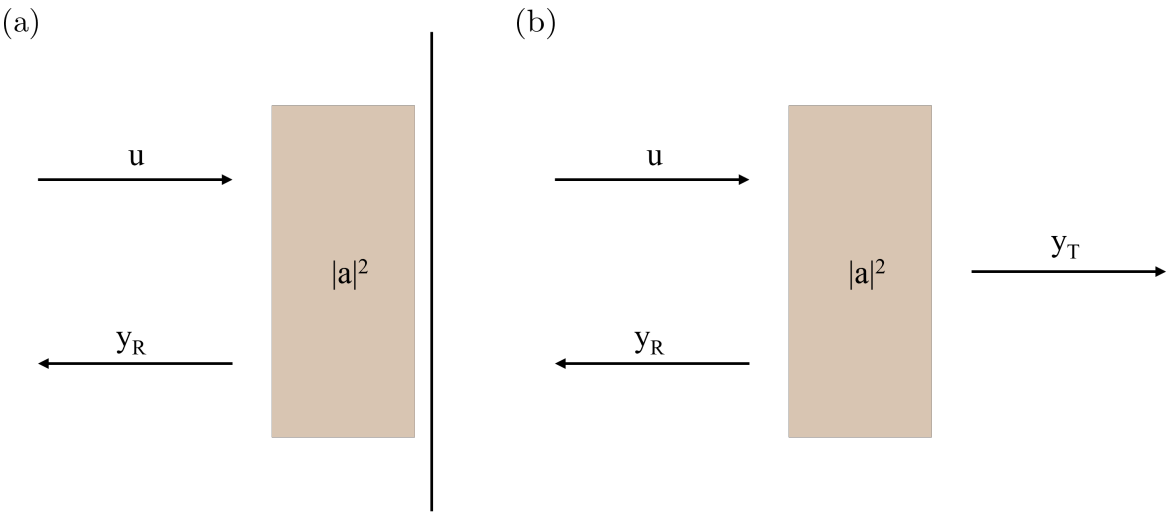

Figure 2.12: Coupled-mode theory representation of a lossy resonant absorber. (a) One-port geometry, where a back mirror suppresses transmission and reflection is the only radiative output channel. (b) Two-port geometry, where the resonator is coupled to both reflection and transmission channels. The resonant mode amplitude is denoted by α, with stored energy $|\alpha|^2$, while u, y_R, and y_T denote the incoming, reflected, and transmitted wave amplitudes, respectively [23, 26].

the resonant mode into the external reflection channel, whereas γ_a describes dissipative loss inside the cavity, including absorption in the active absorbing layer [23, 26].

With the time-dependence convention $e^{i\omega t}$, the one-port resonator is described by the temporal coupled-mode equations [23, 26]

$$\frac{d\alpha}{dt} = i\omega_0\alpha - (\gamma_d + \gamma_a)\,\alpha + \sqrt{2\gamma_d}\,u, \tag{2.58}$$

and

$$y_R = -u + \sqrt{2\gamma_d}\,\alpha. \tag{2.59}$$

The first term on the right-hand side of Eq. (2.58) represents the free oscillation of the resonant mode at ω_0. The second term represents the decay of the mode amplitude due to radiative leakage and material absorption, while the last term represents excitation of the resonant mode by the incident wave.

The factor $\sqrt{2\gamma_d}$ follows from the normalization and energy conservation. If there is no incident wave and no material absorption, the stored energy decays as $|\alpha(t)|^2 \propto e^{-2\gamma_d t}$. Therefore, the power emitted into the single available output channel is $2\gamma_d|\alpha|^2$ and since the emitted field amplitude is proportional to α, the corresponding coupling amplitude is $\sqrt{2\gamma_d}$ [23, 25, 26]. The same coefficient appears in the input term of Eq. (2.58) because, for a reciprocal resonator, coupling from the external channel into the cavity and coupling from the cavity back into the external channel are related by time-reversal symmetry [25, 26].

Equation (2.59) expresses the reflected wave as the coherent sum of two contributions. The term $-u$ is the direct, nonresonant reflection pathway, with the sign fixed by the chosen reference plane and phase convention. The term $\sqrt{2\gamma_d}\alpha$ is the resonant contribution, corresponding to the field that couples into the cavity and is re-emitted into the reflection

channel [23, 25]. Critical coupling is therefore an interference effect between the direct and resonant reflected fields.

For monochromatic excitation at angular frequency ω, the cavity amplitude follows the same harmonic time dependence as the input field. Thus, substituting $\alpha(t) = \alpha e^{i\omega t}$ and $u(t) = ue^{i\omega t}$ into Eq. (2.58) converts the differential equation into an algebraic equation for the steady-state mode amplitude. Solving for the ratio between the stored-mode amplitude and the incident-wave amplitude gives

$$\frac{\alpha}{u} = \frac{\sqrt{2\gamma_d}}{i(\omega - \omega_0) + \gamma_d + \gamma_a}. \tag{2.60}$$

This expression is the Lorentzian response of the resonant mode. The numerator sets how efficiently the incident wave excites the cavity, while the denominator contains both the detuning from resonance, $\omega - \omega_0$, and the total decay rate, $\gamma_d + \gamma_a$ [23, 25, 26].

Substituting Eq. (2.60) into Eq. (2.59) gives the complex reflection coefficient,

$$\frac{y_R}{u} = \frac{\gamma_d - \gamma_a - i(\omega - \omega_0)}{\gamma_d + \gamma_a + i(\omega - \omega_0)}. \tag{2.61}$$

The corresponding reflectance is obtained by taking the squared modulus of this amplitude ratio:

$$R = \left|\frac{y_R}{u}\right|^2 = \frac{(\gamma_d - \gamma_a)^2 + (\omega - \omega_0)^2}{(\gamma_d + \gamma_a)^2 + (\omega - \omega_0)^2}. \tag{2.62}$$

Since the back mirror suppresses transmission, the only possible outgoing power is reflection. Therefore, the absorption is

$$A = 1 - R = \frac{4\gamma_d\gamma_a}{(\gamma_d + \gamma_a)^2 + (\omega - \omega_0)^2}. \tag{2.63}$$

Equation (2.63) shows that complete absorption requires two simultaneous conditions [23, 26]:

$$\omega = \omega_0, \qquad \gamma_d = \gamma_a. \tag{2.64}$$

The first condition means that the incident wave is resonant with the cavity mode, so the detuning term $\omega - \omega_0$ vanishes. The second condition means that the radiative leakage rate is exactly matched to the absorption rate. Under these conditions, the numerator of Eq. (2.62) becomes zero, so the reflected field vanishes.

The regimes away from critical coupling can also be read directly from Eq. (2.63). If $\gamma_d < \gamma_a$, the system is undercoupled: the cavity is too lossy compared with the rate at which energy is fed into it. If $\gamma_d > \gamma_a$, the system is overcoupled: energy leaks back out of the resonator faster than it is dissipated. In both cases, the destructive interference in the reflection channel is incomplete, and the absorption remains below unity [23, 24].

2.5.2 Two-port resonator

The importance of the back mirror becomes clear by comparing the one-port absorber with the two-port geometry of Fig. 2.12(b). In a symmetric two-port cavity, the resonant mode

can radiate through both sides of the structure, so transmission remains an available output channel [23, 26]. For the simplified symmetric case, the CMT equations are [26]

$$\frac{d\alpha}{dt} = i\omega_0\alpha - (\gamma_d + \gamma_a)\,\alpha + \sqrt{\gamma_d}\,u, \tag{2.65}$$

with output relations

$$y_R = -u + \sqrt{\gamma_d}\,\alpha, \tag{2.66}$$

and

$$y_T = \sqrt{\gamma_d}\,\alpha. \tag{2.67}$$

The structure of these equations is the same as in the one-port case, but the coupling amplitude is different. In the symmetric two-port case, the resonant mode radiates into two equivalent output channels. Therefore, the emitted power is split between reflection and transmission, and the coupling amplitude associated with each channel is $\sqrt{\gamma_d}$, rather than $\sqrt{2\gamma_d}$ [26]. The reflected wave again contains a direct term and a resonant re-emission term, while the transmitted wave in this simplified model is produced by resonant emission into the second port.

For monochromatic excitation at angular frequency ω, the same steady-state substitution used above gives

$$\frac{\alpha}{u} = \frac{\sqrt{\gamma_d}}{i(\omega - \omega_0) + \gamma_d + \gamma_a}. \tag{2.68}$$

Inserting this result into the two output relations gives the reflected and transmitted amplitude ratios. Taking their squared moduli gives

$$R = \frac{\gamma_a^2 + (\omega - \omega_0)^2}{(\gamma_d + \gamma_a)^2 + (\omega - \omega_0)^2}, \tag{2.69}$$

and

$$T = \frac{\gamma_d^2}{(\gamma_d + \gamma_a)^2 + (\omega - \omega_0)^2}. \tag{2.70}$$

The absorption is obtained from energy conservation as the part of the incident power that is neither reflected nor transmitted:

$$A = 1 - R - T = \frac{2\gamma_d\gamma_a}{(\gamma_d + \gamma_a)^2 + (\omega - \omega_0)^2}. \tag{2.71}$$

At resonance and for matched rates, $\omega = \omega_0$ and $\gamma_d = \gamma_a$, Eq. (2.71) gives

$$A = \frac{1}{2}. \tag{2.72}$$

Thus, under single-sided illumination, a symmetric two-port resonator cannot absorb more than 50% of the incident power, even when the radiative and absorptive rates are matched [23]. The reason is that the resonator still has two output channels. At the matched condition, only half of the incident power is dissipated, while the remaining power is distributed between the two radiative output channels. By adding a back mirror, the transmission channel is removed, and the system becomes a one-port resonator in which the only remaining outgoing wave can be canceled interferometrically [23].

Chapter 3

Computational Methods

The computational framework used in this work combines three numerical components. First, the optical response of the multilayer cavity is calculated with the transfer matrix method (TMM). This provides the instantaneous reflectance, transmittance, total absorption, and graphene-specific absorption of the structure. Second, the time evolution of the graphene carrier variables, under pulse excitation, is obtained by solving the coupled rate equations for the non-equilibrium carrier density, electronic temperature, and lattice temperature. These equations are integrated in time using a fourth-order Runge–Kutta scheme. Third, the energy-dependent quantities entering the graphene model, such as carrier densities, heat capacities, and optical conductivities, are evaluated numerically using the composite Simpson rule.

3.1 Transfer Matrix Method

The transfer matrix method was used to calculate the optical response of the planar multilayer structures considered in this work. The method is particularly suitable for one-dimensional stratified media, where each layer is laterally uniform and is described by its thickness and complex refractive index [78, 81]. Under these assumptions, the electromagnetic field in each layer can be written as the superposition of a forward- and a backward-propagating plane wave [78].

Figure 3.1 illustrates the two elementary operations used in the TMM formulation. Figure 3.1(a) shows an interface between two media with refractive indices n_1 and n_2. The incident and reflected waves in the first medium are denoted by E_A and E_B, while the forward and backward waves in the second medium are denoted by E_C and E_D, respectively. Figure 3.1(b) shows propagation inside a homogeneous layer of refractive index n_1 and thickness d, where the forward and backward waves acquire opposite propagation phases [78,81].

For normal incidence, taking the z-axis along the propagation direction, the electric field inside layer j is written as

$$E_j(z) = E_j^+ e^{ik_j z} + E_j^- e^{-ik_j z}, \tag{3.1}$$

where E_j^+ and E_j^- are the forward- and backward-propagating field amplitudes, respectively, and

$$k_j = k_0 n_j = \frac{\omega}{c} n_j. \tag{3.2}$$

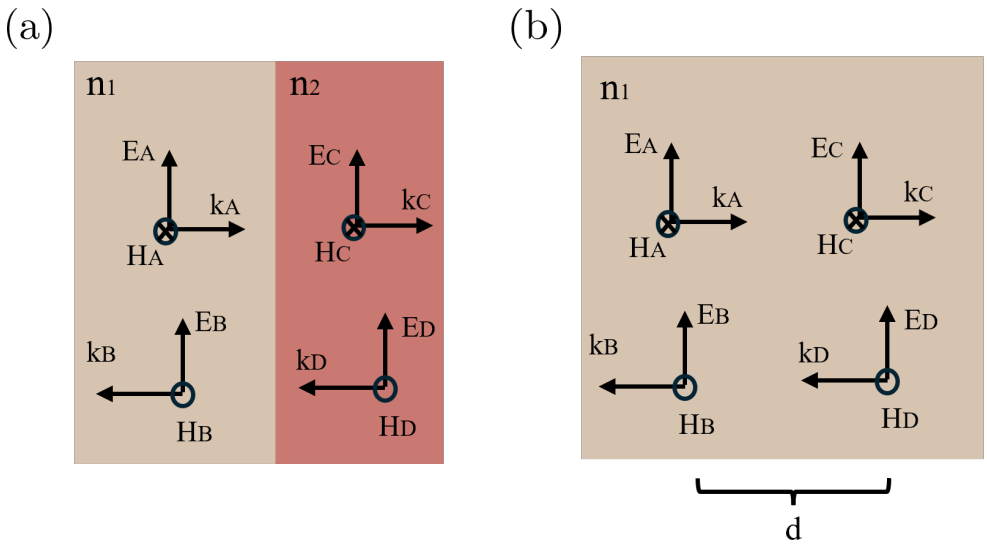

Figure 3.1: Schematic representation of the two elementary steps used in the transfer matrix method. (a) Interface between two media with refractive indices n_1 and n_2, where E_A and E_B are the forward and backward waves in the first medium, while E_C and E_D are the corresponding waves in the second medium. (b) Propagation through a homogeneous layer of refractive index n_1 and thickness d. The symbols $\otimes$ and $\odot$ indicate magnetic-field directions into and out of the page, respectively.

Here k_0 is the vacuum wavenumber, ω is the angular frequency, c is the speed of light in vacuum, and n_j is the refractive index of layer j [44, 78].

The corresponding magnetic field follows from Maxwell's equations. For non-magnetic media and normal incidence, the forward- and backward-propagating waves have opposite magnetic-field signs,

$$H_j(z) = Y_j \left(E_j^+ e^{ik_j z} - E_j^- e^{-ik_j z} \right), \tag{3.3}$$

where

$$Y_j = \frac{n_j}{Z_0} \tag{3.4}$$

is the optical admittance of the layer and $Z_0 = \sqrt{\mu_0/\varepsilon_0}$ is the impedance of free space [44, 78]. The minus sign in the backward-wave term is a direct consequence of the reversed propagation direction, as also indicated by the opposite magnetic-field orientations in Fig. 3.1.

First, consider propagation through a homogeneous layer of thickness d_j, as shown schematically in Fig. 3.1(b). During propagation, the forward wave acquires the phase factor $e^{ik_j d_j}$, while the backward wave acquires the phase factor $e^{-ik_j d_j}$ [78]. Therefore,

$$\begin{pmatrix} E_j^+(z+d_j) \\ E_j^-(z+d_j) \end{pmatrix} = P_j \begin{pmatrix} E_j^+(z) \\ E_j^-(z) \end{pmatrix}, \tag{3.5}$$

with the propagation matrix

$$P_j = \begin{pmatrix} e^{ik_j d_j} & 0 \\ 0 & e^{-ik_j d_j} \end{pmatrix}. \tag{3.6}$$

Next, consider the interface between layer j and layer $j+1$, as shown in Fig. 3.1(a). At an interface without free surface charge or free surface current, the tangential components of the electric and magnetic fields are continuous [44, 78]. For normal incidence, this gives

$$E_j^+ + E_j^- = E_{j+1}^+ + E_{j+1}^-, \tag{3.7}$$

and

$$Y_j \left(E_j^+ - E_j^-\right) = Y_{j+1} \left(E_{j+1}^+ - E_{j+1}^-\right). \tag{3.8}$$

Solving Eqs. (3.7) and (3.8) for the amplitudes in layer $j+1$ gives

$$\begin{pmatrix} E_{j+1}^+ \\ E_{j+1}^- \end{pmatrix} = I_{j,j+1} \begin{pmatrix} E_j^+ \\ E_j^- \end{pmatrix}, \tag{3.9}$$

where the interface matrix is

$$I_{j,j+1} = \frac{1}{2} \begin{pmatrix} 1 + \frac{Y_j}{Y_{j+1}} & 1 - \frac{Y_j}{Y_{j+1}} \\ 1 - \frac{Y_j}{Y_{j+1}} & 1 + \frac{Y_j}{Y_{j+1}} \end{pmatrix}. \tag{3.10}$$

For non-magnetic media, $Y_j/Y_{j+1} = n_j/n_{j+1}$, and therefore

$$I_{j,j+1} = \begin{pmatrix} \frac{n_{j+1}+n_j}{2n_{j+1}} & \frac{n_{j+1}-n_j}{2n_{j+1}} \\ \frac{n_{j+1}-n_j}{2n_{j+1}} & \frac{n_{j+1}+n_j}{2n_{j+1}} \end{pmatrix}. \tag{3.11}$$

For a multilayer stack, the total transfer matrix is obtained by multiplying the interface and propagation matrices in the order in which the wave encounters the layers [78, 81]. For a stack of N internal layers between an incident medium 0 and an exit medium $N+1$, the total matrix can be written as

$$M = I_{N,N+1} P_N I_{N-1,N} \cdots P_1 I_{0,1}. \tag{3.12}$$

With the convention used here,

$$\begin{pmatrix} E_t \\ 0 \end{pmatrix} = M \begin{pmatrix} E_i \\ E_r \end{pmatrix}, \tag{3.13}$$

where E_i, E_r, and E_t are the incident, reflected, and transmitted field amplitudes. The second component on the left-hand side is zero because no wave is assumed to be incident from the output side [78].

From Eq. (3.13), the amplitude reflection coefficient of the full structure is

$$r = \frac{E_r}{E_i} = -\frac{M_{21}}{M_{22}}, \tag{3.14}$$

and the amplitude transmission coefficient is

$$t = \frac{E_t}{E_i} = \frac{\det(M)}{M_{22}}. \tag{3.15}$$

The corresponding reflectance and transmittance are

$$R = |r|^2, \tag{3.16}$$

and

$$T = \frac{n_{N+1}}{n_0}|t|^2. \tag{3.17}$$

The total absorptance of the structure is then calculated from energy conservation as

$$A = 1 - R - T. \tag{3.18}$$

If the absorption of a specific layer is required, it can be obtained from the radiative energy flux through the multilayer structure. More specifically, the absorptance of the j-th layer is calculated from the decrease of the electromagnetic flux across that layer,

$$A_j = S_j^{\text{in}} - S_j^{\text{out}}, \tag{3.19}$$

where S_j^{in} and S_j^{out} are the radiative fluxes at the entrance and exit of layer j, respectively.

To calculate the radiative flux inside an arbitrary layer, both the forward- and backward-propagating waves must be taken into account. Denoting the corresponding field amplitudes in layer j by E_j^+ and E_j^-, the radiative flux can be written as [78, 82]

$$S_j = \Re\left(\frac{n_j}{n_0}\right)\left(|E_j^+|^2 - |E_j^-|^2\right) - 2\Im\left(\frac{n_j}{n_0}\right)\Im\left(E_j^+ E_j^{-*}\right). \tag{3.20}$$

where n_0 refers to the incident medium, while n_j refers to layer j. The first term describes the net contribution of the forward and backward waves, whereas the second term accounts for their interference in absorbing media.

3.2 4^{th} order Runge-Kutta method

The temporal evolution of graphene during pulsed excitation is described by a set of coupled rate equations for the non-equilibrium carrier density n_{ne}, the electronic temperature $T_{e,\text{SLG}}$, and the lattice temperature $T_{l,\text{SLG}}$. These variables are collected in the vector

$$y(t) = \begin{pmatrix} n_{\text{ne}}(t) \\ T_{e,\text{SLG}}(t) \\ T_{l,\text{SLG}}(t) \end{pmatrix}. \tag{3.21}$$

The coupled equations can then be written as the initial-value problem

$$\frac{dy}{dt} = f\left[t, y(t)\right], \quad y(t_0) = y_0 \tag{3.22}$$

The function f contains the generation of photoexcited carriers, carrier thermalization, electronic heating, and cooling through electron–phonon processes and the initial values t_0, y_0

are known. The system is integrated using the classical fourth-order Runge–Kutta method (RK4) [83, 84]. For a time step $h > 0$, the update from t_n to $t_{n+1} = t_n + h$ is

$$y_{n+1} = y_n + h/6\,(k_1 + 2k_2 + 2k_3 + k_4)\,. \tag{3.23}$$

where

$$k_1 = f\,(t_n, y_n)\,, \tag{3.24}$$

$$k_2 = f\left(t_n + \frac{h}{2}, y_n + \frac{h}{2}k_1\right), \tag{3.25}$$

$$k_3 = f\left(t_n + \frac{h}{2}, y_n + \frac{h}{2}k_2\right), \tag{3.26}$$

$$k_4 = f\,(t_n + h, y_n + hk_3)\,, \tag{3.27}$$

The method has a total error of order $O(h^4)$ [83]. It therefore provides a good compromise between accuracy and computational cost for the repeated time-domain simulations required in this work.

3.3 Composite Simpson's rule

Several quantities entering the graphene model are defined through energy integrals. These include, for example, carrier densities, electronic heat capacity, and the optical conductivity. Since these quantities are evaluated repeatedly the numerical integration scheme must be both accurate and computationally efficient.

The composite Simpson rule was used for numerical integration over finite intervals [83]. For an interval $[a, b]$ divided into an even number N of subintervals with $\Delta x = (b - a)/N$, the integral is approximated as

$$\int_a^b f(x)\,dx \simeq \frac{\Delta x}{3}\left[f(x_0) + 4\sum_{j=1}^{N/2} f(x_{2j-1}) + 2\sum_{j=1}^{N/2-1} f(x_{2j}) + f(x_N)\right], \tag{3.28}$$

where $x_j = a + j\Delta x$.

For integrals over infinite or semi-infinite domains, a change of variables was used to map the integration range to a finite interval before applying Simpson's rule. For integrals over the whole real axis,

$$\int_{-\infty}^{+\infty} f(x)\,dx = \int_{-1}^{+1} f\left(\frac{u}{1-u^2}\right)\frac{1+u^2}{(1-u^2)^2}\,du. \tag{3.29}$$

For semi-infinite intervals,

$$\int_a^{+\infty} f(x)\,dx = \int_0^1 f\left(a + \frac{u}{1-u}\right)\frac{du}{(1-u)^2}, \tag{3.30}$$

and

$$\int_{-\infty}^{a} f(x)\,dx = \int_0^1 f\left(a - \frac{1-u}{u}\right)\frac{du}{u^2}. \tag{3.31}$$

Chapter 4

Saturable Absorption Model and Experimental Comparison

4.1 Model formulation

Saturable absorption is the nonlinear optical phenomenon in which the absorption of a material decreases as the incident optical intensity increases. In graphene, absorption saturation can originate from both intraband and interband transitions [13, 16]. Intraband saturation is mainly associated with carrier heating, which modifies the carrier distribution and can reduce the intraband optical conductivity [13]. Interband saturation, by contrast, is primarily governed by band filling: photoexcited nonequilibrium carriers change the occupation of the electronic states involved in the optical transition, thereby inducing Pauli blocking [13, 18]. Carrier heating can also modify the interband response by broadening the Fermi–Dirac distribution and changing the electronic temperature-dependent optical conductivity. For the near-infrared interband excitation regime considered here, the model used in this work therefore focuses on the dominant band-filling contribution, while also accounting for the effect of the electronic carrier temperature on the graphene optical response [16, 18].

The finite linewidth of the interband transition is introduced through the effective optical dephasing time τ_{opt}. As discussed in Sec. 2.2.1, this is implemented in the Kubo conductivity of Eqs. (2.27) and (2.26) by writing the complex frequency as $\Omega = \omega + 2i\Gamma$, with $2\Gamma = \tau_{\text{opt}}^{-1}$. The parameter τ_{opt} phenomenologically accounts for the loss of coherence of the interband excitation due to scattering processes, including electron–phonon, impurity, defect, and other disorder-related scattering mechanisms [52]. Therefore, the interband transition is broadened over a finite energy interval rather than being infinitely sharp, as schematically illustrated in Fig. 4.1. The corresponding energy broadening is $\Delta E = 2\hbar\Gamma = \hbar/\tau_{\text{opt}}$.

For an optical pulse with finite spectral bandwidth, as in femtosecond-duration excitation, an additional broadening should be considered. If τ_p denotes the characteristic pulse duration, this contribution can be represented phenomenologically through an additional frequency width Γ_p, with $2\Gamma_p \simeq \tau_p^{-1}$ [1]. The pulse contribution can therefore be incorporated into an effective linewidth by writing $\Delta E_{\text{eff}} = 2\hbar\Gamma + \hbar\Gamma_p$. Thus, $(\tau_{\text{opt,eff}})^{-1} = 1/\tau_{\text{opt}} + 1/(2\tau_p)$ and $\Gamma_{\text{eff}} = \Gamma + \Gamma_p/2$. For picosecond or longer pulses, the pulse bandwidth is much narrower, and the excitation can be treated as quasi-CW [16].

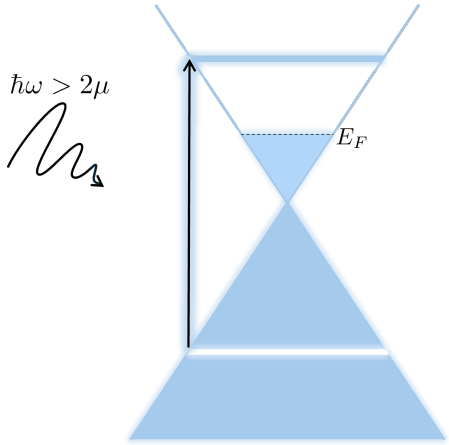

Figure 4.1: Interband excitation in doped graphene for $\hbar\omega > 2|\mu|$. The optical transition occurs between valence- and conduction-band states centered around $-\hbar\omega/2$ and $+\hbar\omega/2$, respectively. The shaded regions represent the finite transition linewidth associated with the effective optical dephasing time τ_{opt}.

The linewidth $2\hbar\Gamma_{\text{eff}}$ determines the energetic spread of the photoexcited carrier population [1,18]. To describe this broadened interband excitation, the photoexcited non-equilibrium electrons in the conduction band are described by a Lorentzian distribution. This Lorentzian profile is motivated by the resonant structure of the interband Kubo conductivity (Eq. (2.27)),

$$L(\varepsilon) = \frac{\hbar^2\Gamma_{\text{eff}}^2}{(\varepsilon - \hbar\omega/2)^2 + \hbar^2\Gamma_{\text{eff}}^2}. \tag{4.1}$$

This function has unit peak value at $\varepsilon = \hbar\omega/2$, a full width at half maximum equal to $2\hbar\Gamma_{\text{eff}}$, and, when the transition energy is much larger than the linewidth, an integral $\int_0^\infty L(\varepsilon)\, d\varepsilon \simeq \pi\hbar\Gamma_{\text{eff}}$.

During optical excitation, the nonequilibrium carrier density, n_{ne}, increases due to photon absorption and decreases due to carrier–carrier scattering, which redistributes the optically injected carriers towards a thermalized hot-carrier distribution [18]. The time evolution of n_{ne} is described phenomenologically by the rate equation [27,41]

$$\frac{dn_{\text{ne}}}{dt} = \frac{\alpha_{\text{inter}} I}{\hbar\omega} - \frac{n_{\text{ne}}}{\tau_{e-e,\text{eff}}}, \tag{4.2}$$

where I is the incident optical intensity, α_{inter} is the instantaneous interband absorbance, and $\tau_{e-e,\text{eff}}$ is the effective lifetime of the optically generated nonequilibrium population. This effective lifetime is introduced to account phenomenologically for the fact that the photoinduced occupation responsible for band filling may be reduced by carrier–carrier relaxation as well as by additional disorder-related processes. It is implemented through a Matthiessen-type addition of rates [85], $1/\tau_{e-e,\text{eff}} = 1/\tau_{e-e} + 1/\tau_{\text{opt}}$, where τ_{e-e} is the electron–electron relaxation time. The first term of Eq. (4.2) represents the generation rate of nonequilibrium carriers: $\alpha_{\text{inter}} I$ is the interband absorbed power per unit area, and division by the photon energy $\hbar\omega$ gives the number of interband absorbed photons per unit area and unit time, while

the second term describes the removal of carriers from the nonequilibrium population. Under steady-state conditions, the total density of photoexcited nonequilibrium carriers is obtained by [27]

$$n_{\text{ne}} = \frac{\alpha_{\text{inter}} I \tau_{e-e,\text{eff}}}{\hbar\omega} = \int_0^\infty \nu(\varepsilon)\, gL(\varepsilon)\, d\varepsilon. \tag{4.3}$$

where $\nu(\varepsilon)$ is the graphene density of states (Eq. (2.7)) and $g = g(I)$ is the height of the Lorentzian, taking values between 0 and 1.

Since in the near-infrared regime the transition energy is much larger than the linewidth, the density of states varies only weakly over the broadened excitation window. For example, at $\lambda = 1550$ nm, $\hbar\omega/2 \simeq 400$ meV, whereas for $\tau_{\text{opt}} \sim 100$ fs to ~ 15 fs the intrinsic linewidth is $2\hbar\Gamma \simeq 6.6$ and $\simeq 44$ meV, respectively, which remains significantly smaller than the transition energy. Therefore, $\nu(\varepsilon) \simeq \nu\left(\hbar\omega/2\right)$, using the graphene density of states introduced in Eq. (2.7), $\nu\left(\hbar\omega/2\right) = \omega/\pi\hbar v_F^2$, together with the Lorentzian integral over energy, Eq. (4.3) becomes

$$n_{\text{ne}} \simeq g \frac{\omega}{2v_F^2 \tau_{\text{opt,eff}}}. \tag{4.4}$$

Equating this expression with Eq. (4.3) gives

$$g = \frac{2\alpha_{\text{inter}} I v_F^2}{\hbar\omega^2} \tau_{e-e,\text{eff}} \tau_{\text{opt,eff}}. \tag{4.5}$$

Thus, the amplitude g of the photoinduced occupation increases with the absorbed intensity, with the carrier–carrier relaxation time, and with the effective optical broadening time.

The intensity dependence of the absorbance is commonly described by the phenomenological saturable-absorption expression [11, 15, 86, 87]

$$\alpha_{\text{inter}}(I) = \frac{\alpha_0}{1 + I/I_s} + \alpha_{\text{ns}}, \tag{4.6}$$

where α_0 is the low-intensity absorbance, I_s is the saturation intensity, and α_{ns} represents a nonsaturable absorbance contribution which is neglected in the present thesis. Substituting Eq. (4.6), with $\alpha_{\text{ns}} = 0$, into Eq. (4.5) gives

$$g(I) = \frac{g_0}{1 + I_s/I}, \tag{4.7}$$

where $g_0 = 2\alpha_0 I_s v_F^2 \tau_{e-e,\text{eff}} \tau_{\text{opt,eff}}/\hbar\omega^2$. Solving for the saturation intensity gives

$$I_s = \frac{g_0 \hbar\omega^2}{2\alpha_0 v_F^2 \tau_{e-e,\text{eff}} \tau_{\text{opt,eff}}}. \tag{4.8}$$

This expression can be rewritten in terms of the carrier density associated with a Fermi level located at the resonant transition energy. Using the graphene density of states, the carrier density up to $E_F = \hbar\omega/2$ is $n\left(\frac{\hbar\omega}{2}\right) = \omega^2/4\pi v_F^2$. Therefore, Eq. (4.8) can be written in the compact form

$$I_s = \gamma n \left(\frac{\hbar\omega}{2}\right), \tag{4.9}$$

where

$$\gamma = \frac{2\pi\hbar g_0}{\alpha_0 \tau_{e-e,\mathrm{eff}} \tau_{\mathrm{opt,eff}}}. \tag{4.10}$$

This form shows that, within the approximations of the model, the saturation intensity scales with the carrier density associated with the resonant interband transition.

The above relations determine the amplitude g of the photoinduced carrier population. The total carrier distribution can therefore be written as the sum of the equilibrium Fermi–Dirac distribution and a nonequilibrium contribution associated with the optically generated electron–hole pairs:

$$f^*_{\mathrm{FD}}(\varepsilon) = f_{\mathrm{FD}}(\varepsilon;\mu,T_e) + g\left[L(\varepsilon) - L(-\varepsilon)\right]. \tag{4.11}$$

The first term is the equilibrium carrier occupation, while the second term describes the

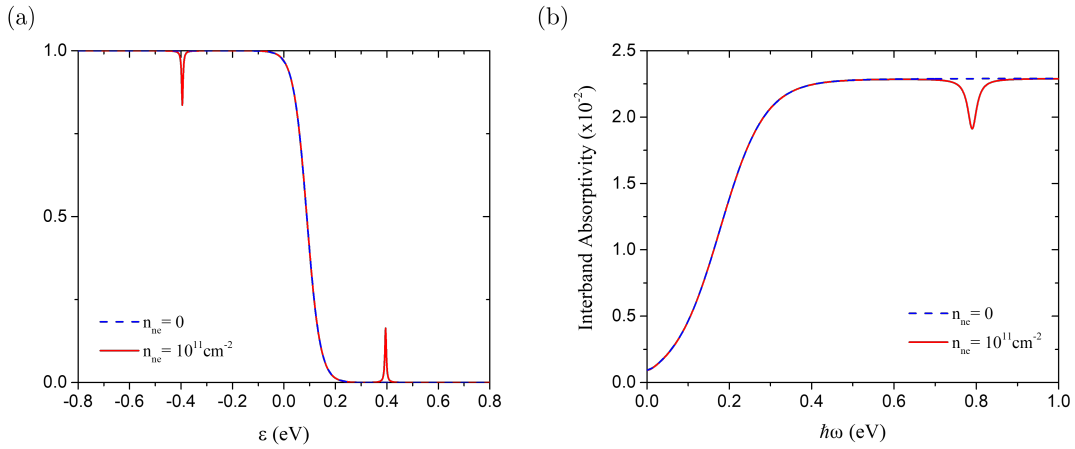

Figure 4.2: (a) Equilibrium Fermi–Dirac distribution (dashed curve) and modified distribution f^*_{FD} (solid curve) and (b) Interband absorbance as a function of photon energy, for $n_{\mathrm{ne}} = 0$ (dashed curve) and 10^{11} cm^{-2} (solid curve). The calculation was performed for $E_F = 0.1$ eV, for a photoexcitation energy $\hbar\omega = 0.8$ eV and $\tau_{\mathrm{opt}} = 100$ fs.

photoinduced modification of the distribution. Specifically, $gL(\varepsilon)$ corresponds to the additional electron occupation around the conduction-band transition energy $+\hbar\omega/2$, whereas $-gL(-\varepsilon)$ describes the corresponding depletion of valence-band states around $-\hbar\omega/2$. This behavior is illustrated in Fig. 4.2(a), where the modified distribution f^*_{FD} is compared with the equilibrium Fermi–Dirac distribution. The photoinduced modification reduces the occupation difference $f^*_{\mathrm{FD}}(-\varepsilon) - f^*_{\mathrm{FD}}(\varepsilon)$ entering the interband optical conductivity of Eq. (2.27). As a result, further interband absorption is suppressed through Pauli blocking, leading to the reduced interband absorbance shown in Fig. 4.2(b). In this way, Eq. (4.11) provides the microscopic link between photoinduced band filling and the macroscopic saturable-absorption response.

To complete the description of the optical response during photoexcitation, carrier heating must also be taken into account. In the presence of the photoinduced nonequilibrium population, the carrier-dependent quantities entering the model, including the optical absorbance,

electrical conductance, and electronic heat capacity, are evaluated using the modified distribution function f^*_{FD} of Eq. (4.11). The absorbance is therefore treated as a function of the chemical potential, the electronic temperature, and the nonequilibrium carrier density, $\alpha \equiv \alpha(\mu, T_e, n_{\mathrm{ne}})$. The dependence on n_{ne} accounts for Pauli blocking due to band filling, whereas the dependence on T_e accounts for the thermal broadening of the carrier distribution.

The temporal evolution of the electronic and lattice temperatures is described using a two-temperature model [22, 27, 88]. The electronic temperature satisfies [27]

$$c_e(\mu, T_e)\frac{dT_e}{dt} = \alpha(\mu, T_e, n_{\mathrm{ne}})I - J_{\mathrm{op}} - J_{\mathrm{sc}}, \tag{4.12}$$

where c_e is the electronic heat capacity (Eq. (2.18)), I is the incident optical intensity, J_{op} is the energy-transfer rate from carriers to optical phonons (Eq. (2.48)), and J_{sc} is the disorder-assisted acoustic-phonon cooling contribution (Eq. (2.50)).

The graphene lattice temperature evolves according to [27, 88]

$$c_l(T_l)\frac{dT_l}{dt} = J_{\mathrm{op}} + J_{\mathrm{sc}} - \Gamma_{\mathrm{SLG-sub}}\left(T_l - T_{\mathrm{sub}}\right), \tag{4.13}$$

where c_l is the lattice heat capacity,$c_l = -1.4 \times 10^{-5} + 1.9 \times 10^{-6} T_l$ J m^{-2} K^{-1} [27, 89], T_{sub} is the substrate temperature. The parameter $\Gamma_{\mathrm{SLG-sub}}$ represents the effective thermal coupling between the graphene lattice and its surrounding environment, usually taking values of ~ 20 MW m^{-2} K^{-1} for Si or SiO_2 substrates [27, 88, 89]. The first two terms of Eq.(4.13) represent the energy received by the lattice from the electronic subsystem, while the last term describes heat dissipation from graphene to the substrate.

Equations (4.2), (4.12), and (4.13) form the dynamical part of the model. During a ps pulse, the instantaneous intensity $I(t)$ generates nonequilibrium carriers, modifies the carrier distribution through $g(t)$, heats the electronic subsystem, and changes the absorbance through $\alpha(\mu, T_e, n_{\mathrm{ne}})$. At the same time, the cooling terms in the electronic- and lattice-temperature equations determine the subsequent relaxation of the system. In this way, the model separates the band-filling contribution from the carrier-heating contribution, while retaining carrier cooling in the transient saturable-absorption dynamics.

However, for femtosecond-pulse excitation, the absorbed power entering the electronic heat bath is treated more explicitly. Since the interband excitation first creates a nonequilibrium electron–hole population, not all absorbed interband energy is assumed to thermalize instantaneously into the hot Fermi–Dirac carrier bath. The electronic-temperature rate equation is therefore written in the form

$$c_e(\mu, T_e)\frac{dT_e}{dt} = \alpha_{\mathrm{intra}} I(t) + \frac{n_{\mathrm{ne}}\hbar\omega}{\tau_{e-e,\mathrm{eff}}} - J_{\mathrm{op}} - J_{\mathrm{sc}}. \tag{4.14}$$

The additional term represents the energy transferred to the thermalized hot-carrier distribution as the optically generated nonequilibrium carriers relax towards a Fermi–Dirac distribution over the characteristic time $\tau_{e-e,\mathrm{eff}}$.

The transient response is obtained by solving the carrier and thermal dynamics self-consistently with the instantaneous optical response of the structure. At each time step of the incident pulse, the optical response of the system is calculated using the transfer matrix

method, with the graphene optical properties updated from the instantaneous carrier distribution. The total graphene absorbance, α, is then separated into interband and intraband contributions according to the relative contribution of the real parts of the corresponding optical conductivities, since optical loss is governed by the real part of the optical conductivity or, equivalently, by $\Im\{\epsilon_{SLG}\}$ [27, 90]

$$\alpha_{\text{inter}} = \alpha \frac{\text{Re}\left\{\sigma_{\text{inter}}^{(1)}\right\}}{\text{Re}\left\{\sigma_{\text{intra}}^{(1)} + \sigma_{\text{inter}}^{(1)}\right\}}. \tag{4.15}$$

The intraband contribution is obtained in the same way. The coupled rate equations for n_{ne}, T_e, and T_l (Eqs. (4.2), (4.12) or (4.14) and (4.13) respectively) are integrated in time using a fourth-order Runge–Kutta method.

4.2 Comparison of Reported Graphene Saturation Intensities

Graphene saturable absorption has been investigated using a wide range of sample configurations and experimental techniques [8,9,17,86,91,92]. However, the reported saturation intensities, I_s, span several orders of magnitude [14, 93–96]. Part of this dispersion arises from differences in excitation wavelength, pulse duration, layer number, saturable absorbance, sample morphology, carrier-relaxation dynamics, and optical environment [16,92,96]. Consequently, the reported I_s values are not always directly comparable. The purpose of this section is therefore to express the available literature data on a common, model-guided basis and to examine whether systematic trends occur after normalization. The analysis follows the physical picture detailed in Section 4.1.

According to Eq. (4.8), the frequency dependence of the saturation intensity is approximately quadratic, $I_s \propto \omega^2$. Consequently, in order to compare measurements performed at different wavelengths, each reported saturation intensity was first referred to 1550 nm, a standard reference wavelength in fiber-optic systems and optical communications [97,98]. A second normalization was then introduced to account for the saturable part of the absorbance and for the effective number of graphene layers participating in the optical interaction

$$I_{\text{norm}} = I_s \left(\frac{\lambda}{1550\ \text{nm}}\right)^2 \frac{a_0}{N_{\text{eff}}}, \tag{4.16}$$

where a_0 denotes the saturable part of the absorption and N_{eff} is the effective number of graphene layers participating in the optical interaction. The factor N_{eff} is introduced to account for the approximately linear scaling of graphene absorbance with the number of layers [8,9]. For continuous chemical vapor deposition (CVD)-transferred, epitaxial, or mechanically exfoliated graphene films, N_{eff} can be associated with a physical number of graphene layers [8,9,93,95,99,100]. In contrast, in flake-based polymer composites, liquid dispersions, and other effective graphene media, N_{eff} is only an effective optical quantity and does not correspond to a well-defined stack of continuous graphene monolayers [14,92,96,101,102].

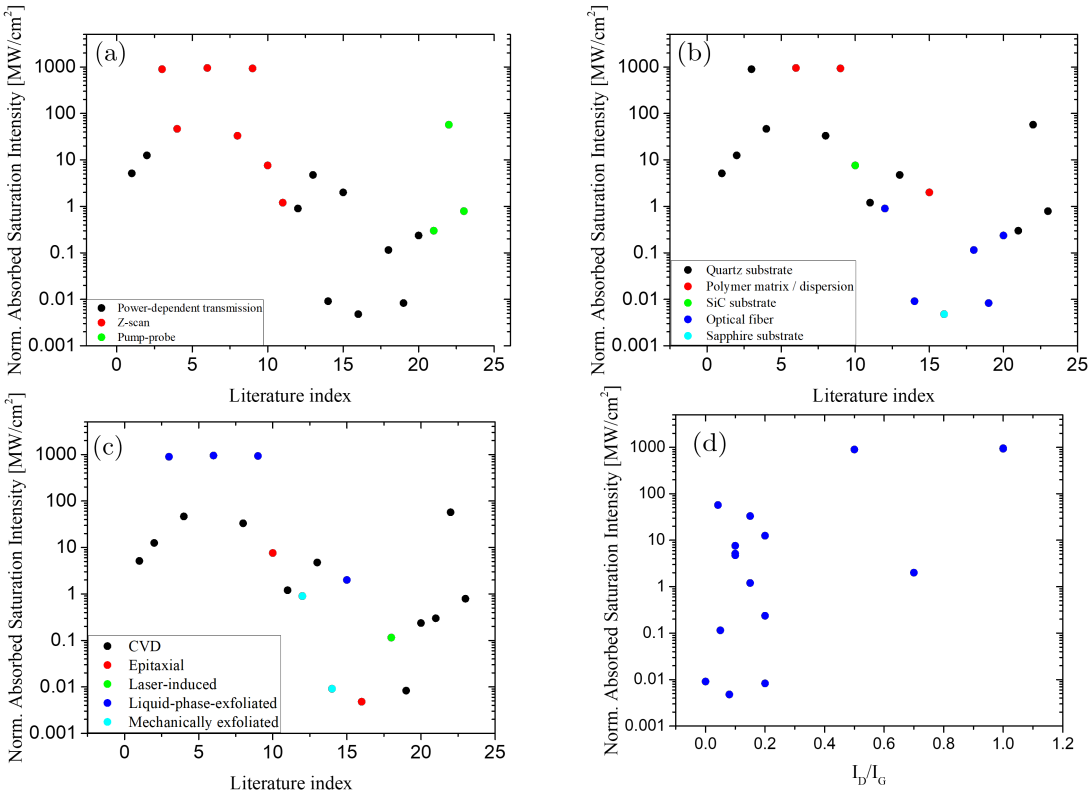

Figure 4.3: Normalized absorbance-weighted saturation intensity I_{norm} extracted from the literature and classified according to: (a) experimental method, (b) substrate or host medium, (c) graphene fabrication route, and (d) Raman disorder ratio I_D/I_G, where available.

The literature data used in the comparison are listed in Table 4.1 and grouped according to experimental method, substrate or host medium, graphene fabrication route, and Raman disorder ratio I_D/I_G.

The reported saturation parameters were also extracted using different fitting expressions. Most studies employ the rational saturable-absorption model given by Eq. (4.6), whereas Lu et al. used the exponential bleaching law

$$a(I) = a_0 e^{-I/I_s} + a_{\text{ns}}, \tag{4.17}$$

to describe the power-dependent transmission [17]. Tan et al. used the related, but mathematically distinct, transmission model

$$T(I) = A e^{\left[-\frac{B}{1+I/I_s}\right]}, \tag{4.18}$$

while other studies included an additional two-photon-absorption or optical-limiting term, typically proportional to βI, to reproduce the reduction in transmission at high intensities [96, 103, 107]. These models do not assign exactly the same numerical meaning to I_s, the saturable contribution of the rational model decreases asymptotically as I^{-1}, whereas the exponential model approaches its high-intensity limit more rapidly. When a clear saturation plateau is

Table 4.1: Literature data used for the normalization of graphene saturation intensity.

Index	Reference	Fabrication	Experimental method	Substrate	λ (nm)	Pulse (ps)	N_{eff}	I_D/I_G	I_s [MW/cm^2]	a_0	I_{norm} [MW/cm^2]
1	[17]	CVD	Power-dependent transmission	Quartz substrate	800	0.100	3	0.100	7.91×10^3	0.00731	5.13×10^0
2	[17]	CVD	Power-dependent transmission	Quartz substrate	800	0.100	1	0.200	2.77×10^3	0.01690	1.25×10^1
3	[92]	Liquid-phase-exfoliated	Z-scan	Quartz substrate	1030	0.340	5	0.500	8.51×10^4	0.11900	8.94×10^2
4	[96] (CVD-GR)	CVD	Z-scan	Quartz substrate	1030	0.300	1	–	6.20×10^3	0.01700	4.65×10^1
5	[92] (G/NMP)	Liquid-phase-exfoliated	Z-scan	Polymer matrix / dispersion	1030	0.340	5	1.000	6.71×10^4	0.16100	9.54×10^2
6	[103]	CVD	Z-scan	Quartz substrate	1086	0.125	3	0.150	3.00×10^3	0.06700	3.29×10^1
7	[92] (G/PVA)	Liquid-phase-exfoliated	Z-scan	Polymer matrix / dispersion	1030	0.340	5	1.000	5.99×10^4	0.17600	9.31×10^2
8	[91]	Epitaxial	Z-scan	SiC substrate	800	0.200	1	0.100	4.00×10^3	0.00710	7.57×10^0
9	[95]	CVD	Z-scan	Quartz substrate	1550	3.800	3	0.150	7.40×10^1	0.04850	1.20×10^0
10	[9]	Mechanically exfoliated	Power-dependent transmission	Optical fiber	1550	0.500	8	–	9.00×10^1	0.08000	9.00×10^{-1}
11	[104]	CVD	Power-dependent transmission	Quartz substrate	800	0.060	1	0.100	9.92×10^2	0.01800	4.76×10^0
12	[93]	Mechanically exfoliated	Power-dependent transmission	Optical fiber	1550	0.400	1	0.000	6.20×10^{-1}	0.01470	9.11×10^{-3}
13	[14]	Liquid-phase-exfoliated	Power-dependent transmission	Polymer matrix / dispersion	1558	0.450	1	0.700	1.00×10^2	0.02000	2.02×10^0
14	[99]	Epitaxial	Power-dependent transmission	Sapphire substrate	1040	0.500	1	0.080	5.10×10^{-1}	0.02100	4.82×10^{-3}
15	[94]	Laser-induced	Power-dependent transmission	Optical fiber	1562	1.500	6	0.050	9.70×10^0	0.07000	1.15×10^{-1}
16	[86]	CVD	Power-dependent transmission	Optical fiber	1550	1.000	1	0.200	5.30×10^{-1}	0.01570	8.32×10^{-3}
17	[8]	CVD	Power-dependent transmission	Optical fiber	1550	1.000	3	0.200	7.10×10^{-1}	0.04480	1.06×10^{-2}
18	[105]	CVD	Pump-probe	Quartz substrate	1250	0.160	1	–	8.52×10^1	0.00540	2.99×10^{-1}
19	[100]	CVD	Pump-probe	Quartz substrate	800	0.100	1	0.042	1.00×10^4	0.02150	5.73×10^1
20	[106]	CVD	Pump-probe	Quartz substrate	1040	0.200	1	–	2.35×10^2	0.00750	7.93×10^{-1}

The last column reports the normalized absorbance-weighted comparison quantity I_{norm}, calculated from Eq. (4.16).

resolved, the choice of fitting law generally changes the extracted scale only by a factor of order unity. If only the initial nonlinear increase in transmission is measured, however, I_s becomes strongly correlated with the modulation depth and may be poorly constrained, while the inclusion of competing nonlinear absorption introduces additional parameter correlations.

The experimental methods considered in Fig. 4.3(a) include power-dependent or balanced transmission, open-aperture Z-scan, and pump–probe spectroscopy. The first two probe the intensity- or fluence-dependent nonlinear transmission: in Z-scan, the incident intensity is varied by translating the sample through the beam focus [108], whereas in power-dependent transmission the sample remains fixed and the incident power is varied [8]. Pump–probe spectroscopy instead records the pump-induced change in probe transmission as a function of the relative delay between the two pulses. At complete spatial overlap and zero delay, fluence-dependent pump–probe measurements have been shown to converge with single-pulse saturation measurements [109]. When the normalized values are grouped according to experimental method, no clearly separated clusters emerge. Several open-aperture Z-scan values remain in the upper part of the distribution, although many correspond to heterogeneous effective media, for which scattering and host contributions may affect the measured response [92, 96]. Power-dependent transmission measurements span almost the entire normalized range, from below 10^{-2} to above $10\ \mathrm{MW/cm^2}$, while the fewer pump–probe entries also remain broadly distributed. The residual spread therefore cannot be attributed to a systematic difference between Z-scan and power-dependent transmission alone, consistent with the same-sample study of Miao et al., who observed qualitatively similar saturable-absorption behavior using open-aperture Z-scan and balanced transmission [110].

Panel 4.3(b) groups the normalized values according to the substrate or host medium, including continuous graphene films on quartz, sapphire, or SiC, fiber-integrated absorbers, and effective media such as polymer composites and liquid dispersions. Quartz-supported samples extend over several orders of magnitude despite sharing the same nominal substrate, whereas polymer composites and liquid dispersions include several of the highest normalized values. In these effective media, the measured response also depends on material concentration, aggregation, host properties, and optical path length [92, 96, 102]. Several fiber-integrated absorbers appear near the lower end of the distribution, however, this should not be interpreted as an intrinsic effect of silica, since the inferred intensity and measured transmission may also depend on the specific optical configuration, coupling conditions, and effective light–graphene interaction [10, 111].

Panel 4.3(c) classifies the data according to fabrication route, including CVD-transferred, direct-grown or epitaxial, mechanically exfoliated, liquid-phase-exfoliated, and laser-induced graphene. No fabrication category forms a distinct cluster after normalization, CVD-transferred samples alone span several orders of magnitude. This shows that nominally similar continuous films can exhibit substantially different saturation parameters because of variations in layer number, doping, transfer residues, grain structure, substrate interaction, and fitting conditions. Liquid-phase-exfoliated and other flake-based samples include several of the highest values, but their normalization by N_{eff} is less direct, since the number of layers within an individual flake does not generally correspond to the number of graphene sheets sampled along the optical path.

Panel 4.3(d) shows no monotonic relation between I_{norm} and the Raman ratio I_D/I_G. Ra-

man spectroscopy is widely used as a nondestructive probe of graphene structural quality, with I_D/I_G commonly employed as an indicator of disorder-related scattering [28–30]. The G band originates from the in-plane bond-stretching mode, whereas the D band is defect-activated through intervalley double-resonance scattering [28, 30]. Comparing I_D/I_G with I_{norm} therefore provides a qualitative test of whether the normalized saturation intensity is related to Raman-inferred disorder. No clear trend is observed, suggesting that Raman-inferred disorder is not the dominant parameter controlling I_{norm} across the compiled studies.

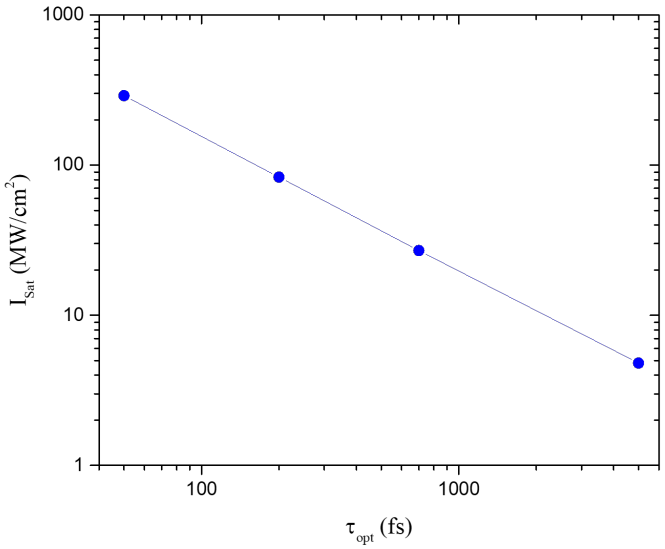

Figure 4.4: Model-calculated saturation intensity I_s as a function of the optical relaxation time τ_{opt} for a quartz/graphene/quartz structure with $E_F = 0.2$ eV, excited by a 1 ps pulse at $\lambda = 1550$ nm. The saturation intensity decreases by nearly two orders of magnitude over the considered range of τ_{opt}.

To illustrate the sensitivity of the saturation response to the optical dephasing time, Fig. 4.4 shows the calculated dependence of I_{sat} on the optical relaxation time τ_{opt}. Over the full range considered, I_{sat} decreases by nearly two orders of magnitude. A similar qualitative trend was reported by Marini et al. [16]. At $\lambda \simeq 1550$ nm, their model predicts a decrease from the order of 10^2 MW/cm^2 at $\tau = 50$ fs to below 1 MW/cm^2 at $\tau \simeq 700$ fs, whereas the present model yields a weaker decrease, from approximately 290 to 27 MW/cm^2 over the same interval. This quantitative difference may partly arise from the distinct treatment of carrier relaxation: Marini et al. assume $T = 0$ K and use a single effective relaxation time, while the present model includes carrier thermalization and the evolution of a hot Fermi–Dirac distribution.

Overall, the persistence of the wide spread after normalization indicates that the reported saturation intensities are governed by several coupled physical and methodological factors that are not captured by wavelength, saturable absorbance, and layer-number scaling alone. Differences between reasonable fitting laws or spatial and temporal pulse conventions can shift the extracted I_s, but are not sufficient by themselves to explain the full multi-order spread. Much larger discrepancies can arise when average and peak intensities are not con-

sistently distinguished, or when intensity and fluence are compared without accounting for pulse duration. The remaining dispersion could therefore be understood as the combined result of genuine sample-to-sample variation and the broad diversity of experimental conditions and reported observables.

4.3 Comparison with Experiment

The saturable-absorption model developed in Section 4.1 is now compared with experimental measurements performed on an electrically gated single-layer-graphene free-space device. The purpose of this comparison is not only to reproduce the measured nonlinear transmission curves, but also to examine whether the model captures the gate-dependent transition between the low-power Pauli-blocked regime, saturable absorption, and reverse saturable absorption (RSA).

As discussed in the previous sections, when $2|\mu| < \hbar\omega$, interband transitions at the excitation photon energy are allowed. Optical absorption then generates non-equilibrium electron and hole populations around $\pm\hbar\omega/2$. At sufficiently high incident intensity, the occupation of these optically active states reduces the probability of further interband transitions through Pauli blocking. As a result, the graphene absorbance decreases and the transmission increases, giving rise to saturable absorption. In contrast, when $2|\mu| \gtrsim \hbar\omega$, the low-power interband absorption is already suppressed by Pauli blocking and the linear absorbance of graphene is small. However, the residual absorption, due to thermal broadening of the carrier distribution, can still heat the electronic system during the incident pulse. The resulting increase in electronic temperature broadens more the Fermi–Dirac distribution and partially restores the availability of optically active interband transitions near the photon energy. This thermal broadening can therefore increase the absorbance with increasing incident intensity. When this heating-induced increase in absorption dominates over the bleaching caused by non-equilibrium band filling, the device exhibits RSA [112].

All experimental measurements and figures presented in this section were provided by the collaborators at the Cambridge Graphene Centre, University of Cambridge. The contribution of the present work is the numerical analysis and comparison of the experimental results with the saturable-absorption model of Section 4.1.

4.3.1 Experimental device and linear characterization

The experimental device, shown in Fig. 4.5(a), consists of a gate-tuned CVD single-layer graphene sample in a free-space transmission geometry. The device configuration and measurements follow the same general approach as previous ionic-liquid gated SLG optical devices reported by the same group [113]. Figure 4.5(b) illustrates the device layout, the optical stack, and the gating geometry. The active region consists of CVD single-layer graphene transferred onto a quartz substrate, covered by an ionic-liquid layer and a top quartz cover. Au source–drain contacts define the electrically accessible graphene channel, while a separate Au gate electrode is used together with the ionic liquid to electrostatically tune the carrier density of graphene. The ionic liquid covers both the graphene channel and the gate elec-

trode, forming a continuous electrolyte layer between them. This enables the graphene Fermi level to be tuned over a wide range, as explained in Subsection 2.1.2, thereby modifying both the low-power optical absorption and the nonlinear transmission response of the device. The optical beam is transmitted through the central gated graphene region, away from the metal contacts. Therefore, the measured transmission is dominated by the optical response of the gated SLG channel and its surrounding dielectric environment.

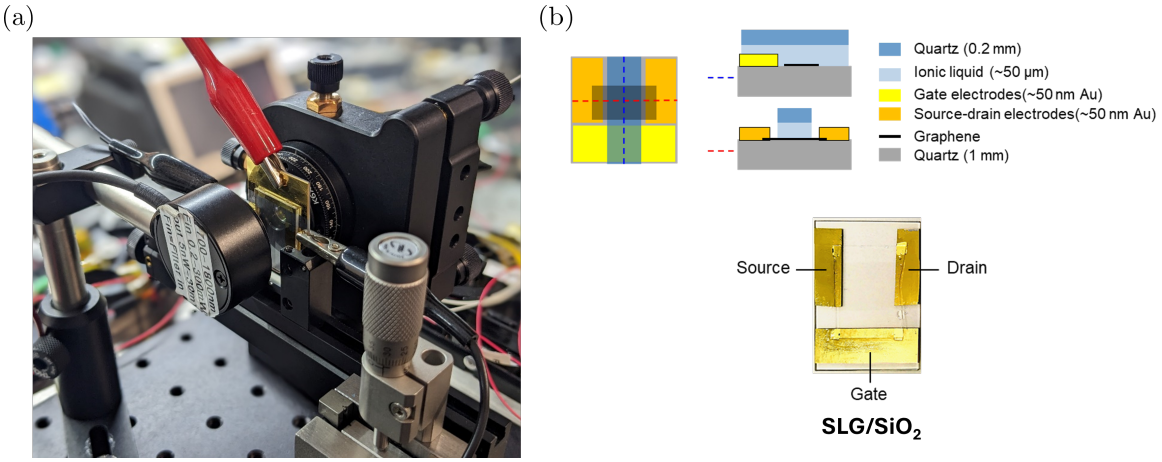

Figure 4.5: Experimental electrically gated SLG free-space device used for the nonlinear transmission measurements. (a) photograph of the sample mounted in the optical setup. (b) Schematic top view, cross-sectional views along the indicated directions, and optical image of the fabricated device. The active optical stack consists of CVD single-layer graphene transferred onto a 1 mm-thick quartz substrate, an ionic-liquid layer of thickness 50 μm, and a top quartz cover 0.2 mm. Au source–drain contacts and an Au gate electrode, each with thickness 50 nm, are used for electrical access and electrostatic gating. Experimental figure provided by the Cambridge Graphene Centre.

Figure 4.6 presents the low-power optical transmission at $\lambda = 1566$ nm, together with the electrical transfer characteristics of the gated SLG device. Figure 4.6(a) shows the raw transmission measured for both a reference device without SLG and the complete SLG-containing device. The transmission of the reference device remains nearly independent of gate voltage, confirming that the passive optical stack does not introduce appreciable gate-dependent modulation. In Fig. 4.6(b), the transmission of the SLG device is normalized by that of the reference device, such that the transmission of the passive stack corresponds to 100%.

The electrical transfer curve shown in Fig. 4.6(b) was measured by applying a small source–drain bias, $V_{SD} = 50$ mV, between the metallic contacts and recording the gate-dependent resistance of the graphene channel. The resistance reaches a pronounced maximum at the charge-neutrality point, corresponding to the minimum-conductivity region of graphene [32]. Since a positive gate voltage is required to reach this point, the graphene is p-doped at $V_g = 0$ [114]. The displacement between the forward and backward voltage sweeps reveals pronounced hysteresis, which is commonly observed in electrolyte- and ionic-liquid-gated devices and is mainly associated with the finite ionic response time and the reorganization of ions within the electric double layer at the graphene–ionic-liquid interface [115,116]. As the gate voltage moves away from the charge-neutrality point, the channel

resistance decreases because of the increasing electron or hole density. At the same time, the optical transmission increases as interband absorption is progressively suppressed by Pauli blocking.

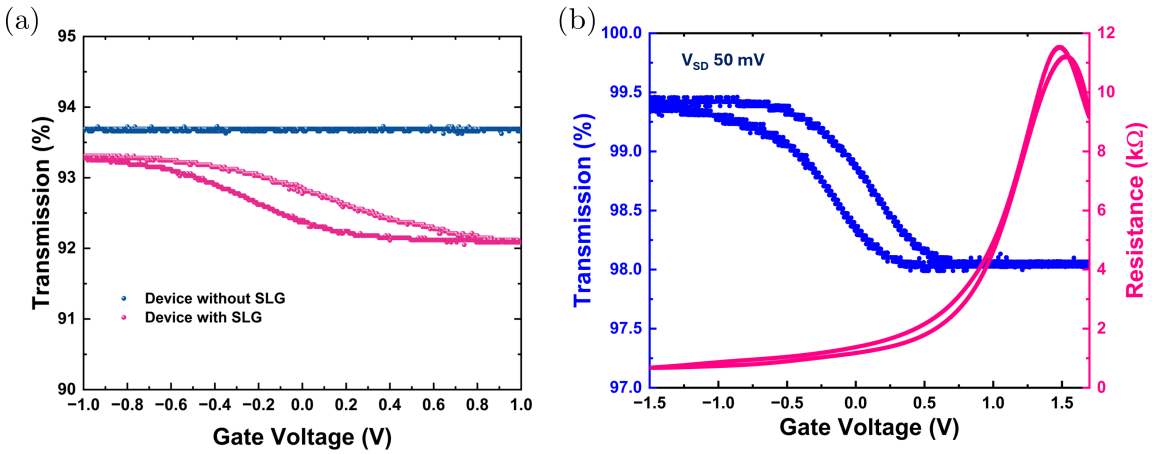

Figure 4.6: Linear transmission and electrical transfer measurements of the gated SLG free-space device. (a) Transmission as a function of gate voltage for the reference device without SLG and for the device with SLG. (b) Normalized gate-dependent transmission of the SLG device, obtained by using the reference device without SLG as the 100% transmission level (blue), together with the electrical resistance measured at $V_{SD} = 50$ mV (pink). Experimental figure provided by the Cambridge Graphene Centre.

4.3.2 Raman-based Fermi-level calibration

Raman spectroscopy was used to calibrate the gate-voltage dependence of the graphene Fermi level. The Raman spectra shown in Fig. 4.7(a) were acquired from the CVD-grown SLG transferred onto quartz at gate voltages corresponding to those used in the nonlinear transmission measurements. The G peak originates from first-order Raman scattering by the in-plane E_{2g} optical phonon at the Brillouin-zone centre Γ [28, 30, 117]. Its position and linewidth are sensitive to charge doping through the doping-dependent renormalization of the phonon energy and lifetime, and are therefore widely used to probe the electronic state of graphene [30, 114, 118]. However, the G peak can also be affected by strain and disorder, so its interpretation is usually combined with the behaviour of the 2D peak and the intensity/area ratios of the Raman bands [30, 117]. The 2D peak is a second-order, two-phonon Raman feature associated with a double-resonance process involving phonons near the K point [28, 30, 117]. Unlike the defect-activated D peak, the 2D peak does not require defects to be observed, because the two-phonon process satisfies momentum conservation without defect scattering [28, 30]. Its lineshape is particularly important for identifying single-layer graphene because in SLG, it is well described by a single Lorentzian component [28].

At the most strongly doped states, the G peak is located at 1594 ± 1 cm^{-1}, with FWHM(G) $= 14 \pm 1$ cm^{-1}, while the 2D peak is located at 2693 ± 1 cm^{-1}. Near the charge-neutrality re-

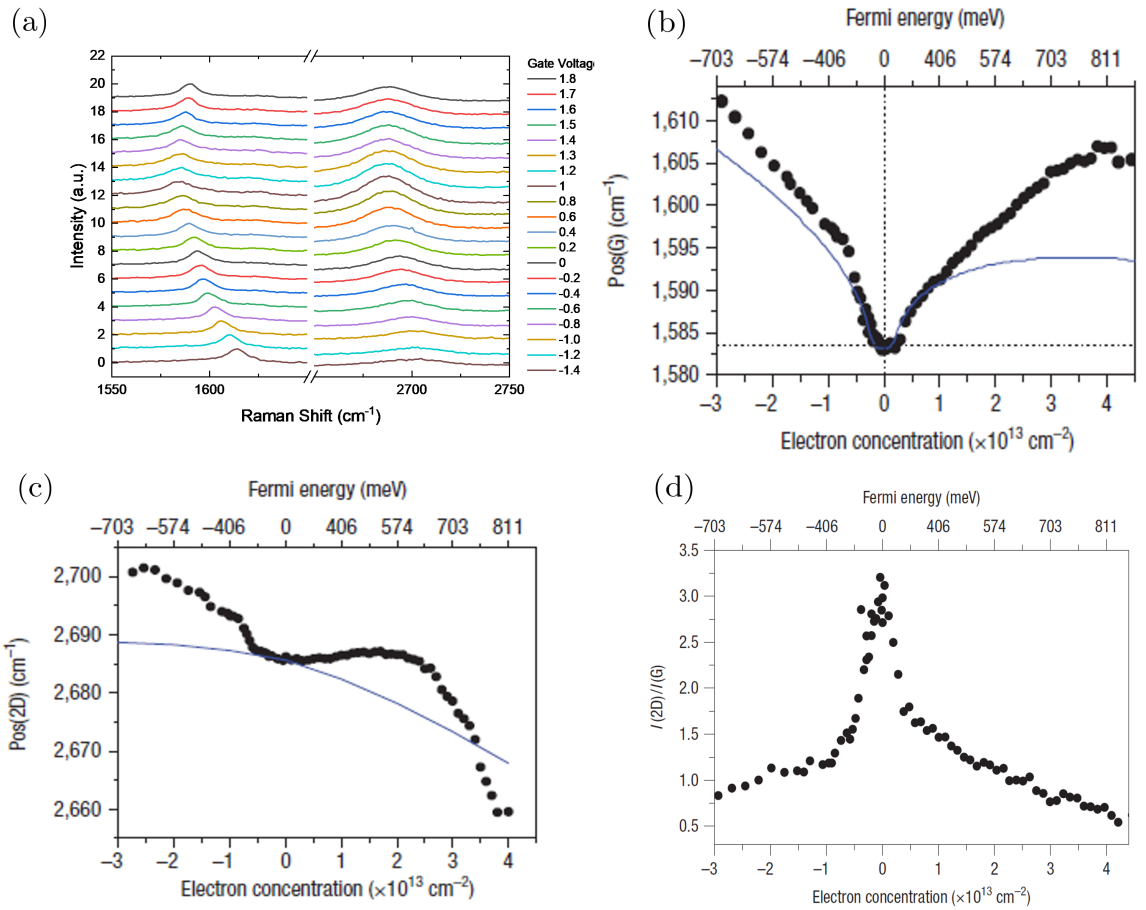

Figure 4.7: (a) Raman spectra of CVD-grown SLG transferred onto quartz at different gate voltages. Experimental data provided by the Cambridge Graphene Centre. (b)–(d) Doping-dependent calibration curves for Pos(G), Pos(2D), and $I(2D)/I(G)$, respectively, adapted from Das et al. [114].

gion, the G peak shifts to 1585 ± 1 cm^{-1} and broadens to FWHM(G) $= 21 \pm 1$ cm^{-1}, while the 2D peak shifts to 2687 ± 1 cm^{-1}. This evolution is consistent with the established Raman response of gated graphene. Increasing the carrier density stiffens and narrows the G mode, whereas near charge neutrality the G peak softens and broadens because electron–hole-pair generation by phonon decay is no longer suppressed by Pauli blocking [114, 118]. The measured $I(2D)/I(G)$ ratio reaches its largest value near the charge-neutrality region and decreases at large $|V_G - V_{CNP}|$. This behaviour is associated with the doping-induced increase in the electronic scattering rate of the photoexcited carriers involved in the resonant Raman process, which reduces the probability of completing the multistep process responsible for the 2D peak [118].

The carrier-density magnitude was estimated by comparing the fitted Raman parameters with the doping-dependent calibration reported by Das et al. for electrochemically top-gated graphene [114]. In that work, the G-peak position, the 2D-peak position, and the intensity ratio $I(2D)/I(G)$ were measured as functions of gate-induced carrier density, providing empirical calibration curves for the corresponding Raman observables.

For the present CVD SLG/quartz sample, the experimentally extracted values of Pos(G),

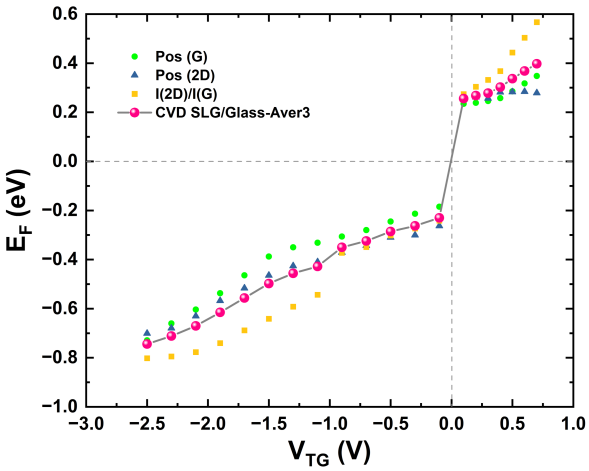

Figure 4.8: Raman-derived Fermi energy as a function of $V_{\mathrm{TG}} = V_{\mathrm{G}} - V_{\mathrm{CNP}}$. The green, blue, and yellow points denote the estimates obtained from Pos(G), Pos(2D), and $I(2D)/I(G)$, respectively, while the pink points show their arithmetic mean. Experimental analysis and figure provided by the Cambridge Graphene Centre.

Pos(2D), and $I(2D)/I(G)$ were mapped separately onto the calibration curves shown in Fig. 4.7(b)–(d), yielding three estimates of the carrier-density magnitude. Because these Raman observables are primarily sensitive to the magnitude of the carrier density, the carrier type was assigned using the position of the applied gate voltage relative to the electrically determined charge-neutrality point. Accordingly, $V_{\mathrm{TG}} < 0$ was assigned to hole doping and $V_{\mathrm{TG}} > 0$ to electron doping, where $V_{\mathrm{TG}} = V_{\mathrm{G}} - V_{\mathrm{CNP}}$.

Each carrier-density estimate was converted into a signed Fermi energy using Eq. (2.11) of Subsection 2.1.2. The resulting gate-dependent estimates of E_F are shown in Fig. 4.8. The final Raman-derived Fermi energy at each gate voltage was taken as the arithmetic mean of the values obtained from Pos(G), Pos(2D), and $I(2D)/I(G)$.

4.3.3 Experimental nonlinear transmission curves

The nonlinear transmission of the gated CVD SLG device was measured using a fibre-based setup operating at 1566 nm, with a pulse duration of 120 fs. The incident beam was divided into sample and reference arms. The sample arm illuminated the device, and the transmitted pulse energy was recorded by a detector, while the reference arm monitored the incident pulse energy.

For each applied gate voltage, corresponding to a Raman-derived Fermi energy E_F, the incident pulse energy was varied and the resulting transmission was determined. Figure 4.9 shows the measured transmission as a function of incident fluence for the different Fermi-energy states.

At the most negative Fermi energies, the low-fluence transmission is high, consistent with the suppression of interband absorption by Pauli blocking. As the incident fluence increases, the transmission decreases, revealing reverse saturable absorption. This behaviour is most pronounced for the highly hole-doped states, with E_F between approximately -0.74 and

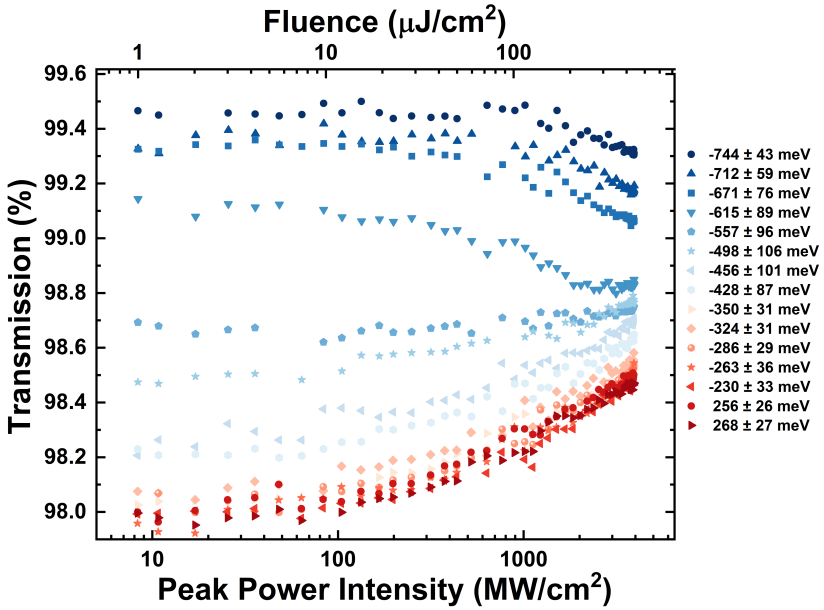

Figure 4.9: Experimental nonlinear-transmission curves of the gated CVD SLG device measured at 1566 nm with a pulse duration of 120 fs. The transmission is plotted as a function of incident fluence and peak power intensity for different Raman-derived Fermi energies. Experimental data and graph provided by the Cambridge Graphene Centre.

-0.62 eV.

At intermediate Fermi energies, the fluence dependence becomes weaker and, in some cases, non-monotonic, indicating a crossover between the competing effects of carrier heating and non-equilibrium band filling. Closer to the charge-neutrality region, as well as for the measured electron-doped states, the transmission increases with incident intensity. This behaviour corresponds to saturable absorption and is attributed to the progressive bleaching of interband transitions through photoinduced Pauli blocking. The measurements therefore show that electrostatic gating controls not only the low-power transmission of the device, but also the sign and magnitude of its nonlinear optical response.

4.3.4 Linear-regime optical simulation

The low-power transmission of the gated SLG device was simulated using the transfer matrix method. The simulated structure reproduced the experimental free-space geometry and consisted of a 1 mm-thick quartz substrate, the CVD SLG sheet, a 50 μm-thick ionic-liquid layer, and a 0.2 mm-thick quartz cover. The wavelength-dependent refractive index of quartz was calculated using the dispersion relation reported by Malitson [119], while the refractive index of the ionic liquid was taken from previous work on a similar device by the experimental group [113]. At 1566 nm, the corresponding values are approximately $n_{\mathrm{Q}} \simeq 1.44$ and $n_{\mathrm{IL}} \simeq 1.42$.

For each Raman-derived Fermi energy, the linear transmission of the multilayer stack was calculated and compared with the low-fluence experimental transmission extracted from the

nonlinear measurements. Because the Raman calibration yields discrete signed Fermi-energy values on both sides of the charge-neutrality point, the comparison is presented as a function of $|E_F|$, rather than directly as a function of gate voltage.

Figure 4.10 compares the experimental low-fluence transmission with the TMM prediction. The calculated transmission increases with $|E_F|$, reflecting the progressive suppression of interband absorption by Pauli blocking. The experimental data exhibit the same overall trend, although their absolute transmission baseline is lower than that predicted by the linear TMM calculation. To account empirically for this baseline difference, a constant additive offset of 0.4 percentage points was applied to the experimental transmission values. The same offset was applied consistently to all experimental transmission curves used in both the linear-regime comparison and the subsequent nonlinear-model analysis.

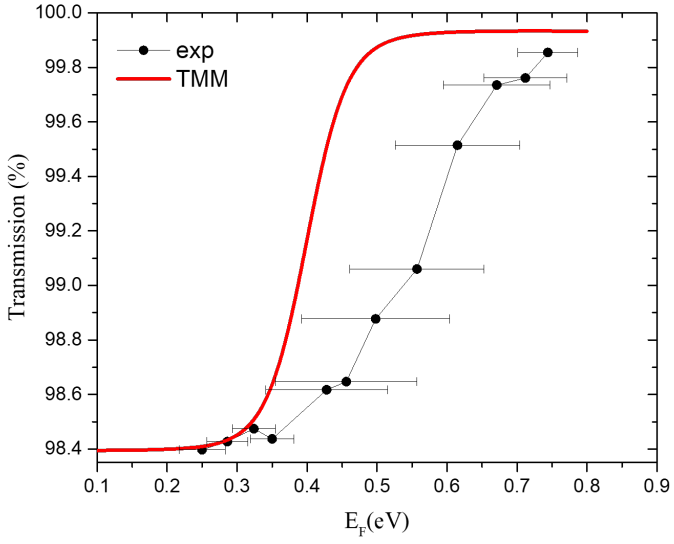

Figure 4.10: Linear-regime comparison between experiment and transfer-matrix simulation as a function of the Raman-derived $|E_F|$. The black points show the corrected experimental low-fluence transmission values extracted from the nonlinear measurements, with horizontal error bars indicating the uncertainty in the Raman-derived Fermi energy. A constant additive offset of 0.4 percentage points wasapplied to the experimental transmission values; the same offset was also used in the nonlinear analysis. The red curve shows the TMM calculation.

The corrected experimental data show an overall increase in transmission with $|E_F|$, in qualitative agreement with the TMM prediction. However, the experimental transition is broader and occurs at larger $|E_F|$ than predicted by the calculation. Since the applied constant offset affects only the absolute transmission baseline, it does not modify the shape of the experimental dependence. Therefore, the remaining discrepancies are more likely associated with uncertainty in the Raman-based Fermi-level extraction. Overall, the comparison supports the qualitative gate-dependent trend inferred from the Raman calibration, but does not quantitatively validate the absoluteE_F scale.

4.3.5 Nonlinear transmission simulation

Following the qualitative agreement obtained in the linear regime, the full nonlinear saturable-absorption model was used to simulate the fluence-dependent transmission curves. The simulations were performed at the experimental wavelength of 1566 nm, using a Gaussian pulse duration of 120 fs. The transient optical response was obtained by solving the coupled rate equations for the electronic temperature (Eq. (4.14)), the lattice temperature (Eq. (4.13)), and the non-equilibrium carrier density (Eq. (4.2)). The pulse-duration-dependent effective times $\tau_{\mathrm{opt,eff}}$ and $\tau_{\mathrm{ee,eff}}$ were used to account for the finite temporal width of the excitation pulse. For each simulation, the incident fluence was calculated by integrating the incident intensity profile over time,

$$F_{\mathrm{in}} = \int_{-\infty}^{\infty} I_{\mathrm{in}}(t)\,\mathrm{d}t. \tag{4.19}$$

The transmitted pulse energy per unit area was obtained by integrating the transmitted intensity over time, and the simulated transmission was therefore calculated as

$$T_{\mathrm{sim}} = \frac{F_{\mathrm{out}}}{F_{\mathrm{in}}} \times 100. \tag{4.20}$$

This procedure allows direct comparison with the experimental transmission curves reported as a function of incident fluence.

As in the linear-regime comparison, a constant additive offset of 0.4 percentage points was applied to all experimental transmission values before comparison with the nonlinear simulations. A global parameter set was used for all measured Fermi energies and incident fluences, rather than fitting each nonlinear-transmission curve independently.

To quantify the agreement between simulation and experiment, the root-mean-square error (RMSE) and a range-normalized RMSE (NRMSE) were used [120, 121]. The RMSE was calculated over all experimental points included in the comparison as

$$\mathrm{RMSE} = \sqrt{\frac{1}{N}\sum_{i=1}^{N}\left[T_{\mathrm{sim}}(F_i, E_{F,i}) - T_{\mathrm{exp}}(F_i, E_{F,i})\right]^2}, \tag{4.21}$$

where F_i is the incident fluence of the i-th experimental point, $E_{F,i}$ is the Fermi energy corresponding to that curve, and N is the total number of points included in the comparison. Since the transmission is expressed in percent, the RMSE is reported in percentage points. The range-normalized error was defined as

$$\mathrm{NRMSE} = \frac{\mathrm{RMSE}}{T_{\mathrm{max,exp}} - T_{\mathrm{min,exp}}} \times 100\%, \tag{4.22}$$

where $T_{\mathrm{max,exp}}$ and $T_{\mathrm{min,exp}}$ are the maximum and minimum experimental transmission values over the full data set.

To determine the parameter set that best reproduces the measured nonlinear transmission, separate two-dimensional parameter sweeps were performed for three fixed values of the electron–electron scattering time, $\tau_{\mathrm{ee},0} = 20$, 15, and 7 fs. For each value of $\tau_{\mathrm{ee},0}$, the

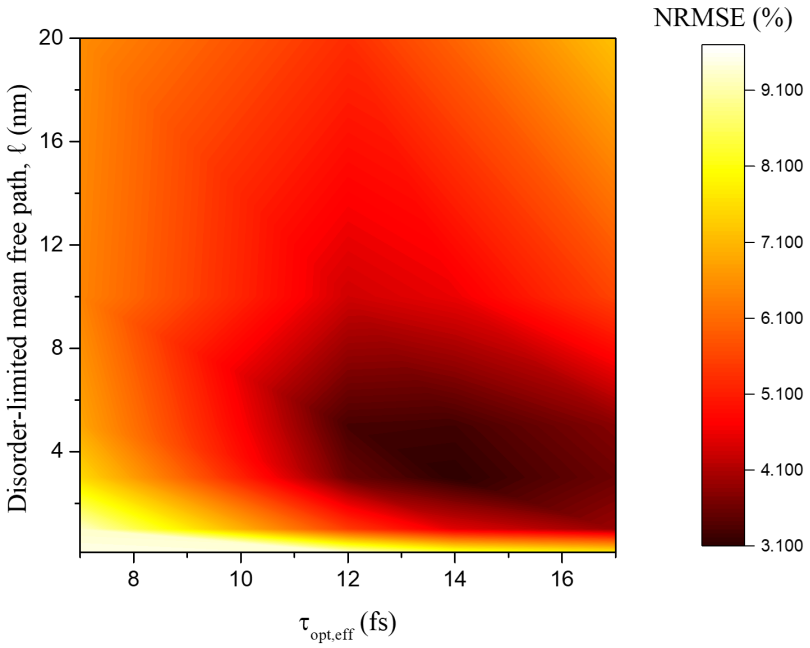

Figure 4.11: NRMSE obtained from the nonlinear-transmission comparison as a function of the effective optical dephasing time $\tau_{\mathrm{opt,eff}}$ and the disorder-limited electronic mean free path ℓ, for $\tau_{\mathrm{ee},0} = 7$ fs, which produced the lowest NRMSE among the examined electron–electron thermalization times. Within the sampled parameter grid, the minimum occurs at $\tau_{\mathrm{opt,eff}} = 14$ fs and $\ell = 3$ nm.

NRMSE was evaluated as a function of the effective optical dephasing time $\tau_{\mathrm{opt,eff}}$ and the disorder-limited electronic mean free path ℓ. The optical dephasing times were selected so that the corresponding effective values were $\tau_{\mathrm{opt,eff}} = 7$, 10, 12, 14, 15, and 17 fs. Each candidate parameter set was evaluated simultaneously against all experimental saturation curves of Fig. 4.9.

For $\tau_{\mathrm{ee},0} = 20$ fs, the minimum error was obtained at $\tau_{\mathrm{opt,eff}} = 10$ fs and $\ell = 3$ nm, with an NRMSE of 3.6%. For $\tau_{\mathrm{ee},0} = 15$ fs, the corresponding minimum occurred at $\tau_{\mathrm{opt,eff}} = 10$ fs and $\ell = 3$ nm, with an NRMSE of 3.2%. The lowest error among the examined cases was obtained for $\tau_{\mathrm{ee},0} = 7$ fs, $\tau_{\mathrm{opt,eff}} = 14$ fs, and $\ell = 3$ nm, with an NRMSE of 3.1%. This combination was therefore selected as the best-fit parameter set within the explored parameter space.

The effective optical dephasing time $\tau_{\mathrm{opt,eff}}$ determines the energetic width of the optically generated nonequilibrium carrier distribution. A shorter dephasing time produces a broader distribution, whereas a longer value concentrates the photoexcited carriers more strongly around the optically active energies. It therefore affects the spectral sharpness of the interband excitation and the strength of band-filling-induced Pauli blocking. In the present parameterization, however, varying $\tau_{\mathrm{opt,eff}}$ does not modify the excitation linewidth alone, but also $\tau_{\mathrm{ee,eff}}$. The scattering processes represented phenomenologically by τ_{opt} provide an additional relaxation pathway for the optically generated nonequilibrium population. Conse-

quently, shorter values of $\tau_{\mathrm{opt,eff}}$ are accompanied by shorter $\tau_{\mathrm{ee,eff}}$, reducing the persistence of nonequilibrium band filling and transferring the absorbed interband energy more rapidly to the thermalized electronic bath. The dependence along the $\tau_{\mathrm{opt,eff}}$ axis of Fig. 4.11 therefore represents the combined influence of excitation broadening and nonequilibrium-carrier relaxation, rather than either effect in isolation.

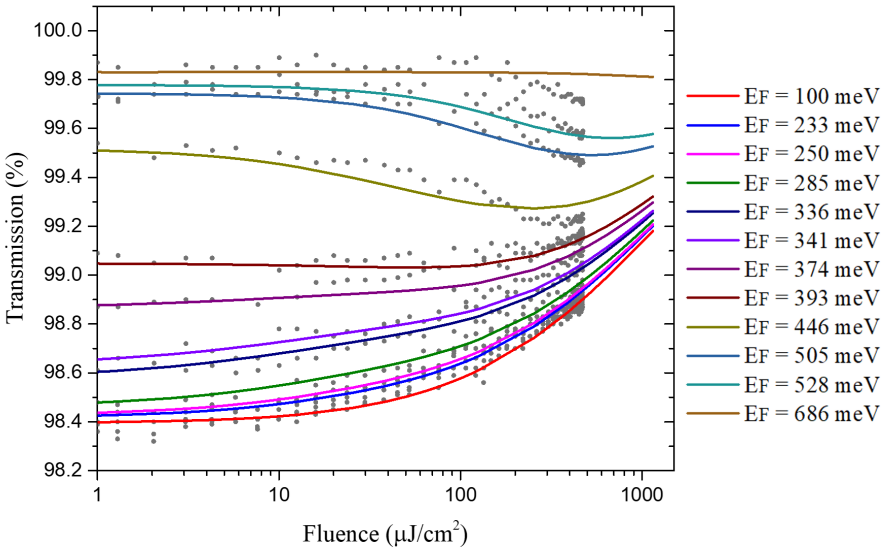

Figure 4.12: Comparison between the corrected experimental nonlinear-transmission data and the simulations obtained using the best-fit parameter set. Dots show the experimental data, while solid lines show the simulated transmission curves. The simulations were performed with $\tau_{\mathrm{ee},0} = 7$ fs, $\tau_{\mathrm{opt,eff}} = 14$ fs, and $\ell = 3$ nm.

The intrinsic electron–electron thermalization time $\tau_{\mathrm{ee},0}$ controls the rate at which the optically generated nonequilibrium carrier population relaxes toward a hot Fermi–Dirac distribution. A shorter $\tau_{\mathrm{ee},0}$ accelerates this redistribution, reducing the lifetime of the nonequilibrium population and therefore weakening the band-filling contribution to Pauli blocking. At the same time, the absorbed energy is transferred more rapidly to the thermalized electronic bath, increasing the relative importance of carrier heating. Conversely, a longer $\tau_{\mathrm{ee},0}$ allows the photoexcited population to persist for longer, strengthening nonequilibrium band filling and the associated bleaching of the interband absorption.

The disorder-limited electronic mean free path ℓ controls the strength of disorder-assisted acoustic-phonon cooling. A shorter ℓ corresponds to stronger supercollision cooling, whereas a longer ℓ weakens this cooling pathway and allows the electronic temperature to remain elevated for longer.

Using the best-fit parameter set, the simulated nonlinear-transmission curves are compared with the experimental data in Fig. 4.12. The simulations reproduce the main gate-dependent evolution of the nonlinear response, but point-to-point experimental scatter remains across the examined doping range.

For Fermi energies below the one-photon Pauli-blocking threshold, $|E_F| < \hbar\omega/2$, the simulated transmission increases monotonically with fluence. In this regime, the optically active interband transitions are initially allowed, while photoinduced band filling progressively suppresses the absorption through Pauli blocking. At the experimental wavelength of 1566 nm, Pauli-blocking threshold is $\hbar\omega/2 \simeq 0.396$ eV. The curve at $E_F = 393$ meV therefore lies close to this threshold and its transmission varies only weakly at low and intermediate fluences. Above the threshold, the calculated response becomes non-monotonic. For $E_F = 446$, 505, and 528 meV, the transmission initially decreases with fluence, reaches a minimum, and subsequently recovers. In this regime, equilibrium interband absorption is partially Pauli blocked. Electronic heating broadens the Fermi–Dirac distribution and restores optically allowed transitions, increasing the absorption and producing reverse saturable absorption. At higher fluence, nonequilibrium band filling becomes increasingly important and suppresses these restored transitions, causing the transmission to recover. Finally, at $E_F = 686$ meV, the calculated transmission remains nearly independent of fluence. At this doping level, the interband transition is strongly Pauli blocked throughout the examined fluence range. Thermal broadening therefore restores only a limited fraction of the interband absorption, resulting in a substantially weaker nonlinear response than at the intermediate Fermi energies.

The minimum NRMSE values obtained for $\tau_{\mathrm{ee},0} = 15$ fs and 7 fs, namely 3.2% and 3.1%, respectively, are very close. Although the latter value gives the lowest error among the examined cases and was therefore selected for the final comparison, the present analysis does not uniquely determine the intrinsic electron–electron thermalization time.

Chapter 5

Design of a Pulse-Shaping Device

The aim of this chapter is to use the nonlinear graphene model developed in the previous chapter as a design tool for a reflective pulse-shaping device. The underlying concept is to place graphene inside an asymmetric Fabry–Pérot cavity, where resonant field enhancement increases the effective light–graphene interaction. When the cavity is operated close to critical coupling, discussed in Sec. 2.5, small intensity-induced changes in graphene absorption can produce large variations in the reflected optical power. In this way, the microscopic saturable-absorption dynamics of graphene are converted into a macroscopic temporal reshaping of an incident optical pulse.

5.1 Bragg Reflector

The first step of the device design was the analysis of the optical response of the fabricated DBR, which was provided by experimental collaborators. The measured reflectivity spectrum was compared with transfer matrix simulations, as shown in Fig. 5.1, in order to validate the passive DBR used in the subsequent cavity design. The DBR consists of six alternating SiO_2/Ta_2O_5 pairs deposited on a quartz substrate. The layer thicknesses were taken as $d_{SiO_2} \simeq 274$ nm and $d_{Ta_2O_5} \simeq 193$ nm, while the refractive indices were set to $n_{SiO_2} \simeq 1.44$ and $n_{Ta_2O_5} \simeq 2.04$, based on literature optical data for fused silica and tantalum pentoxide, respectively [119, 122].

Figure 5.1 compares the measured reflectivity spectrum of the DBR with the TMM calculation. The simulation reproduces the main features of the experimental response, including the broad near-infrared stop band and the peak reflectivity of approximately $R \simeq 0.95$. The agreement is particularly good inside the stop band, which is the spectral region relevant for the cavity design. Deviations are observed mainly outside the stop band, especially at longer wavelengths, and can be attributed to fabrication tolerances, small deviations of the deposited layer thicknesses from the nominal values, material dispersion, surface roughness, and residual substrate-related reflections.

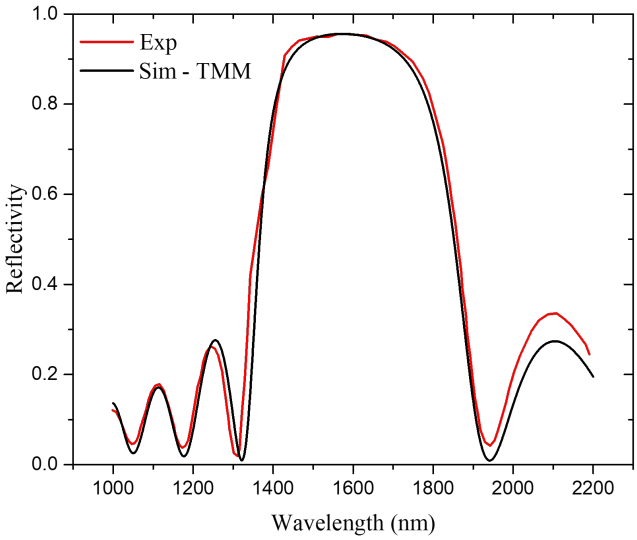

Figure 5.1: Experimental and simulated reflectivity spectra of the fabricated six-pair SiO_2/Ta_2O_5 dielectric Bragg reflector on a quartz substrate. The red curve shows the measured reflectivity, while the black curve corresponds to the transfer matrix method calculation. The calculation reproduces the broad near-infrared stop band validating the passive DBR description used in the cavity design.

5.2 Cavity design

After validating the passive DBR response, the same transfer matrix framework was used to design graphene-loaded Fabry–Pérot cavities. The general structure consists of the fabricated SiO_2/Ta_2O_5 DBR, a dielectric spacer layer, graphene, and a metallic Ag mirror. The last layer of the DBR is part of the optical boundary of the cavity and contributes to the effective phase condition, together with the spacer layer and the Ag mirror. The role of the cavity is to enhance the optical field at the graphene position and therefore increase the effective light–graphene interaction compared with single-pass propagation.

Two illumination geometries were examined, as shown schematically in Fig. 5.2. In the bottom-side geometry, Fig. 5.2 (a), light is incident through the quartz substrate and the DBR. In this case, the DBR acts as the input mirror, while the Ag layer serves as the back reflector. In the top-side geometry, Fig. 5.2 (b), light is incident from the Ag side of the structure. The metallic layer must therefore be thin enough to allow coupling of the incident field into the cavity, while remaining sufficiently reflective to support resonant field buildup.

Three spacer materials were considered: PMMA, Al_2O_3, and oligofluorene. The wavelength-dependent refractive indices of these materials were obtained from optical characterization performed by experimental collaborators and were used as input to the transfer matrix calculations. Near the target wavelength $\lambda_0 = 1572$ nm, the corresponding refractive-index values are approximately $n_{\mathrm{PMMA}} \simeq 1.477$, $n_{\mathrm{Al_2O_3}} \simeq 1.60$, and $n_{\mathrm{oligofluorene}} \simeq 1.68$, while the refractive index of Ag was taken from the literature [123]. The different refractive indices of the spacers mainly affect the physical spacer thickness, of the cavity, required to satisfy

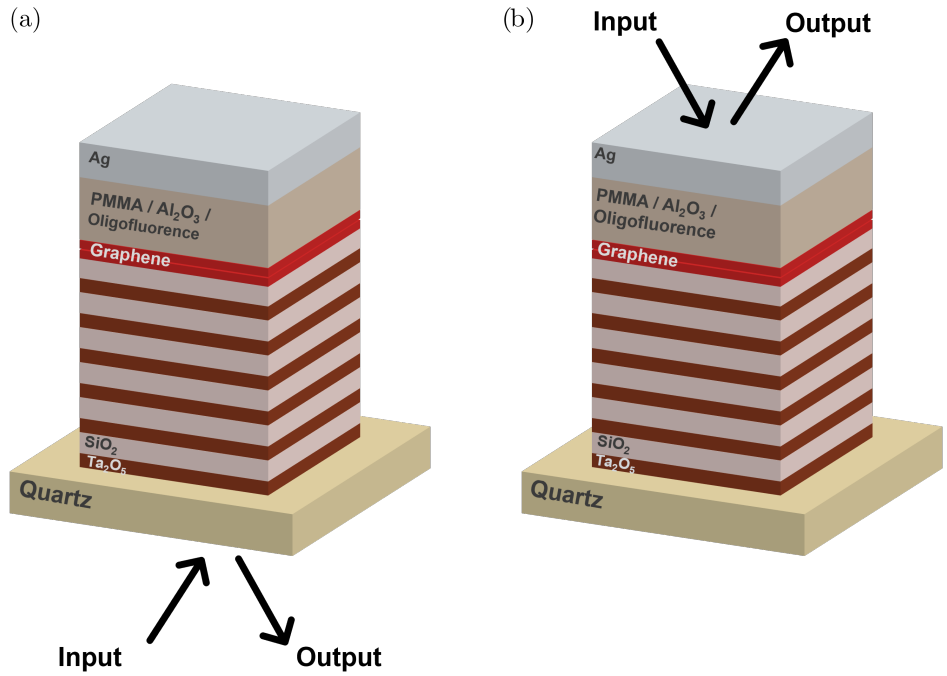

Figure 5.2: Schematic representation of the two illumination geometries considered for the graphene-loaded Fabry–Pérot cavity.(a) Bottom-side incidence, where light is incident through the quartz substrate and the SiO_2/Ta_2O_5 DBR, while the Ag layer acts as the back reflector. (b) Top-side incidence, where light is incident through the thin Ag layer, which acts as a partially transmitting input coupler.

the resonance condition at the target wavelength. In addition, the refractive-index mismatch between the spacer and the adjacent SiO_2 layer introduces a small reflection at their interface. Since the refractive index of PMMA is closest to that of SiO_2, the SiO_2/PMMA is expected to produce the smallest reflection.

To model structures containing N_G graphene layers, the graphene stack was treated within an independent-layer approximation. All layers were assumed to have the same Fermi level, electronic temperature, and lattice temperature. In the transfer matrix calculations, the stack was represented as a single graphene film with total thickness $N_G d_{SLG}$, where d_{SLG} is the thickness assigned to single-layer graphene. Consistently, the areal density of states entering the carrier-dynamics model was scaled according to $N_G \nu(\epsilon)$, where $\nu(\epsilon)$ is given by Eq. (2.7).

The design criterion was operation close to critical coupling. For a reflective one-port cavity, transmission is strongly suppressed by the back reflector, and the minimum in reflectivity corresponds to maximum cavity absorption. Critical coupling is reached when the radiative leakage rate through the input mirror matches the total internal loss rate of the cavity. In the present structures, the internal loss includes the absorption in graphene and the Ag mirror, while the dielectric layers are lossless in this spectral range. Therefore, the design problem requires simultaneous control of the mirror asymmetry, the cavity phase condition, and the graphene-induced internal loss.

The cavity design was carried out at the target wavelength $\lambda_0 = 1572$ nm. For each

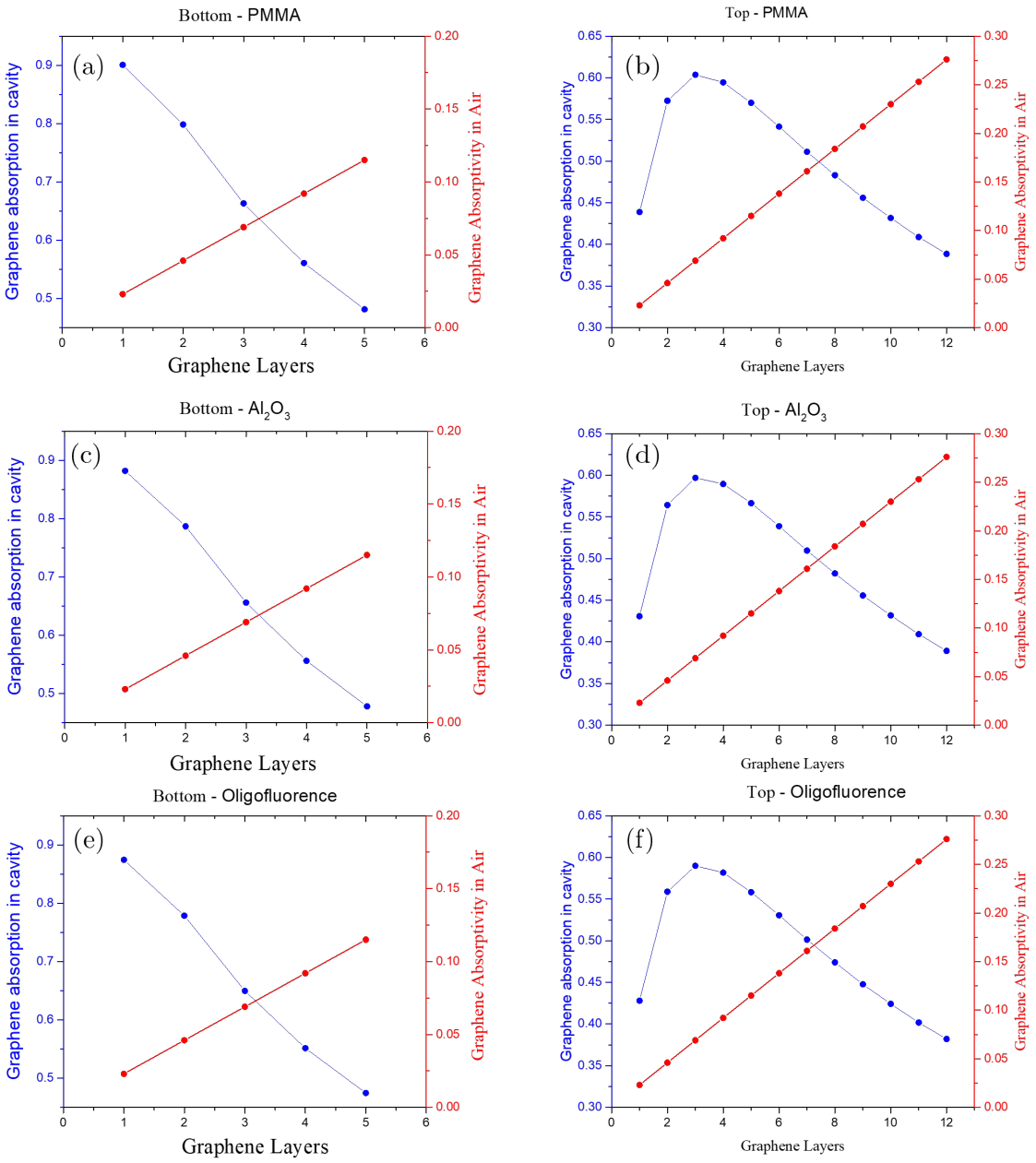

Figure 5.3: Graphene absorption as a function of the number of graphene layers for the different cavity designs. The blue curves show the fraction of the incident power absorbed in graphene when graphene is embedded inside the Fabry–Pérot cavity, $A_{\mathrm{G,cav}}$. The red curves show the corresponding graphene absorbance for the same number of layers in air, $A_{\mathrm{G,air}}$, without cavity enhancement. Panels (a), (c), and (e) correspond to bottom-side illumination for PMMA, Al_2O_3, and oligofluorene spacers, respectively. While, panels (b), (d), and (f) correspond to top-side illumination for the same spacer materials.

spacer material and illumination geometry, the cavity geometry was optimized for single-layer graphene at λ_0. The optimized cavities differ in their resonance linewidths, with the bottom-side designs generally exhibiting narrower resonances than the corresponding top-side designs. For example, in the PMMA-based cavities, the extracted quality factors are $Q_{\text{bottom}} \simeq 205$ and $Q_{\text{top}} \simeq 66$. The number of graphene layers was then varied while keeping the remaining structural parameters fixed. This fixed-geometry scan was used to isolate the effect of graphene loading on the cavity response and to identify the number of graphene layers for which the graphene absorption is maximized, as shown in Fig. 5.3.

Figure 5.3 shows that the graphene absorption inside the cavity, $A_{\text{G,cav}}$, is strongly enhanced compared with the corresponding absorbance of graphene in air, $A_{\text{G,air}}$. In air, the graphene absorbance increases monotonically with the number of layers [8]. Inside the cavity, however, the absorbed fraction is not determined only by the intrinsic graphene absorption, but also by the cavity coupling condition. Increasing the number of graphene layers initially increases the internal loss and drives the structure closer to critical coupling, thereby increasing $A_{\text{G,cav}}$. This trend is most clearly observed in the top-side geometries, shown in Figs. 5.3(b), (d), and (f). Beyond the optimum, however, the cavity becomes over-lossy: the quality factor is reduced, the photon lifetime becomes shorter, and the resonance broadens [79]. As a result, the intracavity field buildup weakens and the fraction of incident power absorbed in graphene decreases.

The same scan, shown in Fig. 5.3, also highlights the difference between the two illumination geometries. In the bottom-side devices, the maximum graphene absorption is reached with fewer graphene layers. This is related to the fact that the bottom-side structure behaves more closely as a reflective one-port absorber. In this geometry, transmission is strongly suppressed, so the field is more efficiently confined inside the cavity and a larger fraction of the circulating power can contribute to graphene absorption. In the top-side devices, part of the incident power remains unabsorbed through finite reflection and finite transmission, while another fraction is dissipated in the Ag input mirror. These channels reduce the resonant field enhancement at the graphene position, so each graphene layer contributes less effectively to the cavity loss balance, therefore, a larger number of graphene layers is required to approach the optimal coupling condition. The same mechanisms also prevent the graphene absorption from reaching 100%, as illustrated in Fig. 5.4 for the PMMA spacer.

Table 5.1: Optimized geometrical parameters and linear power balance for the top-side and bottom-side cavities with single-layer graphene at $\lambda_0 = 1572$ nm.

Geometry	Spacer material	d_{spacer} (nm)	d_{Ag} (nm)	R (%)	T (%)	A_{SLG} (%)	A_{Ag} (%)
Top-side	PMMA	219.35	11.62	0.44	40.45	43.88	15.23
Top-side	Al_2O_3	173.11	12.63	0.61	39.71	43.08	16.60
Top-side	Oligofluorene	192.21	13.13	0.80	39.46	42.81	16.93
Bottom-side	PMMA	239.95	177.89	0.79	0.00	90.07	9.14
Bottom-side	Al_2O_3	216.08	193.94	0.97	0.00	88.19	10.84
Bottom-side	Oligofluorene	209.05	177.78	1.16	0.00	87.42	11.42

The two-parameter optimization was performed for all spacer materials and for both illumination geometries by varying the spacer thickness and the Ag thickness. The spacer

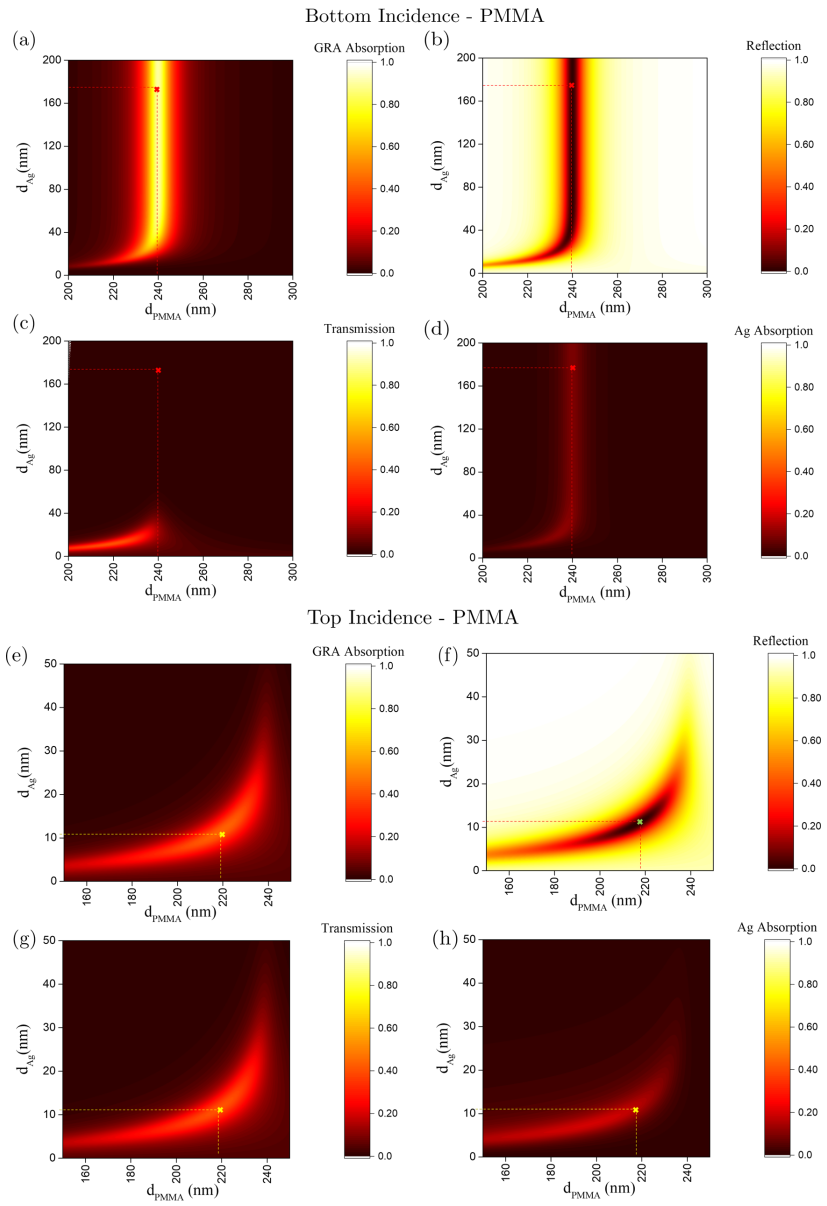

Figure 5.4: Two-parameter optimization of the PMMA-based cavity at $\lambda_0 = 1572$ nm with single-layer graphene. Panels (a)–(d) correspond to the bottom-side geometry, while panels (e)–(h) correspond to the top-side geometry. The maps show the graphene absorption A_{SLG}, reflection R, the transmission T and Ag absorption A_{Ag} as functions of the PMMA spacer thickness and the Ag thickness. The graphene absorption map identifies the region where the incident optical power is most efficiently dissipated in graphene.

thickness controls the cavity phase condition, while the Ag thickness controls the input coupling strength, top-side geometry, the metallic loss, and the transmission in the bottom-side configuration. Since the optimized responses of the three spacer materials were found to be qualitatively similar, the PMMA-based cavities are used as representative examples in the main text. The bottom-side and top-side PMMA optimization maps are shown in Fig. 5.4,

while the optimized geometrical parameters for all spacer materials are summarized in Table 5.1.

The PMMA optimization maps in Fig. 5.4 provide a visual confirmation of the cavity design criterion. In the bottom-side geometry, the selected operating point lies in a region where the graphene absorption is maximized, Fig. 5.4(a), while both reflection and transmission remain strongly suppressed, Figs. 5.4(b) and 5.4(c). The remaining non-graphene absorption is associated with the Ag mirror, Fig. 5.4(d), indicating that the optimized structure approaches, but does not reach, ideal graphene-only absorption.

In the top-side geometry, the optimum corresponds to a different compromise. The graphene absorption is still enhanced, Fig. 5.4(e), but a significant fraction of the incident power is transmitted through the structure, Fig. 5.4(g), while an additional fraction is absorbed in the thin Ag layer, Fig. 5.4(h). This behavior is consistent with the role of Ag as a partially transmitting input coupler in this illumination direction. Therefore, the PMMA maps support the conclusion drawn from Table 5.1: after optimization, the bottom-side configuration is more effective for concentrating the absorbed power in graphene. This behavior is also consistent with the extracted quality factors discussed above, since $Q_{\text{bottom}} \simeq 3Q_{\text{top}}$.

5.3 Extreme Pulse-Shaping

After the linear optimization of the graphene-loaded cavities, their nonlinear time-dependent response under pulsed excitation was investigated. The aim is to exploit graphene saturable absorption in order to dynamically tune the cavity through the critical-coupling condition during the pulse, thereby reshaping the temporal profile of the reflected signal.

The essential idea is to start from a cavity that is intentionally loaded with a larger number of graphene layers than the one required for critical coupling in the linear regime. Therefore, at low intensity pulse excitation the internal loss of the cavity is larger than the leakage rate through the input mirror, $\gamma_{\text{loss}}(0) > \gamma_{\text{leak}}$. As the instantaneous pulse intensity increases, graphene absorption decreases due to saturable absorption and can therefore drive the cavity dynamically towards the critical-coupling condition. Whenever graphene's absorption brings the total cavity loss close to the radiative leakage rate, the reflected signal is strongly suppressed as shown in Fig. 5.5.

The extreme reshaping of the pulse can then be achieved by the number of times and the position the pulse drives the cavity through critical coupling. Let I_{cc} denote the incident intensity at which the saturated graphene absorption reduces the cavity loss to the critical value. If I_{cc} is approximately equal to I_{peak}, the cavity reaches critical coupling at the maximum of the incident pulse, its central part is then almost completely absorbed by the cavity, producing a deep minimum in the reflected signal at the pulse center. Consequently, the single-peaked incident pulse is transformed into a reflected pulse with two side peaks Fig. 5.6(b).

A different response occurs when $I_{\text{cc}} < I_{\text{peak}}$. In this case, the critical-coupling condition is crossed twice: first on the rising edge of the pulse and then again on the falling edge. Between these two crossings, the graphene absorption is further saturated, the internal loss becomes smaller than the leakage rate, and the cavity moves away from critical coupling towards an under-lossy state. Reflection is therefore partially restored around the pulse max-

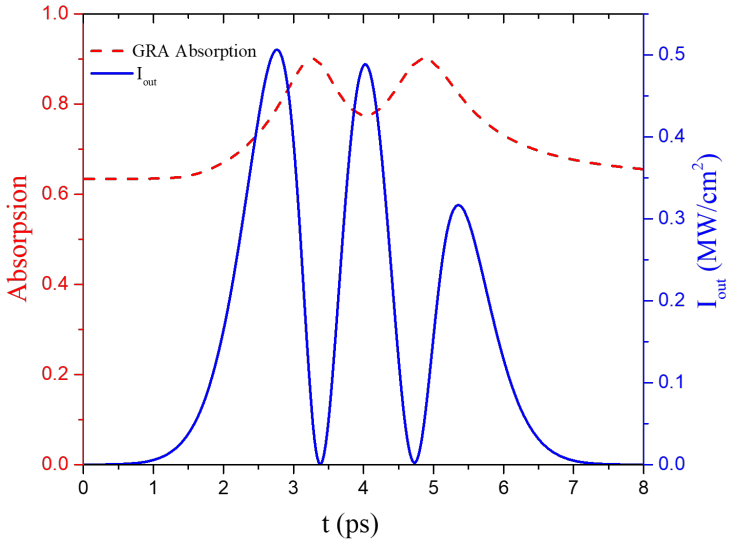

Figure 5.5: Temporal evolution of the nonlinear cavity response for a representative three-peak pulse-shaping case. The dashed red curve shows the instantaneous cavity absorption, while the blue curve shows the reflected output power. The reflected signal is suppressed when the graphene absorption reaches the maximum. Since this condition is crossed twice during the pulse, two reflection minima are formed and the reflected pulse splits into three.

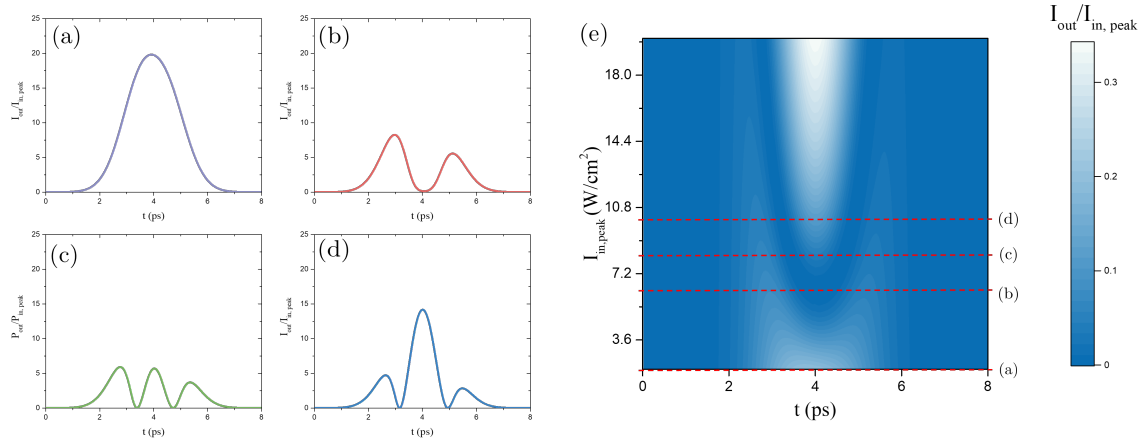

Figure 5.6: Pulse shaping in the optimized bottom-side PMMA cavity containing three graphene layers at $\lambda = 1579.13$ nm. Panels (a)–(d) show representative reflected pulse profiles for incident Gaussian pulses with peak intensities $I_{\text{in,peak}} = 2.0, 5.95, 8.56$, and $10.9\ \text{MW/cm}^2$, respectively. The reflected pulse evolves from a single peak in (a), to a two-peak profile in (b), and subsequently to three-peak profiles in (c) and (d). Panel (e) shows the normalized reflected intensity $I_{\text{out}}/I_{\text{in,peak}}$ as a function of time and incident peak intensity. The horizontal dashed lines indicate the intensities corresponding to the pulse profiles shown in panels (a)–(d).

imum and the output reflected signal, develops two temporal minima and can split into three local maxima Fig. 5.5.

Figure 5.6 summarizes this behavior for the configuration that gives the strongest output performance, namely the bottom-side PMMA cavity with three graphene layers. The calculation was performed at $\lambda = 1579.13$ nm, different from the original design wavelength, $\lambda_0 = 1572$ nm, because the cavity was first optimized for single-layer graphene. Figures 5.6(a)–(d) show representative reflected pulse profiles extracted from the map in Fig. 5.6(e). The incident pulse is a Gaussian pulse, and its peak intensity is varied while keeping the wavelength fixed. At $I_{\text{in,peak}} = 2.0\,\text{MW/cm}^2$, the reflected signal remains single-peaked, Fig. 5.6(a). Increasing the peak intensity to $I_{\text{in,peak}} = 5.95\ \text{MW/cm}^2$ drives the cavity close to critical coupling near the pulse maximum, producing a central reflection minimum and splitting the output into two peaks, Fig. 5.6(b). At $I_{\text{in,peak}} = 8.56\ \text{MW/cm}^2$ and $I_{\text{in,peak}} = 10.9\ \text{MW/cm}^2$ the critical-coupling condition is crossed twice during the pulse, leading to a three-peak reflected profile, Figs. 5.6(c) and (d).

The pulse-shaping performance of all optimized configurations is summarized in Table 5.2. For each geometry, spacer material, graphene-layer number, and target number of reflected peaks, the table lists the wavelength λ_{best} and incident peak intensity $I^{\text{best}}_{\text{in,peak}}$ that give the clearest pulse-splitting response. The wavelength tolerance $\lambda_{\text{tolerance}}$ denotes the approximate spectral range around λ_{best} over which the same two- or three-peak response remains identifiable. The quantity $I_{\text{out}}/I_{\text{in,peak}}$ represents the normalized reflected output, of the clearest response and is used here as a measure of the output efficiency of the pulse-shaped signal.

Table 5.2 reveals a trade-off between output efficiency and operational tolerance. The bottom-side configurations generally provide the highest normalized reflected output, with the best cases reaching $I_{\text{out}}/P_{\text{in,peak}} \simeq 8\%$. These structures are therefore more efficient for producing strong pulse-shaped reflected signals, consistent with the stronger resonant field buildup and more efficient graphene absorption obtained in the bottom-side geometry. By contrast, the top-side configurations generally require larger incident peak intensities and provide lower output efficiency. However, they usually exhibit larger wavelength tolerances. Thus, although the top-side geometry is less efficient in terms of output intensity, it is more forgiving with respect to experimental uncertainties, such as wavelength detuning, and small deviations of the fabricated layer thicknesses.

Table 5.2: Summary of the optimal wavelength, incident peak intensity, wavelength tolerance, and maximum normalized reflected output for each geometry, spacer material, graphene-layer number, and number of reflected peaks.

Geometry	Spacer	N_G	Peaks	λ^{best} (nm)	$I^{best}_{in,peak}$ (W/cm^2)	$\lambda^{tolerance}$ (nm)	$I_{out}/I_{in,peak}$ (%)
Bottom	Al_2O_3	1	2	1572.96	6.0×10^5	0.5 ± 0.1	0.3
Bottom	Al_2O_3	1	3	1572.86	7.7×10^5	0.5 ± 0.1	0.2
Bottom	Al_2O_3	2	2	1575.96	3.2×10^6	2.0 ± 0.2	3.7
Bottom	Al_2O_3	2	3	1576.12	5.0×10^6	2.2 ± 0.2	3.2
Bottom	Al_2O_3	3	2	1579.06	6.4×10^6	3.3 ± 0.3	8.1
Bottom	Al_2O_3	3	3	1579.06	8.8×10^6	3.3 ± 0.3	6.0
Bottom	Oligoluorence	1	2	1573.24	6.1×10^5	0.5 ± 0.1	0.3
Bottom	Oligoluorence	1	3	1573.39	9.6×10^5	0.5 ± 0.1	0.4
Bottom	Oligoluorence	2	2	1576.15	3.2×10^6	2.0 ± 0.2	3.8
Bottom	Oligoluorence	2	3	1576.32	5.0×10^6	2.0 ± 0.2	2.9
Bottom	Oligoluorence	3	2	1579.13	6.4×10^6	3.5 ± 0.2	8.0
Bottom	Oligoluorence	3	3	1579.13	8.8×10^6	3.1 ± 0.2	6.0
Bottom	PMMA	1	2	1572.93	4.8×10^5	0.4 ± 0.2	0.3
Bottom	PMMA	1	3	1572.93	7.3×10^5	0.4 ± 0.2	0.2
Bottom	PMMA	2	2	1575.96	3.0×10^6	2.3 ± 0.2	3.7
Bottom	PMMA	2	3	1575.76	4.3×10^6	2.1 ± 0.2	2.6
Bottom	PMMA	3	2	1579.13	6.0×10^6	3.3 ± 0.2	8.3
Bottom	PMMA	3	3	1579.13	8.6×10^6	3.6 ± 0.2	5.9
Top	Al_2O_3	4	2	1582.61	1.7×10^7	4.9 ± 0.3	3.4
Top	Al_2O_3	4	3	1582.32	4.1×10^7	4.1 ± 0.3	1.5
Top	Al_2O_3	5	2	1585.61	2.3×10^7	4.9 ± 0.3	4.7
Top	Al_2O_3	5	3	1585.03	5.5×10^7	4.9 ± 0.3	2.0
Top	Al_2O_3	6	2	1588.68	2.5×10^7	7.0 ± 0.4	6.9
Top	Al_2O_3	6	3	1587.21	6.0×10^7	5.5 ± 0.4	2.9
Top	Oligoluorence	4	2	1582.61	1.8×10^7	4.1 ± 0.3	3.6
Top	Oligoluorence	4	3	1582.61	5.3×10^7	3.8 ± 0.3	1.3
Top	Oligoluorence	5	2	1585.69	2.3×10^7	5.1 ± 0.3	5.1
Top	Oligoluorence	5	3	1585.05	6.4×10^7	4.5 ± 0.3	1.9
Top	Oligoluorence	6	2	1588.63	2.9×10^7	6.3 ± 0.4	6.3
Top	Oligoluorence	6	3	1587.37	7.2×10^7	5.5 ± 0.4	2.6
Top	PMMA	4	2	1582.88	1.8×10^7	5.0 ± 0.3	3.2
Top	PMMA	4	3	1582.62	4.3×10^7	4.2 ± 0.3	1.4
Top	PMMA	5	2	1585.92	2.1×10^7	5.6 ± 0.3	5.0
Top	PMMA	5	3	1585.58	5.7×10^7	5.3 ± 0.3	2.0
Top	PMMA	6	2	1588.68	2.5×10^7	7.5 ± 0.4	6.9
Top	PMMA	6	3	1587.58	6.0×10^7	6.5 ± 0.4	2.9

Chapter 6

Conclusions

The results of this thesis show that the saturation intensity of graphene should not be treated as a universal material constant. The large variation among reported values persists even after normalization with respect to excitation wavelength, saturable absorbance, and the effective number of graphene layers. No systematic dependence was identified on the experimental method, fabrication route, substrate or host material, or Raman ratio I_D/I_G. The measured saturation response should therefore be interpreted as the combined outcome of carrier dynamics, excitation conditions, optical environment, graphene morphology, and the definitions and fitting conventions used to extract the saturation parameters.

Comparison with the gated-graphene measurements showed that a common set of carrier-dynamics parameters can reproduce the main doping-dependent evolution of the nonlinear transmission. The agreement is strongest at lower Fermi energies, where non-equilibrium band filling dominates the response, while larger deviations appear at higher Fermi energies, where carrier heating plays a greater role. The comparison therefore supports the physical consistency of the model and its ability to describe the crossover between saturable and reverse saturable absorption, although it does not constitute a complete quantitative validation of all thermal processes included in the model.

The device-design calculations demonstrated that resonant enhancement can overcome the weak single-pass interaction between light and graphene. When graphene is incorporated into an asymmetric Fabry–Pérot cavity, its intensity-dependent absorption can produce strong temporal modulation of the reflected optical signal. In particular, operation close to critical coupling can transform a single incident pulse into reflected profiles containing two or three distinct peaks. The strongest pulse-shaping performance was obtained for the bottom-side PMMA cavity containing three graphene layers.

More generally, the bottom-side structures provided stronger graphene absorption, higher reflected output intensities, and operation at lower incident intensities. The top-side structures produced weaker output modulation but preserved the desired pulse profiles over broader wavelength and incident-intensity ranges. The two geometries therefore exhibit a clear trade-off between maximum pulse-shaping performance and tolerance to experimental deviations. Overall, the results demonstrate how the transient carrier dynamics of graphene can be translated, through resonant cavity engineering, into a substantial and controllable temporal modulation of a reflected optical pulse.

Appendix A

Estimate of third-harmonic generation

The main nonlinear mechanism considered in this thesis is the intensity-dependent saturable absorption of graphene at the fundamental frequency. Nevertheless, graphene also possesses a third-order nonlinear optical response and can therefore generate radiation at the third-harmonic frequency [54–56]. This process was examined separately in order to verify that the generated third-harmonic signal is negligible compared with the optical power remaining at the fundamental frequency.

The field at the fundamental frequency is first calculated with the transfer-matrix method. The local field at the graphene position is then used to evaluate the nonlinear sheet current at 3ω. Finally, this current is treated as a source term and the emitted third-harmonic field is propagated through the surrounding multilayer structure using the transfer-matrix formalism.

For a normally incident plane wave at the fundamental frequency ω, the incident intensity I_0 is related to the incident electric-field amplitude by

$$I_0 = \frac{1}{2} n_{\text{in}} \varepsilon_0 c \left| E_{\text{inc}}(\omega) \right|^2 , \tag{A.1}$$

where n_{in} is the refractive index of the incident medium. The transfer-matrix calculation at the fundamental frequency gives the local field enhancement at the graphene sheet,

$$\mathcal{F}_\omega = \frac{E_{\text{g}}(\omega)}{E_{\text{inc}}(\omega)}, \tag{A.2}$$

where $E_{\text{g}}(\omega)$ is the total electric field acting on graphene. Hence,

$$E_{\text{g}}(\omega) = \mathcal{F}_\omega \sqrt{\frac{2I_0}{n_{\text{in}} \varepsilon_0 c}}. \tag{A.3}$$

The nonlinear sheet current generated at the third-harmonic frequency is written as [54–56]

$$J^{(3)}_{\text{NL}}(3\omega) = \sigma^{(3)}_{\text{SLG}}(3\omega; \omega, \omega, \omega) \left[E_{\text{g}}(\omega) \right]^3 . \tag{A.4}$$

Substituting Eq. (A.3) into Eq. (A.4) gives

$$J^{(3)}_{\text{NL}}(3\omega) = \sigma^{(3)}_{\text{SLG}}(3\omega; \omega, \omega, \omega) \mathcal{F}_\omega^3 \left(\frac{2I_0}{n_{\text{in}} \varepsilon_0 c} \right)^{3/2} . \tag{A.5}$$

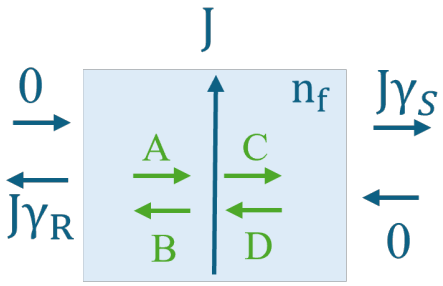

Figure A.1: Source-current transfer-matrix configuration used for the calculation of the emitted third-harmonic field. The nonlinear sheet current $J = J_{\mathrm{NL}}^{(3)}(3\omega)$ is embedded in a layer of refractive index n_f and radiates outgoing waves $J\gamma_R$ and $J\gamma_S$ towards the left and right sides of the structure, respectively. No third-harmonic wave is incident from either side. The amplitudes A, B and C, D denote the counter-propagating fields immediately to the left and right of the source.

The optical stacks on the two sides of the source are described by two transfer matrices, denoted by L and R. The matrix L connects the field amplitudes at the graphene position to the outgoing wave on the left side of the structure, while R connects the field amplitudes at the graphene position to the outgoing wave on the right side. The total transfer matrix is

$$M = RL. \tag{A.6}$$

The electric-field amplitudes immediately to the left of the nonlinear source are denoted by E_A and E_B, while those immediately to the right are denoted by E_C and E_D, as shown in Fig. A.1. The outgoing third-harmonic waves emitted by the source are written as

$$E_{\mathrm{R,out}}(3\omega) = J_{\mathrm{NL}}^{(3)}(3\omega)\gamma_R, \tag{A.7}$$

and

$$E_{\mathrm{S,out}}(3\omega) = J_{\mathrm{NL}}^{(3)}(3\omega)\gamma_S. \tag{A.8}$$

Here, γ_R and γ_S are the transfer coefficients from the nonlinear sheet current to the emitted third-harmonic fields on the two sides of the structure.

At the source position, the nonlinear surface current produces a discontinuity in the tangential magnetic field [44]. For normal incidence, this condition can be written in terms of the forward and backward electric-field amplitudes as

$$H^+ - H^- = J_{\mathrm{NL}}^{(3)} \quad \Rightarrow \quad E^+ - E^- = \frac{J_{\mathrm{NL}}^{(3)}}{n_f \varepsilon_0 c}, \tag{A.9}$$

where n_f is the refractive index of the layer in which the source is embedded and $\xi = 2n_f\varepsilon_0 c$. The electric-field amplitudes on the two sides of the source are then related by

$$E_C = E_A + \frac{J_{\mathrm{NL}}^{(3)}}{\xi}, \tag{A.10}$$

and

$$E_D = E_B - \frac{J_{\mathrm{NL}}^{(3)}}{\xi}. \tag{A.11}$$

Since there is no incident third-harmonic wave from either side, as shown in Fig. A.1, the source problem is written as

$$\begin{pmatrix} E_A \\ E_B \end{pmatrix} = L \begin{pmatrix} 0 \\ J_{\mathrm{NL}}^{(3)} \gamma_R \end{pmatrix}, \tag{A.12}$$

and

$$\begin{pmatrix} J_{\mathrm{NL}}^{(3)} \gamma_S \\ 0 \end{pmatrix} = R \begin{pmatrix} E_C \\ E_D \end{pmatrix}. \tag{A.13}$$

where

$$L = \begin{pmatrix} L_{11} & L_{12} \\ L_{21} & L_{22} \end{pmatrix}, \qquad R = \begin{pmatrix} R_{11} & R_{12} \\ R_{21} & R_{22} \end{pmatrix}, \tag{A.14}$$

Eq. (A.12) gives

$$E_A = L_{12} J_{\mathrm{NL}}^{(3)} \gamma_R, \tag{A.15}$$

and

$$E_B = L_{22} J_{\mathrm{NL}}^{(3)} \gamma_R. \tag{A.16}$$

Using Eqs. (A.10) and (A.11), the fields on the right side of the source become

$$E_C = J_{\mathrm{NL}}^{(3)} \left(L_{12} \gamma_R + \frac{1}{\xi} \right), \tag{A.17}$$

and

$$E_D = J_{\mathrm{NL}}^{(3)} \left(L_{22} \gamma_R - \frac{1}{\xi} \right). \tag{A.18}$$

Combining Eqs. (A.12), (A.13), (A.15) and (A.16) we get

$$\gamma_R = \frac{1}{\xi} \frac{R_{22} - R_{21}}{M_{22}}. \tag{A.19}$$

and

$$\gamma_S = M_{12} \gamma_R + \frac{R_{11} - R_{12}}{\xi}. \tag{A.20}$$

where $M_{22} = R_{21} L_{12} + R_{22} L_{22}$ and $M_{12} = R_{11} L_{12} + R_{12} L_{22}$. Equations (A.19) and (A.20) give the transfer of the nonlinear sheet current into outgoing third-harmonic waves on the two sides of the multilayer device.

The emitted intensity on either side $q = R, S$ may be written as

$$I_q^{(3\omega)} = \frac{1}{2} n_{q,\mathrm{out}}(3\omega) \varepsilon_0 c \left| \gamma_q \right|^2 \left| \sigma_{\mathrm{SLG}}^{(3)}(3\omega; \omega, \omega, \omega) \right|^2 \left| \mathcal{F}_\omega \right|^6 \left(\frac{2 I_0}{n_{\mathrm{in}} \varepsilon_0 c} \right)^3. \tag{A.21}$$

The total emitted third-harmonic intensity is

$$I_{\mathrm{THG}} = I_{\mathrm{R}}^{(3\omega)} + I_{\mathrm{S}}^{(3\omega)}. \tag{A.22}$$

The corresponding conversion efficiency is defined as

$$\eta_{\mathrm{THG}} = \frac{I_{\mathrm{THG}}}{I_0} = \frac{I_{\mathrm{R}}^{(3\omega)} + I_{\mathrm{S}}^{(3\omega)}}{I_0}. \tag{A.23}$$

Since the emitted third-harmonic intensity scales as I_0^3, the conversion efficiency scales as

$$\eta_{\mathrm{THG}} \propto I_0^2. \tag{A.24}$$

The transfer-matrix source implementation was verified against finite-element simulations performed in COMSOL Multiphysics. The FEM validation follows the standard frequency-domain formulation of Maxwell's equations for electromagnetic waves [124, 125]. The validation was carried out in the simplified free-standing air/graphene/air geometry shown in Fig. A.2, and not in the full Bragg-cavity device. The purpose of this comparison was to benchmark the nonlinear sheet-current treatment and the corresponding emitted third-harmonic power.

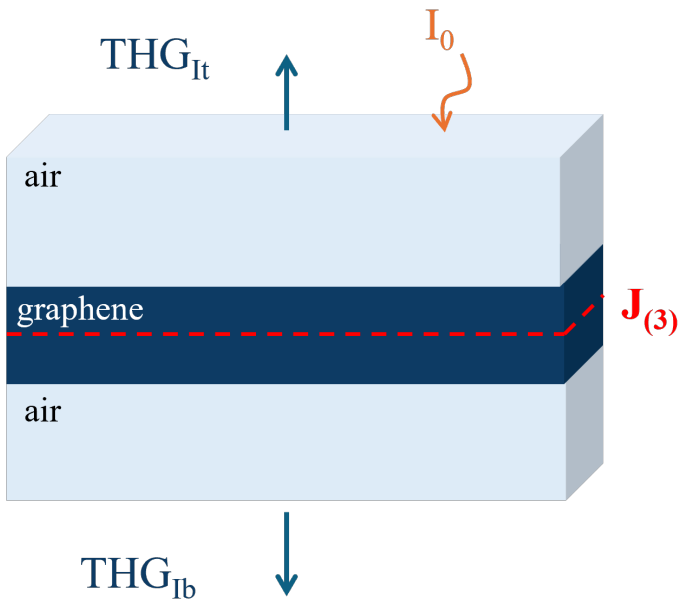

Figure A.2: Geometry used for the FEM validation of the third-harmonic source-current implementation. A graphene sheet is placed between two semi-infinite air regions. The incident fundamental intensity I_0 drives a nonlinear surface current $J^{(3)}(3\omega)$, which radiates third-harmonic fields towards the top and bottom sides, with emitted intensities $I_{\mathrm{t}}^{(3\omega)}$ and $I_{\mathrm{b}}^{(3\omega)}$, respectively. This simplified geometry is used only for validation; the actual device calculation is performed for the full Bragg-cavity multilayer structure.

In the FEM validation, the calculation was performed in two frequency-domain steps. First, the air/graphene/air geometry was solved at the fundamental frequency ω. In the surrounding air domains, the linear field satisfies

$$\nabla \times \mu_0^{-1} \nabla \times \mathbf{E}_\omega - \omega^2 \varepsilon_0 \varepsilon_r \mathbf{E}_\omega = 0. \tag{A.25}$$

At the graphene sheet, the linear optical response was introduced through the surface-current boundary condition using the graphene sheet conductivity calculated from the Kubo formalism [46, 47],

$$\hat{\mathbf{n}} \times (\mathbf{H}_{2,\omega} - \mathbf{H}_{1,\omega}) = \sigma^{(1)}_{\mathrm{SLG}}(\omega)\mathbf{E}_{\mathrm{g}}(\omega), \tag{A.26}$$

where $\mathbf{E}_{\mathrm{g}}(\omega)$ is the local electric field at the graphene interface. This first solve was used only to obtain the local fundamental field that drives the nonlinear current.

The third-order sheet conductivity $\sigma^{(3)}_{\mathrm{SLG}}(3\omega;\omega,\omega,\omega)$ was calculated externally using the nonlinear conductivity formalism for graphene [54–56] and was then used to define the nonlinear surface current

$$\mathbf{J}^{(3)}_{\mathrm{NL}}(3\omega) = \sigma^{(3)}_{\mathrm{SLG}}(3\omega;\omega,\omega,\omega)\,[\mathbf{E}_{\mathrm{g}}(\omega)]^3\,. \tag{A.27}$$

In the second step, the electromagnetic problem was solved at the third-harmonic frequency 3ω. At the graphene sheet, the total surface current at 3ω was written as the sum of the linear graphene response at the generated frequency and the externally imposed nonlinear source current:

$$\hat{\mathbf{n}} \times (\mathbf{H}_{2,3\omega} - \mathbf{H}_{1,3\omega}) = \sigma^{(1)}_{\mathrm{SLG}}(3\omega)\mathbf{E}_{3\omega} + \mathbf{J}^{(3)}_{\mathrm{NL}}(3\omega). \tag{A.28}$$

Thus, in the validation problem, graphene acts both as a linear conductive sheet at 3ω and as a nonlinear source radiating at the generated frequency.

The emitted third-harmonic power was obtained from the outward time-averaged Poynting flux,

$$P^{(3\omega)}_{\mathrm{FEM}} = \int_{\partial\Omega} \frac{1}{2}\,\mathrm{Re}\,[\mathbf{E}_{3\omega} \times \mathbf{H}^{*}_{3\omega}] \cdot \hat{\mathbf{n}}\, dS. \tag{A.29}$$

For the same symmetric air/graphene/air geometry, the emitted third-harmonic power density calculated from the transfer-matrix source formulation is

$$I^{(3\omega)}_{\mathrm{t}} = \frac{1}{2}\varepsilon_0 c \left| J^{(3)}_{\mathrm{NL}}(3\omega)\gamma_R \right|^2, \tag{A.30}$$

and

$$I^{(3\omega)}_{\mathrm{b}} = \frac{1}{2}\varepsilon_0 c \left| J^{(3)}_{\mathrm{NL}}(3\omega)\gamma_S \right|^2. \tag{A.31}$$

Due to the symmetry of the validation geometry, the two emitted powers are equal. The validation was carried out at

$$\lambda_\omega = 1550\ \mathrm{nm}, \qquad E_F = 0.2\ \mathrm{eV}. \tag{A.32}$$

For these parameters, the source coefficient satisfies

$$|\gamma_{R,S}\varepsilon_0 c| \simeq 0.50, \tag{A.33}$$

as expected for a symmetric source radiating into two air half-spaces.

The transfer-matrix source calculation and the FEM power outflow agree within approximately 10% over the full intensity range. The comparison also preserves the expected cubic dependence of the emitted third-harmonic power on the incident field amplitude.

After this validation, the same modified transfer-matrix formulation was used to estimate the third-harmonic emission in the actual structures studied in this thesis. As a representative

Table A.1: Comparison between the transfer-matrix source calculation and the FEM power outflow for the free-standing air/graphene/air validation geometry. The third-harmonic power density corresponds to the emitted power outflow from one side of the graphene sheet.

I_0 (W/m^2)	$I_{\mathrm{THG,TMM}}$ (W/m^2)	$I_{\mathrm{THG,FEM}}$ (W/m^2)
1×10^{8}	4.24×10^{-15}	4.68×10^{-15}
2×10^{9}	3.39×10^{-11}	3.75×10^{-11}
3×10^{10}	1.15×10^{-7}	1.26×10^{-7}
4×10^{11}	2.71×10^{-4}	3.00×10^{-4}
5×10^{12}	5.30×10^{-1}	5.85×10^{-1}
6×10^{13}	9.16×10^{2}	1.01×10^{3}

case, the bottom-side PMMA cavity with single-layer graphene was considered at an incident intensity $I_0 = 2 \times 10^7$ W/cm^2 $= 2 \times 10^{11}$ W/m^2. This intensity is higher than the intensity at which the three-peak pulse shape appears for the corresponding single-layer graphene structure, as discussed in Chapter 5.

For this structure, the transfer coefficients obtained at the third-harmonic frequency were

$$|\gamma_R| = 5.96 \times 10^2, \qquad |\gamma_S| = 2.92. \tag{A.34}$$

The much larger value of $|\gamma_R|$ shows that the generated third-harmonic radiation is emitted mainly towards one side of the structure. The calculated generated third-harmonic power density was

$$I_{\mathrm{gen}}^{(3\omega)} = 1.22 \times 10^5 \text{ W/m}^2. \tag{A.35}$$

This value represents the total power density transferred from the fundamental field to the third-harmonic field. Therefore, it gives the relevant measure for possible pump depletion. Comparing it with the incident fundamental intensity gives

$$\frac{I_{\mathrm{gen}}^{(3\omega)}}{I_0} = \frac{1.22 \times 10^5}{2 \times 10^{11}} \simeq 6.1 \times 10^{-7}. \tag{A.36}$$

Therefore, even for a deliberately high incident intensity in the bottom-side PMMA single-layer graphene structure the generated third-harmonic power remain more than seven orders of magnitude smaller than the incident fundamental intensity. The third-harmonic channel therefore removes only a negligible fraction of the optical power from the fundamental wave. Consequently, third-harmonic generation is not included as a coupled mechanism in the main pulse-shaping model.

Bibliography

[1] Jean-Claude Diels and Wolfgang Rudolph. *Ultrashort Laser Pulse Phenomena: Fundamentals, Techniques, and Applications on a Femtosecond Time Scale*. Academic Press, Burlington, MA, 2 edition, 2006.

[2] Andrew M Weiner. Femtosecond pulse shaping using spatial light modulators. *Review of scientific instruments*, 71(5):1929–1960, 2000.

[3] R Stoian, M Boyle, A Thoss, A Rosenfeld, G Korn, and IV Hertel. Dynamic temporal pulse shaping in advanced ultrafast laser material processing. *Applied Physics A*, 77(2):265–269, 2003.

[4] Zhipei Sun, Amos Martinez, and Feng Wang. Optical modulators with 2d layered materials. *Nature Photonics*, 10(4):227–238, 2016.

[5] Julien Fatome, Stéphane Pitois, Aladji Kamagaté, Guy Millot, David Massoubre, and Jean-Louis Oudar. All-optical reshaping based on a passive saturable absorber microcavity device for future 160-gb/s applications. 19(4):245–247.

[6] Ursula Keller, Kurt J Weingarten, Franz X Kartner, Daniel Kopf, Bernd Braun, Isabella D Jung, Regula Fluck, Clemens Honninger, Nicolai Matuschek, and J Aus Der Au. Semiconductor saturable absorber mirrors (sesam's) for femtosecond to nanosecond pulse generation in solid-state lasers. *IEEE Journal of selected topics in QUANTUM ELECTRONICS*, 2(3):435–453, 1996.

[7] RI Woodward, RCT Howe, G Hu, F Torrisi, M Zhang, T Hasan, and EJR Kelleher. Few-layer mos2 saturable absorbers for short-pulse laser technology: current status and future perspectives. *Photonics Research*, 3(2):A30–A42, 2015.

[8] Qiaoliang Bao, Han Zhang, Yu Wang, Zhenhua Ni, Yongli Yan, Ze Xiang Shen, Kian Ping Loh, and Ding Yuan Tang. Atomic-layer graphene as a saturable absorber for ultrafast pulsed lasers. *Advanced Functional Materials*, 19(19):3077–3083, 2009.

[9] Amos Martinez, Kazuyuki Fuse, and Shinji Yamashita. Mechanical exfoliation of graphene for the passive mode-locking of fiber lasers. *Applied Physics Letters*, 99(12):121107, 2011.

[10] Amos Martinez and Zhipei Sun. Nanotube and graphene saturable absorbers for fibre lasers. *Nature Photonics*, 7:842–845, 2013.

[11] Gaozhong Wang, Aidan A Baker-Murray, and Werner J Blau. Saturable absorption in 2d nanomaterials and related photonic devices. *Laser & Photonics Reviews*, 13(7):1800282, 2019.

[12] Rahul Raveendran Nair, Peter Blake, Alexander N Grigorenko, Konstantin S Novoselov, Tim J Booth, Tobias Stauber, Nuno MR Peres, and Andre K Geim. Fine structure constant defines visual transparency of graphene. *science*, 320(5881):1308–1308, 2008.

[13] Mathieu Massicotte, Giancarlo Soavi, Alessandro Principi, and Klaas-Jan Tielrooij. Hot carriers in graphene – fundamentals and applications. *Nanoscale*, 13:8376–8411, 2021.

[14] D Popa, Z Sun, F Torrisi, T Hasan, F Wang, and AC Ferrari. Sub 200 fs pulse generation from a graphene mode-locked fiber laser. *Applied Physics Letters*, 97(20), 2010.

[15] Xi Peng and Yixin Yan. Graphene saturable absorbers applications in fiber lasers. *Journal of the European Optical Society-Rapid Publications*, 17(1):16, 2021.

[16] A Marini, JD Cox, and FJ García de Abajo. Theory of graphene saturable absorption. *Physical Review B*, 95(12):125408, 2017.

[17] Shunbin Lu, Shuqing Chen, Zhiwei Zheng, Han Zhang, Chujun Zhao, and Shuangchun Wen. Saturable absorption in graphene at 800 nm band. In *AOPC 2012: Laser Technology and Applications*, volume 8555 of *Proceedings of SPIE*, page 85551A. SPIE, 2012.

[18] FT Vasko. Saturation of interband absorption in graphene. *Physical Review B—Condensed Matter and Materials Physics*, 82(24):245422, 2010.

[19] Andrea Tomadin, Daniele Brida, Giulio Cerullo, Andrea C. Ferrari, and Marco Polini. Nonequilibrium dynamics of photoexcited electrons in graphene: Collinear scattering, auger processes, and the impact of screening. 88(3):035430, 2013.

[20] Andrea Tomadin, Sam M. Hornett, Hai I. Wang, Evgeny M. Alexeev, Andrea Candini, Camilla Coletti, Dmitry Turchinovich, Mathias Kläui, Mischa Bonn, Frank H. L. Koppens, Euan Hendry, Marco Polini, and Klaas-Jan Tielrooij. The ultrafast dynamics and conductivity of photoexcited graphene at different fermi energies. 4(5):eaar5313, 2018.

[21] D. Brida, A. Tomadin, C. Manzoni, Y. J. Kim, A. Lombardo, S. Milana, R. R. Nair, K. S. Novoselov, A. C. Ferrari, G. Cerullo, and M. Polini. Ultrafast collinear scattering and carrier multiplication in graphene. 4:1987, 2013.

[22] S Doukas, P Sharma, I Goykhman, and E Lidorikis. Electrical detection of graphene plasmons for mid-infrared photodetection and chemical sensing: a computational study. *Applied Physics Letters*, 121(5), 2022.

[23] Jessica R. Piper and Shanhui Fan. Total absorption in a graphene monolayer in the optical regime by critical coupling with a photonic crystal guided resonance. *ACS Photonics*, 1(4):347–353, 2014.

[24] Amnon Yariv. Critical coupling and its control in optical waveguide-ring resonator systems. *IEEE Photonics Technology Letters*, 14(4):483–485, 2002.

[25] Shanhui Fan, Wonjoo Suh, and John D. Joannopoulos. Temporal coupled-mode theory for the fano resonance in optical resonators. *Journal of the Optical Society of America A*, 20(3):569–572, 2003.

[26] Thomas Christopoulos, Odysseas Tsilipakos, and Emmanouil E. Kriezis. Temporal coupled-mode theory in nonlinear resonant photonics: From basic principles to contemporary systems with 2d materials, dispersion, loss, and gain. *Journal of Applied Physics*, 136(1), 2024.

[27] S Doukas, P Mensz, N Myoung, AC Ferrari, I Goykhman, and E Lidorikis. Thermionic graphene/silicon schottky infrared photodetectors. *Physical Review B*, 105(11):115417, 2022.

[28] A. C. Ferrari, J. C. Meyer, V. Scardaci, C. Casiraghi, M. Lazzeri, F. Mauri, S. Piscanec, D. Jiang, K. S. Novoselov, S. Roth, and A. K. Geim. Raman spectrum of graphene and graphene layers. 97(18):187401, 2006.

[29] Luiz Gustavo Cançado, Ado Jorio, Eduardo H. Martins Ferreira, Fernando Stavale, Carlos A. Achete, Rodrigo B. Capaz, Marcus V. O. Moutinho, Antonio Lombardo, Topi S. Kulmala, and Andrea C. Ferrari. Quantifying defects in graphene via raman spectroscopy at different excitation energies. *Nano Letters*, 11(8):3190–3196, 2011.

[30] Andrea C. Ferrari and Denis M. Basko. Raman spectroscopy as a versatile tool for studying the properties of graphene. *Nature Nanotechnology*, 8(4):235–246, 2013.

[31] Philip Richard Wallace. The band theory of graphite. *Physical review*, 71(9):622, 1947.

[32] Antonio H Castro Neto, Francisco Guinea, Nuno MR Peres, Kostya S Novoselov, and Andre K Geim. The electronic properties of graphene. *Reviews of modern physics*, 81(1):109–162, 2009.

[33] Neil W Ashcroft, N David Mermin, et al. Solid state physics, 1976.

[34] DSL Abergel, V Apalkov, J Berashevich, Klaus Ziegler, and Tapash Chakraborty. Properties of graphene: a theoretical perspective. *Advances in Physics*, 59(4):261–482, 2010.

[35] Andre K Geim and Konstantin S Novoselov. The rise of graphene. *Nature materials*, 6(3):183–191, 2007.

[36] Beidou Guo, Liang Fang, Baohong Zhang, and Jian Ru Gong. Graphene doping: a review. *Insciences J.*, 1(2):80–89, 2011.

[37] Fredrik Schedin, Andrei Konstantinovich Geim, Sergei Vladimirovich Morozov, Ew W Hill, Peter Blake, Mi I Katsnelson, and Kostya Sergeevich Novoselov. Detection of individual gas molecules adsorbed on graphene. *Nature materials*, 6(9):652–655, 2007.

[38] Jong Sik Oh, Kyong Nam Kim, and Geun Young Yeom. Graphene doping methods and device applications. *Journal of nanoscience and nanotechnology*, 14(2):1120–1133, 2014.

[39] Kostya S Novoselov, Andre K Geim, Sergei V Morozov, De-eng Jiang, Yanshui Zhang, Sergey V Dubonos, Irina V Grigorieva, and Alexandr A Firsov. Electric field effect in atomically thin carbon films. *science*, 306(5696):666–669, 2004.

[40] Franz Mandl. *Statistical physics*. John Wiley & Sons, 1991.

[41] Giancarlo Soavi, Gang Wang, Habib Rostami, David G Purdie, Domenico De Fazio, Teng Ma, Birong Luo, Junjia Wang, Anna K Ott, Duhee Yoon, et al. Broadband, electrically tunable third-harmonic generation in graphene. *Nature nanotechnology*, 13(7):583–588, 2018.

[42] Dong Sun, Grant Aivazian, Aaron M Jones, Jason S Ross, Wang Yao, David Cobden, and Xiaodong Xu. Ultrafast hot-carrier-dominated photocurrent in graphene. *Nature nanotechnology*, 7(2):114, 2012.

[43] Gabriele Giuliani and Giovanni Vignale. *Quantum theory of the electron liquid*. Cambridge university press, 2008.

[44] David J Griffiths. *Introduction to electrodynamics*. Cambridge University Press, 2023.

[45] Robert W Boyd, Alexander L Gaeta, and Enno Giese. Nonlinear optics. In *Springer handbook of atomic, molecular, and optical physics*, pages 1097–1110. Springer, 2008.

[46] George W Hanson. Dyadic green's functions and guided surface waves for a surface conductivity model of graphene. *Journal of Applied Physics*, 103(6), 2008.

[47] Leonid A Falkovsky. Optical properties of graphene. In *Journal of Physics: conference series*, volume 129, page 012004, 2008.

[48] Vipin Kumar. Linear and nonlinear optical properties of graphene: A review. *Journal of Electronic Materials*, 2021.

[49] Efthimios Kaxiras. Applications of band theory. In *Atomic and Electronic Structure of Solids*, pages 160–202. Cambridge University Press, 2003.

[50] Qiaoliang Bao and Kian Ping Loh. Graphene photonics, plasmonics, and broadband optoelectronic devices. *ACS nano*, 6(5):3677–3694, 2012.

[51] Jason Horng, Chi-Fan Chen, Baisong Geng, Caglar Girit, Yuanbo Zhang, Zhao Hao, Hans A Bechtel, Michael Martin, Alex Zettl, Michael F Crommie, et al. Drude conductivity of dirac fermions in graphene. *Physical Review B—Condensed Matter and Materials Physics*, 83(16):165113, 2011.

[52] Marco Romagnoli, Vito Sorianello, Michele Midrio, Frank HL Koppens, Cedric Huyghebaert, Daniel Neumaier, Paola Galli, Wolfgang Templ, Antonio D'Errico, and Andrea C Ferrari. Graphene-based integrated photonics for next-generation datacom and telecom. *Nature Reviews Materials*, 3(10):392–414, 2018.

[53] Kin Chung Fong and K. C. Schwab. Measurement of the electronic thermal conductance channels and heat capacity of graphene at low temperature. *Physical Review X*, 3:041008, 2013.

[54] Jin-Luo Cheng, Nathalie Vermeulen, and JE Sipe. Third order optical nonlinearity of graphene. *New Journal of Physics*, 16(5):053014, 2014.

[55] Jin Luo Cheng, Nathalie Vermeulen, and JE Sipe. Third-order nonlinearity of graphene: Effects of phenomenological relaxation and finite temperature. *Physical Review B*, 91(23):235320, 2015.

[56] Sergey A Mikhailov. Quantum theory of the third-order nonlinear electrodynamic effects of graphene. *Physical Review B*, 93(8):085403, 2016.

[57] Sergey A Mikhailov. Nonperturbative quasiclassical theory of the nonlinear electrodynamic response of graphene. *Physical Review B*, 95(8):085432, 2017.

[58] Habib Rostami and Marco Polini. Theory of third-harmonic generation in graphene: A diagrammatic approach. *Physical Review B*, 93(16):161411, 2016.

[59] Justin C. W. Song and Leonid S. Levitov. Energy flows in graphene: hot carrier dynamics and cooling. 27(16):164201, 2015.

[60] Torben Winzer, Andreas Knorr, and Ermin Malić. Carrier multiplication in graphene. 10(12):4839–4843, 2010.

[61] Justin C. W. Song, Klaas J. Tielrooij, Frank H. L. Koppens, and Leonid S. Levitov. Photoexcited carrier dynamics and impact-excitation cascade in graphene. 87(15):155429, 2013.

[62] K. J. Tielrooij, J. C. W. Song, S. A. Jensen, A. Centeno, A. Pesquera, A. Zurutuza Elorza, M. Bonn, L. S. Levitov, and F. H. L. Koppens. Photoexcitation cascade and multiple hot-carrier generation in graphene. 9:248–252, 2013.

[63] M. Breusing, S. Kuehn, T. Winzer, E. Malić, F. Milde, N. Severin, J. P. Rabe, C. Ropers, A. Knorr, and T. Elsaesser. Ultrafast nonequilibrium carrier dynamics in a single graphene layer. 83(15):153410, 2011.

[64] Dong Sun, Zong-Kwei Wu, Charles Divin, Xuebin Li, Claire Berger, Walt A. de Heer, Phillip N. First, and Theodore B. Norris. Ultrafast relaxation of excited dirac fermions in epitaxial graphene using optical differential transmission spectroscopy. 101(15):157402, 2008.

[65] Momchil T. Mihnev, Faris Kadi, Charles J. Divin, Torben Winzer, Seunghyun Lee, Che-Hung Liu, Zhaohui Zhong, Claire Berger, Walt A. de Heer, Ermin Malic, Andreas Knorr, and Theodore B. Norris. Microscopic origins of the terahertz carrier relaxation and cooling dynamics in graphene. 7:11617, 2016.

[66] Wang-Kong Tse and S. Das Sarma. Energy relaxation of hot dirac fermions in graphene. 79(23):235406, 2009.

[67] Farhan Rana, Paul A. George, Jared H. Strait, Jahan Dawlaty, Shriram Shivaraman, Mvs Chandrashekhar, and Michael G. Spencer. Carrier recombination and generation rates for intravalley and intervalley phonon scattering in graphene. 79(11):115447, 2009.

[68] Jahan M. Dawlaty, Shriram Shivaraman, Mvs Chandrashekhar, Farhan Rana, and Michael G. Spencer. Measurement of ultrafast carrier dynamics in epitaxial graphene. 92(4):042116, 2008.

[69] S. Arshia Khatoon, Meenhaz Ansari, S. S. Z. Ashraf, and M. Obaidurrahman. Inelastic scattering and cooling of photoexcited electrons through coupling with acoustic, optic, and surface polar optic phonons in graphene. 129(1):014308, 2021.

[70] Justin C. W. Song, Michael Y. Reizer, and Leonid S. Levitov. Disorder-assisted electron-phonon scattering and cooling pathways in graphene. 109(10):106602, 2012.

[71] Matt W. Graham, Su-Fei Shi, Daniel C. Ralph, Jiwoong Park, and Paul L. McEuen. Photocurrent measurements of supercollision cooling in graphene. 9:103–108, 2013.

[72] A. C. Betz, S. H. Jhang, E. Pallecchi, R. Ferreira, G. Fève, J.-M. Berroir, and B. Plaçais. Supercollision cooling in undoped graphene. 9:109–112, 2013.

[73] S. Piscanec, M. Lazzeri, Francesco Mauri, A. C. Ferrari, and J. Robertson. Kohn anomalies and electron-phonon interactions in graphite. 93(18):185503, 2004.

[74] Andrea C. Ferrari. Raman spectroscopy of graphene and graphite: Disorder, electron–phonon coupling, doping and nonadiabatic effects. 143(1–2):47–57, 2007.

[75] J. K. Viljas and T. T. Heikkilä. Electron-phonon heat transfer in monolayer and bilayer graphene. 81(24):245404, 2010.

[76] J. D. Joannopoulos, P. R. Villeneuve, and S. Fan. Photonic crystals: putting a new twist on light. *Nature*, 386:143–149, 1997.

[77] J. D. Joannopoulos, S. G. Johnson, J. N. Winn, and R. D. Meade. *Photonic Crystals: Molding the Flow of Light*. Princeton University Press, 2 edition, 2008.

[78] P. Yeh. *Optical Waves in Layered Media*. Wiley, 1988.

[79] Bahaa E. A. Saleh and Malvin Carl Teich. *Fundamentals of Photonics*. Wiley, 3 edition, 2019.

[80] Hermann A. Haus. *Waves and Fields in Optoelectronics*. Prentice Hall, 1984.

[81] Tom G. Mackay and Akhlesh Lakhtakia. *The Transfer-Matrix Method in Electromagnetics and Optics*. Synthesis Lectures on Electromagnetics. Springer International Publishing.

[82] Olivier Deparis. Poynting vector in transfer-matrix formalism for the calculation of light absorption profile in stratified isotropic optical media. *Optics letters*, 36(20):3960–3962, 2011.

[83] Josef Stoer, Roland Bulirsch, R Bartels, Walter Gautschi, and Christoph Witzgall. *Introduction to numerical analysis*, volume 1993. Springer, 1980.

[84] Uri M Ascher and Linda R Petzold. *Computer methods for ordinary differential equations and differential-algebraic equations*. SIAM, 1998.

[85] Augustus Matthiessen and August Christoph Carl Vogt. Iv. on the influence of temperature on the electric conducting-power of alloys. *Philosophical transactions of the Royal Society of London*, (154):167–200, 1864.

[86] Qiaoliang Bao, Han Zhang, Zhenhua Ni, Yu Wang, Lakshminarayana Polavarapu, Zexiang Shen, Qing-Hua Xu, Dingyuan Tang, and Kian Ping Loh. Monolayer graphene as a saturable absorber in a mode-locked laser. *Nano Research*, 4(3):297–307, 2011.

[87] Kuen Yao Lau, Xiaofeng Liu, and Jianrong Qiu. A comparison for saturable absorbers: carbon nanotube versus graphene. *Advanced Photonics Research*, 3(10):2200023, 2022.

[88] Anastasios D Koulouklidis, Anna C Tasolamprou, Spyros Doukas, Eudokia Kyriakou, M Said Ergoktas, Christina Daskalaki, Eleftherios N Economou, Coskun Kocabas, Elefterios Lidorikis, Maria Kafesaki, et al. Ultrafast terahertz self-induced absorption and phase modulation on a graphene-based thin film absorber. *ACS Photonics*, 9(9):3075–3082, 2022.

[89] Eric Pop, Vikas Varshney, and Ajit K Roy. Thermal properties of graphene: Fundamentals and applications. *MRS bulletin*, 37(12):1273–1281, 2012.

[90] TJ Echtermeyer, S Milana, U Sassi, A Eiden, M Wu, E Lidorikis, and AC Ferrari. Surface plasmon polariton graphene photodetectors. *Nano Letters*, 16(1):8–20, 2016.

[91] Guichuan Xing, Hongchen Guo, Xinhai Zhang, Tze Chien Sum, and Cheng Hon Alfred Huan. The physics of ultrafast saturable absorption in graphene. *Optics Express*, 18(5):4564–4573, 2010.

[92] Yanyan Feng, Ningning Dong, Yuanxin Li, Xiaoyan Zhang, Chunxia Chang, Saifeng Zhang, and Jun Wang. Host matrix effect on the near infrared saturation performance of graphene absorbers. *Optical Materials Express*, 5(4):802–808, 2015.

[93] Henrique Guimaraes Rosa, José Carlos Viana Gomes, and Eunézio A. Thoroh de Souza. Transfer of an exfoliated monolayer graphene flake onto an optical fiber end face for erbium-doped fiber laser mode-locking. *2D Materials*, 2(3):031001, 2015.

[94] Pulak C Debnath, Jaehyun Park, Austin M Scott, Junsu Lee, Ju Han Lee, and Yong-Won Song. In situ synthesis of graphene with telecommunication lasers for nonlinear optical devices. *Advanced Optical Materials*, 3(9):1264–1272, 2015.

[95] Han Zhang, Stéphane Virally, Qiaoliang Bao, Kian Ping Loh, Serge Massar, Nicolas Godbout, and Pascal Kockaert. Z-scan measurement of the nonlinear refractive index of graphene. *Optics Letters*, 37(11):1856–1858, 2012.

[96] Dmitry V. Khudyakov, Anatoly S. Lobach, Nataliya G. Spitsyna, and Valery A. Kazakov. Comparative analysis of nonlinear optical properties of single-layer graphene and few-layer graphene nanosheets. *Applied Physics B*, 125:224, 2019.

[97] Govind P. Agrawal. *Fiber-Optic Communication Systems*. John Wiley & Sons, Hoboken, NJ, 4 edition, 2012.

[98] Gerd Keiser. *Optical Fiber Communications*. McGraw-Hill, New York, 4 edition, 2010.

[99] S. C. Xu, B. Y. Man, S. Z. Jiang, D. J. Feng, S. B. Gao, C. S. Chen, M. Liu, C. Yang, C. Zhang, D. Bi, F. Y. Liu, and X. Meng. Sapphire-based graphene saturable absorber for long-time working femtosecond lasers. *Optics Letters*, 39(9):2707–2710, 2014.

[100] Henrique G. Rosa, Juan A. Castañeda, Carlos H. Brito Cruz, Lázaro A. Padilha, José C. V. Gomes, Eunézio A. Thoroh de Souza, and Hugo L. Fragnito. Controlled stacking of graphene monolayer saturable absorbers for ultrashort pulse generation in erbium-doped fiber lasers. *Optical Materials Express*, 7(7):2528–2537, 2017.

[101] D. G. Purdie, D. Popa, V. J. Wittwer, Z. Jiang, G. Bonacchini, F. Torrisi, S. Milana, E. Lidorikis, and A. C. Ferrari. Few-cycle pulses from a graphene mode-locked all-fiber laser. *Applied Physics Letters*, 106(25):253101, 2015.

[102] Felice Torrisi, Daniel Popa, Silvia Milana, Zhe Jiang, Tawfique Hasan, Elefterios Lidorikis, and Andrea C. Ferrari. Stable, surfactant-free graphene–styrene methyl-methacrylate composite for ultrafast lasers. *Advanced Optical Materials*, 4(7):1088–1097, 2016.

[103] S. Husaini and R. G. Bedford. Graphene saturable absorber for high power semiconductor disk laser mode-locking. *Applied Physics Letters*, 104(16):161107, 2014.

[104] In Hyung Baek, Hwang Woon Lee, Sukang Bae, Byung Hee Hong, Yeong Hwan Ahn, Dong-Il Yeom, and Fabian Rotermund. Efficient mode-locking of sub-70-fs ti:sapphire laser by graphene saturable absorber. *Applied Physics Express*, 5(3):032701, 2012.

[105] Won Bae Cho, Jun Wan Kim, Hwang Woon Lee, Sukang Bae, Byung Hee Hong, Sun Young Choi, In Hyung Baek, Kihong Kim, Dong-Il Yeom, and Fabian Rotermund. High-quality, large-area monolayer graphene for efficient bulk laser mode-locking near 1.25 micrometers. *Optics Letters*, 36(20):4089–4091, 2011.

[106] Elena Ugolotti, Andreas Schmidt, Valentin Petrov, Jun Wan Kim, Dong-Il Yeom, Fabian Rotermund, Sukang Bae, Byung Hee Hong, Antonio Agnesi, Christian Fiebig, Götz Erbert, Xavier Mateos, Magdalena Aguiló, Francesc Diaz, and Uwe Griebner. Graphene mode-locked femtosecond yb:kluw laser. *Applied Physics Letters*, 101(16):161112, 2012.

[107] W. D. Tan, C. Y. Su, R. J. Knize, G. Q. Xie, L. J. Li, and D. Y. Tang. Mode locking of ceramic nd:yttrium aluminum garnet with graphene as a saturable absorber. *Applied Physics Letters*, 96(3):031106, 2010.

[108] M. Sheik-Bahae, A. A. Said, T. H. Wei, D. J. Hagan, and E. W. Van Stryland. Sensitive measurement of optical nonlinearities using a single beam. *IEEE Journal of Quantum Electronics*, 26(4):760–769, 1990.

[109] Robert Fleischhaker, Nico Krauß, Farina Schättiger, and Thomas Dekorsy. Consistent characterization of semiconductor saturable absorber mirrors with single-pulse and pump-probe spectroscopy. *Optics express*, 21(6):6764–6776, 2013.

[110] Lili Miao, Yaqin Jiang, Shunbin Lu, Bingxin Shi, Chujun Zhao, Han Zhang, and Shuangchun Wen. Broadband ultrafast nonlinear optical response of few-layers graphene: toward the mid-infrared regime. *Photonics Research*, 3(5):214–219, 2015.

[111] Shinji Yamashita. Nonlinear optics in carbon nanotube, graphene, and related 2D materials. *APL Photonics*, 4(3):034301, 2019.

[112] ZhiBo Liu, XiaoLiang Zhang, XiaoQing Yan, YongSheng Chen, and JianGuo Tian. Nonlinear optical properties of graphene-based materials. *Chinese science bulletin*, 57(23):2971–2982, 2012.

[113] Eva A. A. Pogna, Andrea Tomadin, Osman Balci, Giancarlo Soavi, Ioannis Paradisanos, Michele Guizzardi, Paolo Pedrinazzi, Sandro Mignuzzi, Klaas-Jan Tielrooij, Marco Polini, Andrea C. Ferrari, and Giulio Cerullo. Electrically tunable nonequilibrium optical response of graphene. *ACS Nano*, 16(3):3613–3624, 2022.

[114] Anindya Das, Simone Pisana, Biswanath Chakraborty, Stefano Piscanec, Srijan K Saha, Umesh V Waghmare, Konstantin S Novoselov, Hulikal R Krishnamurthy, Andre K Geim, Andrea C Ferrari, et al. Monitoring dopants by raman scattering in an

electrochemically top-gated graphene transistor. *Nature nanotechnology*, 3(4):210–215, 2008.

[115] Ahmet Uysal, Hua Zhou, Guang Feng, Sang Soo Lee, Song Li, Paul Fenter, Peter T. Cummings, Pasquale F. Fulvio, Sheng Dai, John K. McDonough, and Yury Gogotsi. Structural origins of potential dependent hysteresis at the electrified graphene/ionic liquid interface. *The Journal of Physical Chemistry C*, 118(1):569–574, 2014.

[116] Jin Tae Kim, Hongkyw Choi, Yongsuk Choi, and Jeong Ho Cho. Ion-gel-gated graphene optical modulator with hysteretic behavior. *ACS Applied Materials & Interfaces*, 10(2):1836–1845, 2018.

[117] L. M. Malard, M. A. Pimenta, G. Dresselhaus, and M. S. Dresselhaus. Raman spectroscopy in graphene. *Physics Reports*, 473(5–6):51–87, 2009.

[118] Matteo Bruna, Anna K Ott, Mari Ijäs, Duhee Yoon, Ugo Sassi, and Andrea C Ferrari. Doping dependence of the raman spectrum of defected graphene. *Acs Nano*, 8(7):7432–7441, 2014.

[119] Ian H Malitson. Interspecimen comparison of the refractive index of fused silica. *Journal of the optical society of America*, 55(10):1205–1209, 1965.

[120] Neil D. Bennett, Barry F. W. Croke, Giorgio Guariso, Joseph H. A. Guillaume, Serena H. Hamilton, Anthony J. Jakeman, Stefano Marsili-Libelli, Lachlan T. H. Newham, John P. Norton, Charles Perrin, Suzanne A. Pierce, Barbara Robson, Ralf Seppelt, Alexey A. Voinov, Brian D. Fath, and Vazken Andreassian. Characterising performance of environmental models. *Environmental Modelling & Software*, 40:1–20, 2013.

[121] Tianfeng Chai and Roland R. Draxler. Root mean square error (RMSE) or mean absolute error (MAE)? – arguments against avoiding RMSE in the literature. *Geoscientific Model Development*, 7(3):1247–1250, 2014.

[122] Daniel Franta, David Nečas, Ivan Ohlídal, and Angelo Giglia. Dispersion model for optical thin films applicable in wide spectral range. In *Optical Systems Design 2015: Optical Fabrication, Testing, and Metrology V*, volume 9628, pages 342–353. SPIE, 2015.

[123] Peter B Johnson and R-WJPrB Christy. Optical constants of the noble metals. *Physical review B*, 6(12):4370, 1972.

[124] Jian-Ming Jin. *The Finite Element Method in Electromagnetics*. Wiley-IEEE Press, Hoboken, NJ, 3 edition, 2014.

[125] John David Jackson. *Classical Electrodynamics*. John Wiley & Sons, New York, 3 edition, 1999.